Non-Body Conformal Grid Methods for Large-Eddy Simulations of Compressible Flows and their Applications in Computational Aeroacoustics

by

Jee-Whan Nam

A thesis
presented to the University of Waterloo
in fulfillment of the
thesis requirement for the degree of
Doctor of Philosophy
in
Mechanical and Mechatronics Engineering

Waterloo, Ontario, Canada, 2015

I hereby declare that I am the sole author of this thesis. This is a true copy of the thesis, including any required final revisions, as accepted by my examiners.

I understand that my thesis may be made electronically available to the public.

Abstract

In the applications of computational aeroacoustics (CAA) involving far-field noise predictions, the most common solution strategy is the *hybrid method* which combines a computational fluid dynamics (CFD) solver for the sound source field with an acoustic solver for the acoustic far-field. Hybrid CAA methods provide flexibility to select the most appropriate methods to compute the sound source and the acoustic fields, respectively, to suit various aeroacoustic problems. The present study reports the development of a hybrid large-eddy simulation (LES)-acoustic analogy method to effectively predict the noise of viscous flow over complex geometries.

With complex geometries, difficulties arise with numerical methods based on body fitted grids. Generating good quality body fitted grids around complex geometries is challenging and time-consuming. Alternatively, numerical methods based on non-body conformal grids can deal with bodies of almost any arbitrary shape. Although the present research was initially motivated for CAA applications, most of the contributions and the novelty of the work is in the development of efficient, easy-to-implement and more accurate non-body conformal methods that can be used for flow over complex geometries. To date, most of the listed work on non-body conformal methods is applied to incompressible flows. The use of non-body conformal methods for compressible turbulent flows is still rare and immature.

Two non-body conformal grid methods are developed and assessed in this work: the ghost-cell based immersed boundary method (GC-IBM) and the ghost-cell based cut-cell method (GC-CCM). In both methods, the boundary conditions on the immersed boundary are enforced through the use of "ghost cells" located inside the solid body. Variables on these ghost cells are computed using linear interpolation schemes. The implementation using GC-IBM is simpler; however, the exact shape of the fluid cells in the vicinity of the solid boundary is not detailed, which results in the loss or gain of mass and momentum. As such, sufficiently refined meshing is required in the vicinity of the solid boundary to mitigate the error on mass conservation. The implementation using GC-CCM requires more work; however, the underlying conservation laws is guaranteed by introducing "cut cells". A cell-merging approach is used to address the *small-cell problem* associated with

a Cartesian cut-cell method, which, if untreated, results in the numerical instability and stiffness of the system of equations.

The applicability of the developed non-body conformal methods is investigated in the compressible LES framework. Turbulent flows in various complex geometric settings are simulated using these non-body conformal methods for a wide range of Reynolds numbers and Mach numbers. For high Reynolds number flows, the developed non-body conformal methods employ a wall model to approximate the wall-shear stress, thus avoiding a requirement for severe grid resolution near the wall. No previously published work involves LES of high Reynolds number compressible flows using a wall model and a non-body conformal method. This research uses a simple wall model based on a wall function to approximate the near wall behaviour, but this approach can be extended to other wall models if necessary. Better wall modelling strategies should be investigated in the future. The numerical results demonstrate that the GC-CCM is capable of capturing near-wall flows relatively well despite the simple wall model used. GC-CCM also provides relatively accurate results compared to other non-body conformal methods.

Returning to the original research efforts for aeroacoustic applications, the GC-CCM is finally benchmarked for the prediction of far-field radiated noise from a flow over a circular cylinder. Of many hybrid approaches available in CAA, Ffowcs-Williams and Hawkings (FW-H) approach is selected to explore the far-field acoustic calculation. Comparison of the results to the experimental data shows that the developed hybrid LES-acoustic analogy method is capable of accurately predicting the sound spectrum for this case of three-dimensional flow over a cylinder in the sub-critical regime. Large-eddy simulations with more complex geometries, such as wings or high-lift systems, have not been performed as a part of this research. Further work is encouraged in order to conclude the research direction originally envisioned by the author.

Acknowledgements

The last three years of my PhD were particularly challenging. Initiating the PhD research in the evening, after a long day at work, was demanding both physically and mentally. I will never forget those endless nights that were only filled with fatigue and frustration. I have to emphasize that the completion of my PhD was only possible because of those who supported me during this time.

I would like to express my gratitude to my academic supervisor, Prof. Fue-Sang Lien, for his kind advices. My regular discussions with him at late night over Skype always left me with encouragement, which helped me to carry on with my research until the end.

I would also like to express my gratitude to my advisor at Bombardier Aerospace, George Waller, for his interest in my research and the understanding of my occasional shortened hours at work. Managing a PhD research while working in the industry can only be possible when one has an advisor like George at the work place.

I would like to thank the members of my doctoral examination committee, Prof. Stubley, Prof. Poulin and Prof. Ismail for their comments and recommendations. I would specifically like to thank Dr. Liou from NASA Glenn Research Center, for being my external examiner and providing me the most detailed comments despite his health condition. I truly wish him all the best with the recovery.

Last but most importantly, I would like to give my greatest appreciation to my mother, father, sisters, brother-in-law and my nieces. Their unconditional support and the positive attitudes were the constant source of strength in my life. I am indefinitely indebted to them.

To my parents

Table of Contents

List of Figures

List of Tables

Nomenclature

Acronyms

AUSM Advection Upstream Splitting Method

CIIM Cartesian cut-cell method, called conservative immersed-interface method

CAA Computational Aeroacoustics

CFL Courant-Friedrichs-Lewy

DNS Direct Numerical Simulation

ENO Essentially Non-oscillatory

FFT Fast Fourier Transform

FW-H Ffowcs-Williams and Hawkings

GC-CCM Ghost-Cell based Cut-Cell Method

GC-IBM Ghost-Cell based Immersed Boundary Method

HLLC Harten-Lax-van-Leer-Einfeldt

IBM Immersed Boundary Method

LES Large Eddy Simulation

LEE linearized Euler equations

LODI Local One-Dimensional Inviscid

M Mach number

MC MC slope limiter

MILES Monotone Integrated Large Eddy Simulation

MUSCL Monotone Upstream Scheme for Conservation Laws

NSCBC Navier-Stokes characteristic boundary conditions

PPM Piecewise Parabolic Method

RANS Reynolds Averaged Navier-Stokes

SPL_c Sound Pressure Level correction

SPL Sound Pressure Level

S-CCM Standard Cut-cell Method

TVD Total Variation Diminishing

UMIST UMIST slope limiter

Alphanumeric

$\mathbf{I}$	acoustic intensity
p'	acoustic pressure
u_i	Cartesian component of the instantaneous velocity in the x_i direction
x_i	Cartesian coordinates ($i = 1, 2, 3$)
h	channel height
C_I	closure coefficient for sub-grid scale turbulent kinetic energy term
C_R	compressible Smagorinsky constant
$\mathbf{c}_m$	coordinates of the centroid of the cut-cell
$\boldsymbol{C}$	cut cell
D	cylinder diameter
L	cylinder span
$\delta(f)$	Dirac delta function
r	distance between an observer's position and a source position
C_D	Drag coefficient
F_D	Drag force
$A_{i,j,k}$	face apertures
$\boldsymbol{F}$	fluid cell
F	flux vector
U_∞	free stream velocity
Re_τ	friction Reynolds number
u_τ	friction velocity
R	gas constant
$\boldsymbol{G}$	ghost cell

G	Green's function
q_j	heat-flux vector
$H(f)$	Heaviside function
F^I	inviscid (hyperbolic) component id F
C_L	Lift coefficient
F_L	Lift force
T_{ij}	Lighthill stress tensor
M_{in}	mass flow rate in
M_{out}	mass flow rate out
I	mirror image point for a node of a ghost cell
P	near-wall node
y^+	non-dimensional wall distance
u_n	normal velocity
N_f	number of cell faces
p	pressure
Re	Reynolds number
L_s	short cylinder span used for CFD simulation
$\boldsymbol{S}$	solid cell
L_c	spanwise cylinder coherence length
e	specific energy
c	speed of sound
s_{ij}	strain-rate tensor
S_t	Strouhal number
Q_j	sub-grid scale heat flux
A_i	surface area of face i
u_t	tangential velocity
T	temperature
E	Total energy
U	vector of conserved state variables
F^V	viscous (elliptic) component id F

K von Karman constant

Greek Symbols

ρ' acoustic density

θ angle between the radiation vector and the surface normal

β channel inclination angles

λ_i characteristic wave velocity

ρ fluid density

$\alpha_{i,j,k}$ fluid volume fraction

ϕ_I generic flow variable at the image point ϕ_I

ν kinematic viscosity

δ_{ij} Kronecker delta

Φ limiter

μ molecular viscosity

τ retarded time

σ_{ij} sub-grid scale stress tensor

κ thermal conductivity

τ_{ij} viscous stress tensor

τ_w wall-shear stress

λ wavelength

Accents

$\bar{U}$ averaged value of U

$\tilde{u}_i$ Cartesian component of the Favre-filtered velocity in the x_i direction

$\tilde{s}_{ij}$ Favre filtered strain-rate tensor

$\tilde{E}$ Favre-filtered total energy

$\bar{p}$ filtered pressure

$\tilde{H}$ filtered total enthalpy per unit volume

$\bar{\rho}$ time-averaged density

$\hat{r}$ unit radiation vector

Other Symbols

$\mathcal{L}_i$ amplitude of characteristic wave associated λ_i

$\triangle_i$	control volume dimension in the i direction
$\triangle$	filter width
$\mathcal{P}$	spjlit pressure
$\mathcal{M}$	split Mach number

Chapter 1

Introduction

1.1 Background

Airframe noise is defined as the non-propulsive components of noise radiated from a flying aircraft and it includes: the noise radiated from the wings, high-lift system (slat and flap), landing gear, and control surfaces. Although engine noise dominates during take-off, engines are often at flight idle during the final approach, and the airframe noise becomes comparable to, or sometimes greater than, the engine noise. In todays aircraft industry, noise at landing is becoming an important issue due to stringent regulations of aircraft community noise. For low Mach number flows with rigid bodies in motion, the dominant sound is due to surface pressure fluctuations. An understanding of the physical mechanisms involving the sound generation is a crucial step for reducing or controlling sound emission.

Aeroacoustics is a branch of acoustics that studies: 1. noise generation by turbulent fluid motion and/or aerodynamic forces interacting with surfaces (*e.g.* the airframe surface) and, 2. the noise propagation into the near or far field. The computation of the noise generation process and the sound propagation constitutes the main focus in the field of computational aeroacoustics (CAA). Since both phenomena are fully described by the full, time-dependent, compressible Navier-Stokes equations, *i.e.* the most general equation which describes the motion of fluids, one can naturally try to apply a *direct approach*

where the computational domain for the full, non-linear Navier-Stokes equations extends to the acoustic far-field. This method, however, poses limitations and challenges. The noise generating process is also inherently unsteady, which renders steady RANS (Reynolds Averaged Navier-Stokes) methods alone unsuitable. Unsteady RANS calculations are generally insufficient as well, except when the flow is dominated by simple large-scale oscillations. Modern turbulence simulation techniques such as DNS (Direct Numerical Simulation) or LES (Large Eddy Simulation) offer attractive alternatives, but they are not affordable. This is particularly the case in low Mach number flows, because there is a vast disparity in the magnitudes of the fluid dynamic and acoustic disturbances which places a stringent requirement on numerical accuracy. Since the acoustic far-fields are typically several orders of magnitude larger in length than the fluid dynamic far field, the direct approach can be bordering on the absurd in terms of the requirements for computing resources. It is for these reasons that the *hybrid approach* is developed to decouple the computation of flow from the computation of sound. This would involve using two different numerical solvers - a computational fluid dynamics (CFD) solver and an acoustic solver. In the CFD solver, LES or hybrid RANS/LES methods can be used to compute the aerodynamic noise generation mechanism (*i.e.* unsteady turbulent flow-fields). The far-field sound pressure can be calculated in the acoustic solver by integrating the time derivative of the wall pressure fluctuations at the surface of the rigid body. When performing CAA computations using the hybrid approach, efforts must be concentrated on the CFD simulation in order to provide the accurate information to the acoustic solver. In particular, when a large-eddy simulation (LES) technique is adopted for complex geometries, grid generation, sub-grid scale models and near-wall treatments should be handled carefully as they are crucial in predicting an accurate flow-field. Compared to the CFD calculations, acoustic calculations in the acoustic solver is relatively straight forward provided that its applicability is well justified.

1.2 Motivation for non-body conformal grids

When dealing with complex geometries in CFD, such as wings, high-lift system, landing gear, etc., significant effort has to be consumed on body conformal grid generation. For these complex geometry models, difficulties arise as high-order numerical schemes are desired which are also sensitive to the quality of computational grid. Generating a good quality body conformal grid around complex geometries is a challenging and time consuming task. An alternative approach is the numerical methods based on non-body conformal grids which specify a body force in such a way that it simulates the presence of a solid surface without altering the existing computational grid. These approaches provide a high level of flexibility such that bodies of almost any arbitrary shape can be handled while retaining most of the favourable properties of unstructured grids at significantly less computational cost. Simple examples of a body conformal grid and a non-body conformal grid are shown in Fig. 1.1.

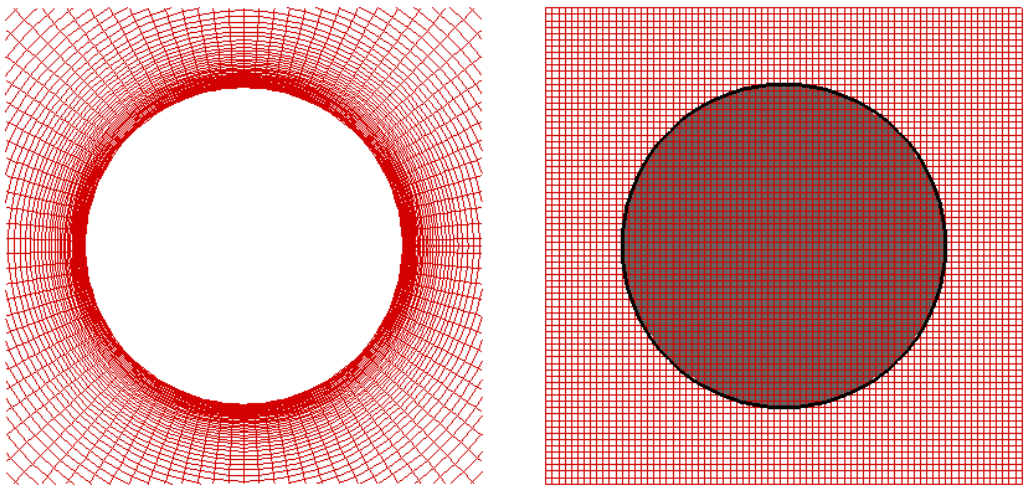

(a) Body conformal grids (b) Non-body conformal grids

Figure 1.1: Representation of a 2-D cylinder geometry using a body conformal (e.g. orthogonal) grid and using a non-body conformal grid.

When dealing with simulations of turbulent flows in the LES framework, the challenge

is to achieve a substantial reduction in the resource requirements for high Reynolds number near-wall flows, while maintaining a realistic description of the effects of near-wall processes. This is because accurate LES of wall bounded flows requires a near-wall resolution comparable to that for DNS, thus limiting the use of LES to moderate Reynolds numbers. One popular way to overcome this difficulty is to replace the detailed modelling of near-wall region with a wall model to skip the direct resolution of the viscous sublayer and buffer layer near the wall through proper parametrization. In this way the grid size can be related just to the large eddies developing in the fluid core, resulting in the justification of a relatively coarse near-wall grid resolution. The challenge however, with the non-body conformal methods, is the lack of control of the grid resolution in the vicinity of the solid boundary. The non-dimensional distance (y^+) of the first grid point off the boundary can vary dramatically depending on how the boundary cuts across the grid.

1.3 Thesis objectives

Although the present research was originally driven for the airframe noise applications, the majority of the work contributing to this research focuses on solving the turbulent flowfield - the noise generating mechanism. In particular, the focus is to accurately perform LES of turbulent compressible flows in a complex geometric setting. The goal is to develop an efficient, easy-to-implement and relatively accurate non-body conformal method that can be used in these simulations, and to demonstrate its applicability and flexibility. The most notable challenge is to incorporate the boundary conditions properly at the solid boundaries that are not aligned with the grid. In this research, new ghost-cell based cut-cell techniques are developed that are capable of capturing the flow dynamics accurately in the vicinity of the interface. The methods are tested for a wide range of Reynolds numbers as well as Mach numbers. To date, most of the listed work on non-body conformal method is devoted to incompressible flows (see [76] for a list of methods developed to date). The same for compressible viscous flows is still rare and immature [33, 83, 12]. Furthermore, most of reported simulations of highly turbulent flows in LES with a wall model are almost exclusively used on body fitted structured grids. Another goal of this work is to perform

LES of high Reynolds number flows in conjunction with a wall model where the near-wall grids are naturally coarse. To the best of the author's knowledge, there is no previously published work that involves LES of high Reynolds number compressible flows using a wall model and a non-body conformal method. Lastly, the developed and validated methods are applied to a simple aeroacoustic application where the goal is to predict the far-field radiated noise from flow over a circular cylinder.

1.4 Outline

This dissertation is delivered in seven main chapters. Chapter 2 describes the governing equations and large-eddy simulations formulation for describing the compressible turbulent flows. This includes the filtering procedure and the turbulence models used in this work. Chapter 3 describes the main elements of the numerical method to solve the governing equations, including flux evaluations, time integration and boundary treatments. Chapter 4 introduces the new non-body conformal methods with a summary of literature review on the topic. It carefully describes the implementation of the new methods with enough detail in the context of high Reynolds number flows, that it can be used for LES of compressible flows in conjunction with a wall model. Chapter 5 presents various test cases involving three-dimensional flow for a wide range of Reynolds numbers and Mach numbers in order to validate the methods introduced in Chapter 4. Last, but certainly not least, Chapter 6 introduces the topic of aeroacoustics and the methodology with which sound generated by turbulent flow can be computed. As a benchmark case, far-field radiated noise prediction from flow over a circular cylinder is computed. The flow-field is computed using the methodology developed in Chapter 4. The conclusions of this research, as well as recommendations for future work, can be found in Chapter 7.

Chapter 2

Mathematical Formulation

This chapter summarizes the governing equations and large eddy simulation (LES) formation used in this work for describing the compressible turbulent flows. Sec. 2.1 introduces the compressible Navier-Stokes equations, Sec. 2.2 introduces the concept of Favre filtering and filtered Navier-Stokes equations for turbulent flow simulations, and Sec. 2.3 discusses the closure problems and the turbulence models to address the closure problems.

2.1 Conservation equations

The compressible Navier-Stokes equations describe the conservation of mass, momentum and energy of any flow field. In a three-dimensional Cartesian coordinate system (x_i, $i = 1, 2, 3$), with t being time, these equations can be expressed in a conserved form as

$$\frac{\partial}{\partial t}(\rho) + \frac{\partial}{\partial x_i}(\rho u_i) = 0 \tag{2.1}$$

$$\frac{\partial}{\partial t}(\rho u_i) + \frac{\partial}{\partial x_j}(\rho u_i u_j) + \frac{\partial}{\partial x_i}(p) = \frac{\partial}{\partial x_j}(\tau_{ij}) \tag{2.2}$$

$$\frac{\partial}{\partial t}(\rho E) + \frac{\partial}{\partial x_j}(\rho E + p)u_j = \frac{\partial}{\partial x_j}(\tau_{ij}u_i) - \frac{\partial}{\partial x_j}(q_j) \tag{2.3}$$

where ρ is the fluid density, u_i is the component of the instantaneous velocity in the x_i direction, p is the pressure, and ρE is the total energy per unit volume. E is defined as $E = e + \frac{1}{2}u_i u_i$ where e is the specific energy. The system of equations remains unclosed until the equation of state (EOS) is defined to relate the thermodynamic variables together. It is assumed in the present study that the gasses under consideration obey to the perfect gas EOS and this can be expressed as

$$p = \rho R T \tag{2.4}$$

where R and T denote the gas constant and temperature. The constitutive relation between stress and strain rate for a Newtonian fluid is given as

$$\tau_{ij} = 2\mu s_{ij} - \frac{2}{3}\mu \frac{\partial u_k}{\partial x_k}\delta_{ij} \tag{2.5}$$

where μ is molecular viscosity, δ_{ij} is the Kronecker delta, and s_{ij} is the strain-rate tensor. s_{ij} is given as

$$s_{ij} = \frac{1}{2}(\frac{\partial u_i}{\partial x_j} + \frac{\partial u_j}{\partial x_i}). \tag{2.6}$$

q_j in Eq.(2.3) is the heat-flux vector which is given as

$$q_j = -\kappa \frac{\partial T}{\partial x_j} \tag{2.7}$$

where κ is thermal conductivity.

2.2 Governing equations for LES

Although Navier-Stokes equations can be solved directly by means of direct numerical simulation (DNS), it is not viable in most problems of engineering interest due to the computational resources that are required to resolve the smallest turbulent eddies. Large-eddy simulations (LES), on the other hand, is based on the idea of scale separation, of filtering of the governing conservation equations. Here, the large-scale quantities are obtained from the solution of the filtered form of the continuity, momentum and energy equations, while the small scale quantities are modelled using a proper turbulence modelling technique. The separation between large and small scales is obtained by applying a spatial filter to the governing equations.

2.2.1 Spatial filtering

Let $G_{\triangle}$ be the mathematical description of the filter kernel used for this operation. For an arbitrary function $f(x_i, t)$, the filtered variable $\bar{f}(x_i, t)$ is then defined as

$$\bar{f}(x,t) = \int f(x',t) G_{\triangle}(x - x') dx' \tag{2.8}$$

In most practical applications of LES using a finite-volume discretization method, the filter is not explicitly defined in the numerical simulations since the computation of cell average values acts as a built-in low pass filter for the governing equations. This implicit filter is a top-hat spatial filter where the filter width $\triangle$ is given by $\triangle = (\triangle_x \triangle_y \triangle_z)^{1/3}$. $\triangle_x$, $\triangle_y$ and $\triangle_z$ are the control volume dimensions in the x, y and z directions, respectively. Solution content with scales larger than this filter width is resolved, whereas the content at sub-grid scale is left to be modelled. In the work herein, this implicit spatial filter is used. A discussion on the relative merits of different filtering functions is beyond the scope of this work, and it should also be noted that the specific form taken by the filtering function is likely to be of secondary importance in any LES modelling strategy. If one desires to study the true solution of a LES that are independent of the numerical grid, an explicit

filter should be defined which can separate the filtering from the discretization operators.

2.2.2 Filtered conservation equations for LES

For LES of compressible flows, the notation is simplified by using a Favre filtered form $\tilde{f}$, which is density weighted as

$$\tilde{f} = \frac{\overline{\rho f}}{\bar{\rho}}. \tag{2.9}$$

Then, the variable can be decomposed into two components:

$$f = \tilde{f} + f'', \tag{2.10}$$

where $\tilde{f}$ is the resolved component and f'' is the unresolved component. Using this density weighted average (Favre filtering), it yields

$$\overline{\rho u_i} = \bar{\rho}\,\frac{\overline{\rho u_i}}{\bar{\rho}} = \bar{\rho}\tilde{u}_i. \tag{2.11}$$

Similarly,

$$\overline{\rho u_i u_j} = \bar{\rho}\widetilde{u_i u_j}; \quad \overline{\rho u_i T} = \bar{\rho}\widetilde{u_i T} \tag{2.12}$$

such that the filtered continuity and momentum equations can be derived easily. The use of the unweighted filter (Reynolds averaging), which is widely used for incompressible flows, is cumbersome for compressible flow equations as one will encounter some additional complexities when establishing suitable closure approximations.

The governing equations for LES are obtained through the application of the Favre-filter to the governing equations for instantaneous flow quantities, Eqs. (2.1)-(2.4), as

$$\frac{\partial}{\partial t}(\bar{\rho}) + \frac{\partial}{\partial x_i}(\bar{\rho}\tilde{u}_i) = 0 \tag{2.13}$$

$$\frac{\partial}{\partial t}(\bar{\rho}\tilde{u}_i) + \frac{\partial}{\partial x_j}(\bar{\rho}\tilde{u}_i\tilde{u}_j) + \frac{\partial}{\partial x_i}(\bar{p}) = \frac{\partial}{\partial x_j}(\bar{\tau}_{ij} + \sigma_{ij}) \tag{2.14}$$

$$\frac{\partial}{\partial t}(\bar{\rho}\tilde{E}) + \frac{\partial}{\partial x_j}(\bar{\rho}\tilde{E} + \bar{p})\tilde{u}_j = \frac{\partial}{\partial x_j}(\bar{\tau}_{ij} + \sigma_{ij})\tilde{u}_i + \frac{\partial}{\partial x_j}(\bar{q}_j + Q_j) \tag{2.15}$$

$$\bar{p} = \bar{\rho}R\tilde{T}. \tag{2.16}$$

Here, $\bar{\rho}$ is the time-averaged density, $\tilde{u}_i$ are the Cartesian components of the Favre-filtered velocity, $\bar{p}$ is the filtered pressure, and $\tilde{E}$ is the Favre-filtered total energy. $\bar{\rho}\tilde{E}$ is the filtered total energy per unit volume defined as

$$\bar{\rho}\tilde{E} = \bar{e} + \frac{1}{2}\tilde{u}_i\tilde{u}_i + \bar{\rho}\tilde{k} \tag{2.17}$$

where $\bar{\rho}\tilde{k}$ is the sub-grid scale turbulent kinetic energy per unit volume defined as

$$\bar{\rho}\tilde{k} = \frac{1}{2}\bar{\rho}(\widetilde{u_i u_i} - \tilde{u}_i\tilde{u}_i). \tag{2.18}$$

σ_{ij} in Eq.(2.14) is the sub-grid scale stress tensor given as

$$\sigma_{ij} = -\bar{\rho}(\widetilde{u_i u_j} - \tilde{u}_i\tilde{u}_j). \tag{2.19}$$

From the above, it can also be derived that $\sigma_{ii} = -2\bar{\rho}\tilde{k}$. Q_j in Eq.(2.15) is the sub-grid scale heat flux,

$$Q_j = -c_p\bar{\rho}(\widetilde{u_j T} - \tilde{u_j}\tilde{T}). \tag{2.20}$$

The molecular viscous stress tensor $\bar{\tau}_{ij}$ and the molecular heat flux vector $\bar{q}_j$ are negligible in free turbulent shear flows and outside the viscous sublayer in turbulent boundary

layers. It is also important to note that, in formulating the above equations, the commutation error between the filtering operation and the spatial derivative of solution content is ignored. When using an implicit filter, the commutation error is introduced at transition regions of different filter width (grid size). It is shown in [72] that, in the case of non-uniform grids, the commutation error can be large near the boundaries, where the change in the grid spacing is largest. It is also shown in [35] that the filtering and differentiation operations commute up to an error which is second order in the filter width. In the case of uniform grids, there is no commutation error. The implications of non-commutation have not been fully examined in the literature.

2.2.3 Closure problems

The Eqs. (2.13) to (2.15) are structurally similar to Eqs. (2.1) to (2.3) with the exceptions of the sub-grid scale terms, σ_{ij}, Q_j, and $\bar{\rho}\tilde{k}$. These terms arise from the differences between filtered products and products of filtered variables, and this difference takes into account the information contained at the sub-grid scale level. The closure of the system requires modelling of these sub-grid scale terms. The challenge is to construct robust models that will provide statistically accurate and meaningful results for the large scale flow structures. In the following section, the closing strategies used herein are summarized and discussed.

2.3 Turbulence model

2.3.1 Conventional explicit sub-grid scale modelling

In LES, the conventional approach to model the sub-grid scale stress terms is by employing the eddy viscosity hypothesis proposed by Boussinesq, which is mathematically analogous to the stress and strain rate for a Newtonian fluid, Eq. (2.5). Eddy viscosity concept relies on the assumption that the sub-grid scale term is proportional to the strain rate tensor. This mimics, in some sense, the effects of physical viscosity which dissipates all kinetic energy into heat at the Kolmogorov scale. In this concept, the eddy viscosity is responsible

for balancing the dissipation rate at filtered scales against the turbulent energy transfer from the resolved scale.

The most commonly used eddy viscosity model in LES is the Smagorinsky model [102] which bases its assumption that the small scale eddies maintain a state of isotropy. The extension of the standard Smagorinsky model to the compressible flows [57, 25] is used in this work to model the eddy viscosity term. The model is

$$\sigma_{ij} = 2C_R\bar{\rho}\triangle^2\sqrt{\tilde{s}_{ij}\tilde{s}_{ij}}(\tilde{s}_{ij} - \frac{1}{3}\tilde{s}_{kk}\delta_{ij}) - \frac{2}{3}\bar{\rho}\tilde{k}\delta_{ij} \tag{2.21}$$

where the Favre filtered strain-rate tensor $\tilde{s}_{ij}$ is defined as

$$\tilde{s}_{ij} = \frac{1}{2}(\frac{\partial\tilde{u}_i}{\partial x_j} + \frac{\partial\tilde{u}_j}{\partial x_i}). \tag{2.22}$$

C_R is the compressible Smagorinsky constant and it is found that $C_R = 0.012$ gives a high correlation between the exact and modelled stresses using various measures of comparison [25]. For the sub-grid scale turbulent kinetic energy term $\bar{\rho}\tilde{k}$, Yoshizawa's model [125] is used

$$-2\bar{\rho}\tilde{k} = \sigma_{ii} = -4\bar{\rho}C_I\triangle^2\tilde{s}_{kl}\tilde{s}_{kl}, \tag{2.23}$$

where C_I is an additional closure coefficient, which is generally quite small ranging somewhere between 0.005 to 0.0066. For the work herein, $C_I = 0$ is used instead because it is physically insignificant and numerically more efficient.

The biggest advantage of this standard Smagorinsky model is the simplicity, which renders this model still very popular; however, it is known to have some major drawbacks. Some of them include: its incapability to adjust to the local flow dynamics, its incapability of sub-grid scale energy backscatter to the resolved scales, and consequently, its limiting behaviour near the wall which correlates relatively poorly with the exact sub-grid scale tensor when compared to the behaviours of other turbulence models [126]. In fact, most of the sub-grid viscosity models do not exhibit the correct behaviour in the vicinity of

solid walls, resulting in an excessive damping of fluctuations in the near-wall region. To correct its erroneous near-wall behaviour, this model is often used with a van Driest damping function in order to account for wall proximity. Another alternative is the dynamic Smagorinsky model which dynamically computes the value at every grid point in space and at every time step. The dynamic model is not considered in this work.

For the sub-grid scale heat flux term, Q_j, the eddy diffusivity model is also used. The eddy viscosity model for sub-grid scale heat flux (Q_j) is given as

$$Q_j = \bar{\rho} c_p \frac{c_R}{p_{r_t}} \triangle^2 \sqrt{\tilde{S}_{kl}\tilde{S}_{kl}} \frac{\partial \tilde{T}}{\partial x_j}. \tag{2.24}$$

The turbulent Prandtl number P_{r_t} is chosen to be 0.4 following the work by Knight *et al.* [57]. This term is less significant as their contributions are relatively negligible when compared to the other sub-grid terms [119].

2.3.2 Implicit sub-grid scale modelling

In view of conventional explicit sub-grid scale modelling, the physical model (*e.g.* Smagorinsky eddy viscosity) for the sub-grid scale terms is held wholly responsible for the entire energy transfer from resolved to unresolved sub-grid scales. This requires a high order accurate numerical algorithm that minimizes numerical dissipation. In practice, however, the significant numerical errors, such as spatial-truncation error [34, 15], contaminate the effect of explicit sub-grid scale modelling terms. Unless the DNS solution is reached, increasing the grid resolution does not improve the situation because the errors can increase faster than the sub-grid terms when no explicit filtering is used [34]. Use of an explicit filter operation with a proper filter to grid width ratio can reduce these errors, but the required filter to grid ratio results in a substantial increase of computational cost for LES. A higher-order discretization scheme minimizes the numerical dissipation and reduces these errors, but a higher-order scheme is not practical for simulations involving complex geometries.

In view of implicit LES, numerical algorithm is held wholly responsible for the entire energy transfer between resolved and sub-grid scales, without an employment of an explicit

sub-grid scale model (*i.e.*, $\sigma_{ij} = 0$ and $Q_j = 0$). In this approach, called Monotone Integrated Large Eddy Simulation (MILES) [6], the dispersion and dissipation errors, arising from the upwind numerical scheme, are used to emulate this physical residual stress such that the sub-grid scale quantities are not explicitly modelled. It is shown by Garnier *et al.* [32] that the numerical diffusion in the MUSCL scheme (which will be discussed in Sec. 3.2.1) is larger than the diffusion of the sub-grid scale models, therefore the addition of an explicit sub-grid scale model is often unnecessary. The filtering and residual stress modelling are then performed implicitly by the numerical method. This method requires monotonic schemes by definition, in which case the scheme used in this work qualifies by virtue of the use of Riemann solvers when computing the inviscid fluxes. This will be shown in the next chapter.

Chapter 3

Numerical Methods

This chapter describes the main elements of the numerical method to solve the governing equations. Sec. 3.1 briefly summarizes the key elements involved in the finite-volume scheme and Sec. 3.2 presents the details on the numerical flux evaluations including both hyperbolic and elliptic components. Sec. 3.3 presents the time marching scheme employed to integrate the coupled system of nonlinear ordinary differential equations in time. Finally, procedures to define boundary conditions are described in Sec. 3.4

3.1 Finite-volume method

The governing equations described in the previous chapter can be written in the following differential form:

$$\frac{\partial U}{\partial t} + \vec{\nabla} \cdot \vec{F} = 0 \tag{3.1}$$

where U is the vector of conserved state variables and $\vec{F}$ is the flux vector. The flux vector can be decomposed into an inviscid (hyperbolic) component $\vec{F}^I$ and a viscous (elliptic) component $\vec{F}^V$ as

$$\vec{F} = \vec{F}^I + \vec{F}^V = (F_x^I - F_x^V, F_y^I - F_y^V, F_z^I - F_z^V) \tag{3.2}$$

where the subscripts represent the coordinate direction of the Cartesian component of the flux vector. By decomposing the flux into the inviscid (hyperbolic) term and the viscous (elliptic) term, standard methods for each flux calculation can be used separately for the evaluation. In particular, the high resolution shock-capturing methods can be used directly for the inviscid flux term, while the gradients of the viscous flux can be calculated with a conventional second-order central difference scheme.

The vectors U, F_x^I, F_x^V, F_y^I, F_y^V, F_z^I and F_z^V can be expressed as

$$\mathbf{U} = \begin{pmatrix} \bar{\rho} \\ \bar{\rho}\tilde{u} \\ \bar{\rho}\tilde{v} \\ \bar{\rho}\tilde{w} \\ \bar{\rho}\tilde{E} \end{pmatrix}, \tag{3.3}$$

$$\mathbf{F}_x^I = \begin{pmatrix} \bar{\rho}\tilde{u} \\ \bar{\rho}\tilde{u}^2 + \bar{p} \\ \bar{\rho}\tilde{u}\tilde{v} \\ \bar{\rho}\tilde{u}\tilde{w} \\ (\bar{\rho}\tilde{E} + \bar{p})\tilde{u} \end{pmatrix} \quad \mathbf{F}_y^I = \begin{pmatrix} \bar{\rho}\tilde{v} \\ \bar{\rho}\tilde{v}\tilde{u} \\ \bar{\rho}\tilde{v}^2 + \bar{p} \\ \bar{\rho}\tilde{v}\tilde{w} \\ (\bar{\rho}\tilde{E} + \bar{p})\tilde{v} \end{pmatrix} \quad \mathbf{F}_z^I = \begin{pmatrix} \bar{\rho}\tilde{w} \\ \bar{\rho}\tilde{w}\tilde{u} \\ \bar{\rho}\tilde{w}\tilde{v} \\ \bar{\rho}\tilde{w}^2 + \bar{p} \\ (\bar{\rho}\tilde{E} + \bar{p})\tilde{w} \end{pmatrix}, \tag{3.4}$$

$$
\mathbf{F}_x^V = \begin{pmatrix} 0 \\ \bar{\tau}_{xx} + \sigma_{xx} \\ \bar{\tau}_{xy} + \sigma_{xy} \\ \bar{\tau}_{xz} + \sigma_{xz} \\ \tilde{u}(\bar{\tau}_{xx} + \sigma_{xx}) + \tilde{v}(\bar{\tau}_{xy} + \sigma_{xy}) + \tilde{w}(\bar{\tau}_{xz} + \sigma_{xz}) - (\bar{q}_x + Q_x) \end{pmatrix},
$$

$$
\mathbf{F}_y^V = \begin{pmatrix} 0 \\ \bar{\tau}_{yx} + \sigma_{yx} \\ \bar{\tau}_{yy} + \sigma_{yy} \\ \bar{\tau}_{yz} + \sigma_{yz} \\ \tilde{u}(\bar{\tau}_{yx} + \sigma_{yx}) + \tilde{v}(\bar{\tau}_{yy} + \sigma_{yy}) + \tilde{w}(\bar{\tau}_{yz} + \sigma_{yz}) - (\bar{q}_y + Q_y) \end{pmatrix}, \tag{3.5}
$$

$$
\mathbf{F}_z^V = \begin{pmatrix} 0 \\ \bar{\tau}_{zx} + \sigma_{zx} \\ \bar{\tau}_{zy} + \sigma_{zy} \\ \bar{\tau}_{zz} + \sigma_{zz} \\ \tilde{u}(\bar{\tau}_{xz} + \sigma_{xz}) + \tilde{v}(\bar{\tau}_{yz} + \sigma_{yz}) + \tilde{w}(\bar{\tau}_{zz} + \sigma_{yz}) - (\bar{q}_z + Q_z) \end{pmatrix}.
$$

The finite-volume method used herein starts by integrating the differential form, Eq. (3.1) and applying the divergence theorem. The resulting integral form is written as

$$
\frac{d}{dt}\int_V U dV + \oint_\Omega n \cdot \vec{F} d\Omega = 0 \tag{3.6}
$$

where V is the control volume, Ω is the closed surface of the control volume, and n is the unit outward vector normal to the closed surface. $U = [\rho, \rho u, \rho v, \rho w, \rho E]^T$ is the flow state vector of the conserved variables and $\vec{F}$ is the flux vector. The averaged value of U within the cell is defined by an integration over the control volume,

$$
\bar{U} = \frac{1}{V}\int_V U dV. \tag{3.7}
$$

The preceding equations are discretized in a Cartesian computational domain which are then solved using a Godunov-type finite-volume method [36]. The Eq. (3.6) can be re-written in a semi-discrete form as

$$\frac{d\bar{U}_{i,j,k}}{dt} = -\frac{1}{V_{i,j,k}} \sum_{i=1}^{N_f} [\vec{n}_i \cdot \vec{F}_i A_i]_{i,j,k} \tag{3.8}$$

where N_f denotes the number of cell faces and A_i denotes the surface area of face i. The semi-discrete form represented by Eq. (3.8) is a set of coupled non-linear ODEs for cell-averaged quantities $\bar{U}_{i,j,k}$ at the (i,j,k)-indexed location, and this can be solved by an evaluation of the flux integrals. In the flux evaluation stage, the cell interface flux F is evaluated as a function of the discontinuous states on either side of the interface ($\bar{U}^L$, $\bar{U}^R$). This discontinuity arose due to the piecewise approximations for $\bar{U}_{i,j,k}$ in each control volume. In the time evolution stage, the solution is evolved forward in time using an appropriate time evolution method which updates the values for $\bar{U}_{i,j,k}$.

3.2 Flux evaluation

3.2.1 Inviscid (Hyperbolic) flux evaluation

For the inviscid fluxes $\vec{F}^I$, Godunov-type upwind finite-volume spatial discretization procedure is applied where the solution of Riemann problem is used to evaluate the cell interface flux. This procedure was first introduced by Godunov [36] as a method for solving non-linear Euler equations. In his original work, piecewise constant solution states are stored in the computational domain at each instance in time such that it permits the existence of discontinuous solutions and leads naturally to a Riemann problem at the interface between cells. The drawback of Godunov's original method is that it remained first-order accurate due to the piecewise constant reconstruction of the cell value. As such, poor accuracy in smooth regions of the flow and smeared representation of discontinuities are inevitable. However, the achievement and the drawback of his initial work inspired new

areas of research which directed to improve the algorithm to a high-resolution scheme and to incorporate more efficient solutions to the Riemann problem. A brief description of higher-order schemes and approximate Riemann solvers are discussed here.

High resolution methods

A second order scheme using a piecewise linear reconstruction and that preserves monotonicity was first introduced by Van Leer [61, 117]. This method, known as Monotone Upstream Scheme for Conservation Laws (MUSCL), makes use of a flux or a slope limiter to constrain the state reconstruction in the vicinity of discontinuities in order to preserves monotonicity. This concept of limiting the flux, which acts to prevent the occurrence of numerical oscillations, was later generalized via the concept of Total Variation Diminishing (TVD) by Harten [45]. TVD is a mathematical property which dictates that, as time progresses the sum of all the differences between adjacent points must remain the same or decrease. Thus, the amount of "variation" in a TVD scheme starts with is the maximum that it can ever achieve. This TVD-MUSCL scheme can be extended to higher order via piecewise polynomial reconstruction. For instance, it was extended to allow for piecewise parabolic reconstruction via the Piecewise Parabolic Method (PPM) of Colella and Woodward [18].

This TVD condition guarantees a stable solution, but the drawback is its strict requirement. As shown in [63], TVD property is not strictly required for stability. Another class of higher order scheme was developed with a goal to find looser criteria that allows a small increase in the total variation near extrema while still suppressing oscillations where necessary. Essentially Non-oscillatory (ENO) scheme and its variations (*e.g.* WENO, MENO) are based on the selection of stencils from the smoothest interpolants in order to obtain higher resolution [44, 99, 100]. A quantitative analysis of solutions to the Euler equations using TVD-MUSCL and ENO schemes is performed in [43], where the superiority of the ENO schemes over the TVD-MUSCL approach is established in terms of accuracy. In this work, the second order TVD-MUSCL sceme is used due to its simpler implementation.

Piecewise linear reconstruction with a limiter

The inviscid flux $\vec{F}^I$ between the two cells, (i,j) and $(i+1,j)$, is given at the cell interface $(i+\frac{1}{2},j)$ as

$$F_{i+\frac{1}{2},j} = F(R(U^L, U^R)) \tag{3.9}$$

where R represents the solution of the Riemann problem. The left state (^{L}) corresponds to information coming from the negative space direction, while the right state (^{R}) corresponds to information coming from the positive space direction. The left and right solution states ($\bar{U}^L$, $\bar{U}^R$) at a midpoint of each cell interface (x) are determined by the piecewise limited linear solution reconstruction as follows:

$$\begin{aligned} \bar{U}^L =& \bar{U}_{i,j,k} + \Phi\vec{\nabla}_{i,j,k}\bar{U}_{i,j,k} \cdot (\vec{x} - \vec{x}_{i,j,k}) \\ \bar{U}^R =& \bar{U}_{i+1,j,k} + \Phi\vec{\nabla}_{i+1,j,k}\bar{U}_{i+1,j,k} \cdot (\vec{x} - \vec{x}_{i+1,j,k}) \end{aligned} \tag{3.10}$$

The limiter Φ here constrains the state reconstruction in the vicinity of discontinuities such that the scheme reduces to first order-accuracy if local extrema are detected. This gives a global piecewise linear approximation that is non-oscillatory in the sense that its total variation is no greater than that of the discrete data. In the current algorithm, the slope limiters of minmod [93], superbee [93], MC [61] and UMIST [64] are implemented for the limited reconstruction, although other limiters would do almost equally well as long as the solution is smooth everywhere.

Flux solvers

Given the left and right solution state vectors at a cell interface ($\bar{U}^L$, $\bar{U}^R$), which are determined from the reconstruction stage, the inviscid flux F^I is then evaluated by solving the Riemann problem. An intuitive choice is to use an exact solution procedure for the Riemann problem such as the one outlined by Gottlieb and Groth [40]. This exact solution

is an iterative procedure, therefore, it is computationally expensive. It is also not economical since it provides the full wave configurations when the Godunov's scheme only requires the interface flux value and discards the rest. Furthermore, the time evolved solutions are treated as a piecewise constant by averaging out the details of the updated solution. This implies that the Godunov's method itself is merely an approximation. As such, an approximated value of the interface flux, rather than the exact value, should be sufficient. Approximated flux value can be obtained in various ways, such as approximate Riemann solvers (*e.g.* Roe [92], HLLC [45]), flux vector splitting methods ([103]), or AUSM ([66]) scheme to name a few.

In this work, the flux is formulated using an improved version of the Advection Upstream Splitting Method (AUSM), called AUSM$^+$. In the original formulation of AUSM proposed by Liou and Steffen [66] , the inviscid flux is split into a convective component and a pressure component. The idea is to discretize the two components separately, since the convective terms are considered scalar quantities convected by velocity u at the cell interface, whereas the pressure terms are governed by the acoustic wave speeds. The details related to this method are given in [67], which are also summarized here. First, the inviscid flux is written as a sum of these two components as

$$F_x^I = F^{(C)} + P = \tilde{u} \begin{pmatrix} \bar{\rho} \\ \bar{\rho}\tilde{u} \\ \bar{\rho}\tilde{v} \\ \bar{\rho}\tilde{w} \\ \bar{\rho}\tilde{H} \end{pmatrix} + \begin{pmatrix} 0 \\ \bar{p} \\ 0 \\ 0 \\ 0 \end{pmatrix} \tag{3.11}$$

where the filtered total enthalpy per unit volume $\tilde{H} = \tilde{E} + \bar{p}/\bar{\rho}$. Correspondingly, the numerical flux at the cell interface $F^I_{i+\frac{1}{2}}$ can be effectively written as

$$F^I_{i+\frac{1}{2}} = \tilde{u}_{i+\frac{1}{2}} \begin{pmatrix} \bar{\rho} \\ \bar{\rho}\tilde{u} \\ \bar{\rho}\tilde{v} \\ \bar{\rho}\tilde{w} \\ \bar{\rho}\tilde{H} \end{pmatrix}_{i+\frac{1}{2}} + \begin{pmatrix} 0 \\ \bar{p} \\ 0 \\ 0 \\ 0 \end{pmatrix}_{i+\frac{1}{2}} = m_{i+\frac{1}{2}} \tilde{a}_{i+\frac{1}{2}} \Phi_{i+\frac{1}{2}} + P_{i+\frac{1}{2}} \tag{3.12}$$

where

$$\Phi_{i+\frac{1}{2}} = \begin{cases} \Phi_i, & \text{if } m_{i+\frac{1}{2}} \geq 0, \\ \Phi_{i+1}, & \text{otherwise;} \end{cases} \tag{3.13}$$

$\Phi = (\bar{\rho}, \bar{\rho}\tilde{u}, \bar{\rho}\tilde{v}, \bar{\rho}\tilde{w}, \bar{\rho}\tilde{H})^T$, and $\tilde{a}_{i+\frac{1}{2}}$ is the filtered interface speed of sound. Here the convective flux $F^{(C)}$ is expressed in terms of the interface Mach number $m_{i+1/2}$. This interface Mach number is written as a sum of two individual components,

$$m_{i+\frac{1}{2}} = \mathcal{M}^+(M_i) + \mathcal{M}^-(M_{i+1}) \tag{3.14}$$

where $\mathcal{M}$ is the split Mach number and the superscripts "+" and "-" are associated with the right and left running waves. The split Mach numbers $\mathcal{M}$ takes the form

$$\mathcal{M}^{\pm}(M) = \begin{cases} \frac{1}{2}(M \pm |M|), & \text{if } |M| \geq 1, \\ \mathcal{M}^{\pm}_{\beta}(M), & \text{otherwise} \end{cases} \tag{3.15}$$

with

$$\mathcal{M}^{\pm}_{\beta}(M) = \pm\tfrac{1}{4}(M \pm 1)^2 \pm \beta(M^2 - 1)^2, \qquad -\tfrac{1}{16} \leq \beta \leq \tfrac{1}{2}. \tag{3.16}$$

Similarly, the interface pressure flux $P_{i+\frac{1}{2}}$ is written as

$$P_{i+\frac{1}{2}} = \mathcal{P}^{+}(M_i)p_i + \mathcal{P}^{-}(M_{i+1})p_{i+1} \tag{3.17}$$

where $\mathcal{P}$ is the split pressure and the superscripts "+" and "-" are associated with the right and left running waves. The split pressure $\mathcal{P}$ takes the form

$$\mathcal{P}^{\pm}(M) = \begin{cases} \frac{1}{2}(1 \pm sign(M)), & if\ |M| \geq 1, \\ \mathcal{P}^{\pm}_{\alpha}(M), & otherwise \end{cases} \tag{3.18}$$

with

$$\mathcal{P}^{\pm}_{\alpha}(M) = \tfrac{1}{4}(M \pm 1)^2(2 \mp M) \pm \alpha M(M^2 - 1)^2, \qquad -\tfrac{3}{4} \leq \alpha \leq \tfrac{3}{16}. \tag{3.19}$$

For simplicity, the interface speed of sound $\tilde{a}_{i+\frac{1}{2}}$ is chosen to be

$$\tilde{a}_{i+\frac{1}{2}} = \tfrac{1}{2}(\tilde{a}_i + \tilde{a}_j) \tag{3.20}$$

This method is known to be valid for a wide range of flow speeds and Mach numbers. The results presented hereafter are produced using the AUSM^{+} flux function. A more complete and detailed discussion is given in [67].

3.2.2 Viscous (Elliptic) flux evaluation

The viscous fluxes of the governing equations are elliptic in nature, therefore it should not be upwinded. In this work, the viscous terms are discretized by using the traditional second-order central difference scheme. The numerical viscous flux at the cell interface $F^{V}_{i+\frac{1}{2}}$ takes the form

$$F^{V}_{i+\frac{1}{2}} = F(U_{i+\frac{1}{2}}, \vec{\nabla}U_{i+\frac{1}{2}}) \tag{3.21}$$

where $U_{i+\frac{1}{2}}$ is the solution vector at the cell interface, which is evaluated by averaging the values of the left and right states as

$$U_{i+\frac{1}{2}} = \frac{U^L + U^R}{2}. \tag{3.22}$$

The gradient $\vec{\nabla} U_{i+\frac{1}{2}}$ is evaluated as

$$\vec{\nabla} U_{i+\frac{1}{2}} = \frac{\vec{\nabla} U_i + \vec{\nabla} U_{i+1}}{2} \tag{3.23}$$

where, in the case of x direction,

$$\vec{\nabla} U_i = \frac{U_{i+1,j,k} - U_{i-1,j,k}}{x_{i+1,j,k} - x_{i-1,j,k}} \quad \text{and} \quad \vec{\nabla} U_{i+1} = \frac{U_{i+2,j,k} - U_{i,j,k}}{x_{i+2,j,k} - x_{i,j,k}}. \tag{3.24}$$

3.3 Time integration

The set of coupled non-linear ordinary differential equations (ODEs) given by Eq. (3.8) can be integrated forward in time using a time-marching method. A wide variety of time-marching methods, such as explicit methods (*e.g.* explicit Euler, Adams-Bashforth and Runge-Kutta methods) and implicit methods (*e.g.* implicit Euler, trapezoidal, AdamsMoulton and Runge-Kutta methods), are available for the integration. In this work, the linear reconstruction used in the spatial discretization is globally second-order accurate. To maintain a consistent scheme in terms of accuracy, a time-marching scheme having the same order of accuracy is used.

An explicit method of second-order Adams-Bashforth scheme is employed in this work, *i.e.*

$$\bar{\mathbf{U}}^{n+1}_{i,j,k} = \bar{\mathbf{U}}^{n}_{i,j,k} + \Delta t(3/2 f^n - 1/2 f^{n-1}) \tag{3.25}$$

where

$$
\begin{aligned}
f^n &= F(U^n_{i,j,k}, t^n) \\
&= \frac{F^n_{i+1/2,j,k} - F^n_{i-1/2,j,k}}{\Delta x} + \frac{F^n_{i,j+1/2,k} - F^n_{i,j-1/2,k}}{\Delta y} + \frac{F^n_{i,j,k+1/2} - F^n_{i,j,k-1/2}}{\Delta z}
\end{aligned} \tag{3.26}
$$

on a three-dimensional Cartesian grid. $F^n_{i\pm1/2,j,k}$, $F^n_{i,j\pm1/2,k}$ and $F^n_{i,j,k\pm1/2}$ denote the face-averaged fluxes at the cell interfaces at the current time step n.

For an explicit time marching method such as one used in this work, the time step is limited by the inviscid Courant-Friedrichs-Lewy (CFL) stability as well as by the viscous von Neumann stability constraints. The exact computation of the time step that ensures stability requires the numerical analysis of the eigenvalues of the amplification matrix of the numerical scheme [49]. Here, a simplified analysis is followed. A stable local time step is then taken as the minimum of the inviscid and viscous time steps as

$$
\triangle t^n = min(CFL\frac{\triangle l}{|\vec{u}| + a}, \frac{\alpha}{2}\frac{\rho\triangle l^2}{max(\nu, \nu_t)}) \tag{3.27}
$$

where $\triangle l$ is a minimum cell-face length, a is the speed of sound, ν and ν_t are molecular viscosity and turbulent eddy viscosity, respectively, and α is a scaling factor.

3.4 Boundary conditions

Boundary conditions are enforced by using "ghost" cells, which form a layer of cells around the computational domain. In this section, procedures to define boundary conditions for the compressible Navier-Stokes equations are described.

3.4.1 Periodic boundary conditions

Assumption of periodicity of the computational domain is often used in DNS and LES of channel flows. This is suitable for fully developed homogeneous flow, since the flow fields

at inflow and outflow are considered as statistically the same provided that they are far enough apart from each other. In this case, the computational domain can be regarded as repeating itself infinitely. The domain is then folded on itself and no boundary conditions are actually required. Using ghost cells, this can be achieved by copying flow variables of the outflow (inflow) boundary to the ghost cells at the inflow (outflow) boundary.

3.4.2 Navier-Stokes characteristic boundary conditions

For simulations in which no periodicity is assumed, flow inlets and outlets must be treated according to the physical boundary conditions. To avoid the appearance of spurious reflections at these open boundaries in compressible flows, the three-dimensional Navier-Stokes characteristic boundary conditions (NSCBC), introduced by Pointsot and Lele [86], are considered in this work to describe the non-reflecting boundary conditions. This is a generalized formulation of the characteristic analysis for the Euler equations introduced by Thompson [110, 111] who successfully applied the one-dimensional approximation of the characteristic boundary conditions in the multi-dimensional Euler equations. The basic idea is to decompose the hyperbolic equations into wave modes of velocity to determine incoming and outgoing waves of the domain. The behaviour of the outgoing waves are determined entirely by the solutions within the boundary, whereas the incoming waves are specified according to the boundary conditions. Poinsot and Lele [86] later included the viscous diffusion terms to generalize the original formulation to the viscous diffusive Navier-Stokes equations. The mathematical well-posedness and stability of the viscous boundary conditions have also been investigated extensively [81, 24]. In this study the NSCBC method of [86] is used for non-periodic flow cases and the strategy is summarized below.

When considering boundary conditions for x direction (other directions can be handled similarly), the governing equations (Eq. 2.1 - Eq. 2.3) can be recast in the following characteristic form.

$$\frac{\partial \rho}{\partial t} + d_1 + \frac{\partial(\rho v)}{\partial y} + \frac{\partial(\rho w)}{\partial z} = 0, \tag{3.28}$$

$$\frac{\partial(\rho u)}{\partial t} + u d_1 + \rho d_3 + \frac{\partial(\rho u)v}{\partial y} + \frac{\partial(\rho u)w}{\partial z} = \frac{\partial \tau_{1j}}{\partial x_j}, \tag{3.29}$$

$$\frac{\partial(\rho v)}{\partial t} + v d_1 + \rho d_4 + \frac{\partial(\rho v)v}{\partial y} + \frac{\partial(\rho v)w}{\partial z} + \frac{\partial p}{\partial y} = \frac{\partial \tau_{2j}}{\partial x_j}, \tag{3.30}$$

$$\frac{\partial(\rho w)}{\partial t} + w d_1 + \rho d_5 + \frac{\partial(\rho w)v}{\partial y} + \frac{\partial(\rho w)w}{\partial z} + \frac{\partial p}{\partial z} = \frac{\partial \tau_{3j}}{\partial x_j}, \tag{3.31}$$

$$\begin{aligned} &\frac{\partial \rho E}{\partial t} + \frac{1}{2}(u_k u_k) d_1 + \frac{d_2}{\gamma - 1} + (\rho u) d_3 + (\rho v) d_4 + (\rho w) d_5 \\ &\quad + \frac{\partial}{\partial y}[(\rho E + p)v] + \frac{\partial}{\partial z}[(\rho E + p)w] = \frac{\partial(u_j \tau_{ij})}{\partial x_i} - \frac{\partial q_i}{\partial x_i}. \end{aligned} \tag{3.32}$$

The mathematical process to rewrite the governing equations to the above form is explained in detail in [111, 86] and it is also summarized in Appendix A. The purpose of rewriting the governing equations in this form which contains the quantities d_i is to specify boundary conditions in a convenient manner. The quantities d_i are related to characteristic waves given by

$$\begin{pmatrix} d_1 \\ d_2 \\ d_3 \\ d_4 \\ d_5 \end{pmatrix} = \begin{pmatrix} 1/c^2[\mathcal{L}_2 + 1/2(\mathcal{L}_5 + \mathcal{L}_1)] \\ (1/2)(\mathcal{L}_5 + \mathcal{L}_1) \\ (1/2\rho c)(\mathcal{L}_5 - \mathcal{L}_1) \\ \mathcal{L}_3 \\ \mathcal{L}_4 \end{pmatrix} \tag{3.33}$$

where $\mathcal{L}_i$ is an amplitude of characteristic wave associated with wave velocity λ_i. λ_i's are given by

$$\lambda_1 = u - c \quad , \quad \lambda_2 = \lambda_3 = \lambda_4 = u \quad , \quad \lambda_5 = u + c \tag{3.34}$$

where c is the speed of sound, defined as $c = \sqrt{\frac{\gamma p}{\rho}}$. λ_1 and λ_5 are the velocities of the characteristic waves moving in the negative and positive x directions, respectively, λ_2 is the velocity for entropy advection, and λ_3 and λ_4 are the velocities at which v and w are advected in the x direction. If the velocity λ_i points out of the solution domain (outgoing wave), the corresponding $\mathcal{L}_i$ is computed from its definition below using one-sided derivative approximations.

$$\mathcal{L}_1 = \lambda_1(\frac{\partial p}{\partial x} - \rho c \frac{\partial u}{\partial x}), \tag{3.35}$$

$$\mathcal{L}_2 = \lambda_2(c^2 \frac{\partial \rho}{\partial x} - \frac{\partial p}{\partial x}), \tag{3.36}$$

$$\mathcal{L}_3 = \lambda_3 \frac{\partial v}{\partial x}, \tag{3.37}$$

$$\mathcal{L}_4 = \lambda_4 \frac{\partial w}{\partial x}, \tag{3.38}$$

$$\mathcal{L}_5 = \lambda_5(\frac{\partial p}{\partial x} + \rho c \frac{\partial u}{\partial x}). \tag{3.39}$$

If, on the other hand, λ_i points into the solution domain (incoming wave), the value of the corresponding $\mathcal{L}_i$ must be specified from the boundary conditions. To specify these values of $\mathcal{L}_i$'s that are incoming waves, the technique called LODI (Local One-Dimensional Inviscid) relation [86] is considered in this work. There is no exact simple method to specify these values for multidimensional equations, therefore, these values are approximated by examining a LODI relation. The LODI relation are obtained by rewriting Eqs. (3.28) - (3.32) in terms of primitive variables and $\mathcal{L}_i$. Neglecting other directions, one gets

$$\frac{\partial \rho}{\partial t} + \frac{1}{c^2}\left[\mathcal{L}_2 + \frac{1}{2}(\mathcal{L}_5 + \mathcal{L}_1)\right] = 0, \tag{3.40}$$

$$\frac{\partial p}{\partial t} + \frac{1}{2}(\mathcal{L}_5 + \mathcal{L}_1) = 0, \tag{3.41}$$

$$\frac{\partial u}{\partial t} + \frac{1}{2\rho c}(\mathcal{L}_5 - \mathcal{L}_1) = 0, \tag{3.42}$$

$$\frac{\partial v}{\partial t} + \mathcal{L}_3 = 0, \tag{3.43}$$

$$\frac{\partial w}{\partial t} + \mathcal{L}_4 = 0. \tag{3.44}$$

In the current work, this characteristic boundary treatment is applied to open boundaries where the viscosity and the heat transfer are assumed insignificant ($\tau_{ij} \approx 0, q \approx 0$). The boundary treatment, using the above LODI relation, then follows the strategy of NSCBC for the Euler equation described in [86]. The procedure involves three steps:

Step 1: For each physical boundary condition, eliminate the corresponding conservation equations from the system of Eqs. 3.28 - 3.32. For example, if a constant pressure p is specified at the outlet there is no need to use the energy equation Eq. (3.32).

Step 2: For each boundary condition, use the corresponding LODI relation to express the unknown $\mathcal{L}_i$'s (associated with the incoming waves), as a function of known $\mathcal{L}_i$'s (associated with the outgoing waves). In the example of constant outlet pressure, the only incoming wave is $\mathcal{L}_1$ and LODI relation, Eq. (3.41) suggests that $\mathcal{L}_1 = -\mathcal{L}_5$.

Step 3: Use the remaining conservation equation of the system of Eqns. 3.28 - 3.32 combined with the values of the $\mathcal{L}_i$'s obtained from Step 2 to compute all variables which were not given by the boundary conditions.

The implementation of the above general theory into specific physical boundary conditions at the inlet and outlet are discussed in the subsequent sections.

Subsonic inflow

At a subsonic inflow boundary, four characteristic waves ($\mathcal{L}_2$, $\mathcal{L}_3$, $\mathcal{L}_4$, $\mathcal{L}_5$) are entering the domain, while one ($\mathcal{L}_1$) is leaving the domain at the speed $\lambda_1 = u - c$ (Fig. 3.1(a)). The amplitude of $\mathcal{L}_1$ is determined from the interior information, Eq. (3.35), while the rest of the $\mathcal{L}_i$'s are determined from the physical boundary conditions. There are many physical boundary conditions that exist and, in this work, u, v, w and ρ are chosen to be imposed at the inlet. This leads the time derivative of these variables to be zero. By using the LODI system Eqs. (3.40) - (3.44) (except Eq. (3.41)), the expression for the $\mathcal{L}_i$'s can be determined in terms of $\mathcal{L}_1$. For example, Eq. (3.42) implies that $\mathcal{L}_5 = \mathcal{L}_1$ since the time derivative of u is zero. Other $\mathcal{L}_i$'s are determined similarly as

$$\begin{pmatrix} \mathcal{L}_2 \\ \mathcal{L}_3 \\ \mathcal{L}_4 \\ \mathcal{L}_5 \end{pmatrix} = \begin{pmatrix} -\mathcal{L}_1 \\ 0 \\ 0 \\ \mathcal{L}_1 \end{pmatrix}. \tag{3.45}$$

With all the $\mathcal{L}_i$'s identified, the Eqs. (3.28) - (3.32) can now be solved at the boundary.

Subsonic non-reflecting outflow

For the non-reflecting outflow at the outlet, there are four characteristic waves ($\mathcal{L}_2$, $\mathcal{L}_3$, $\mathcal{L}_4$, $\mathcal{L}_5$) that are leaving the domain, while one ($\mathcal{L}_1$) is entering the domain (Fig. 3.1(a)). To avoid the reflection of waves, the amplitude of the incoming wave is enforced to be zero. This can be achieved simply by setting $\mathcal{L}_1 = 0$. The amplitudes of other $\mathcal{L}_i$'s are determined from the interior information, Eqs. (3.35) - (3.39).

Supersonic inflow

For the supersonic inflow at the inlet, all the characteristic waves are entering the domain, including $\mathcal{L}_1$ (Fig. 3.1(b)). Consequently, all the amplitudes of $\mathcal{L}_i$'s must be specified from the boundary, hence, all the flow variables (u, v, w, ρ and p) are imposed at the inlet.

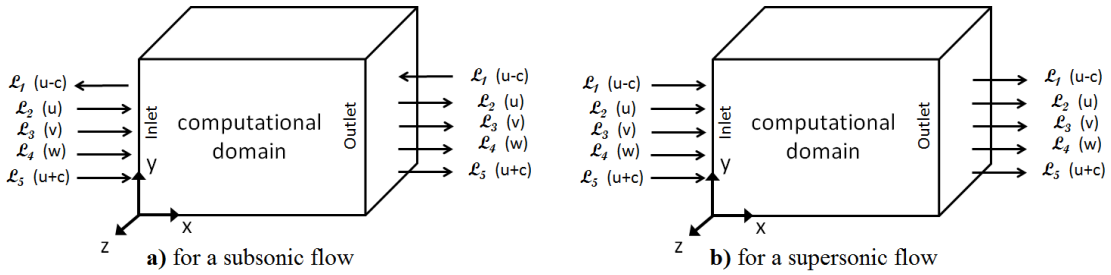

Figure 3.1: Characteristic wave leaving and entering the computational domain through an inlet and an outlet plane for a) a subsonic flow, and b) a supersonic flow.

Supersonic outflow

For the supersonic outflow at the outlet, all the characteristic waves are leaving the domain (Fig. 3.1(b)). Consequently, no boundary conditions is required to be specified at all, and the evolution of the flow at the boundary is determined completely by the interior information. In this case, all the $\mathcal{L}_i$'s are computed from the interior information.

3.4.3 Solid wall boundary conditions

On solid walls, the no-slip conditions are enforced, which is achieved by imposing flow variables at the ghost cells using Dirichlet and Neumann conditions. Conditions of Dirichlet type are prescribed for the velocity in order to capture the no-slip wall, while conditions of Neumann type are prescribed for pressure and density to model the adiabatic wall. The normal velocity (or pressure gradient) is set to be zero.

It is worth noting here that there is an alternative and perhaps more rigorous method to impose the solid walls in compressible flow simulations, based on the characteristic wave decomposition. This method utilizes the NSCBC method of Sec. 3.4.2, and it is also described in [86]. The similarities and differences between the method based on Dirichlet/Neumann conditions and the method based on the NSCBC are reported in [59], which concludes that the latter method (based on the NSCBC) leads to a more stable and robust scheme. The two methods, however, lead to equivalently accurate results, and this is fur-

ther confirmed in the context of the immersed boundary method in [73]. As such, and also due to the simpler implementation of the former method (based on Dirichlet/Neumann conditions), the latter method is not considered in this work.

In the context of non-body conformal grid, the solid boundaries are immersed in the Cartesian grids, resulting in cutting the Cartesian cells in a random manner and making the implementation of boundary conditions difficult. In this approach, the challenge is to compute the solution states at the ghost cell point such that the reconstructed solution and the associated boundary flux satisfy the no slip wall on the immersed boundary. The procedures, with which the solution states at the ghost cells are determined, are discussed in detail in the next chapter.

Chapter 4

Non-body Conformal Grid Treatment

4.1 Introduction

4.1.1 Motivation

When dealing with complex geometries in CFD, difficulties arise with the numerical methods based on body fitted grids because high-order numerical schemes are often desired but they are sensitive to the quality of the computational grids. Generating good quality body fitted grids around the complex geometries is challenging and time-consuming. An alternative approach is the numerical methods based on non-body conformal grids which specify a body force in such a way that it simulates the presence of a solid surface without altering the existing computational grid. Most salient advantage is in its high level of flexibility in handling highly complex geometries at significantly less computational cost. Most notable challenge is in how to incorporate the boundary conditions properly at the solid boundaries that are not aligned with the grid. Non-body conformal methods can be divided into two major classes based on the specific treatment of the cells in the vicinity of the boundary: (1) Immersed boundary methods, which enforce wall conditions indirectly through the use of forcing functions, and (2) Cartesian cut-cell methods, which rely on the construction of irregular grid cells near surfaces. In this research, two non-body conformal

grid methods are studied: the ghost-cell based immersed boundary method (GC-IBM) and the ghost-cell based cut-cell method (GC-CCM). Turbulent compressible flows in various complex geometric settings are simulated using these non-body conformal methods in this work. In the case of high Reynolds number flows, a wall model is employed to approximate the wall-shear stress such that a severe grid resolution requirement near the wall is avoided. In this chapter, the implementations of these methods are described in detail.

4.1.2 Overview of immersed boundary method (IBM)

The immersed boundary method (IBM) was first introduced by Peskin [84], and many strategies have since been developed in order to properly impose the wall boundary conditions (as well summarized in [76]). Over the years, these strategies have been tested in a wide range of CFD applications using both finite-difference and finite-volume methods. During the early stages of development, the effect of solid body inside a fixed mesh was represented by including a continuous forcing function in the momentum equation. This arrangement was successfully tested for a variety of flows in the incompressible flow solvers at low Reynolds numbers [37, 38, 97, 55]. This approach, known as the continuous forcing approach, has exhibited some stability and accuracy issues with highly unsteady flows at high Reynolds numbers [58, 104]. Another approach, known as discrete forcing approach, then gained popularity by discretizing the governing equations on a Cartesian grid without the presence of the immersed boundaries. The discretization near the immersed boundaries is then adjusted in order to account for the boundaries. Mohd-Yusof [77] used a forcing term such that the desired velocity distribution is obtained at the boundaries. This forcing term is determined by the difference between the linearly interpolated velocities in the boundary points and the desired boundary velocities. In this manner, errors between the calculated velocities and the desired velocity profile on the immersed boundaries are compensated. They implemented the method for a complex geometry in a pseudo-spectral code while avoiding the need of a small computational time step. Fadlun *et al.* [26] then applied this approach to a three-dimensional finite difference method on a staggered grid and showed that the approach was more efficient than the continuous forcing approach.

Tseng and Ferziger [112] extended the IBM approaches (of [26] and [118]) to achieve a higher-order representation of the boundary using ghost cells inside the body. Ghost cells are defined as cells in the solid body that have at least one side neighbouring with a fluid cell. The basic idea here is to compute the flow variables in these ghost cells such that the boundary conditions on the immersed boundary in the vicinity of the ghost cells are satisfied. In the computation, an interpolation scheme is devised which implicitly incorporates the boundary conditions. This interpolation is the basic condition for IBM in the discrete forcing approach. There are a number of options available for constructing the interpolation schemes [70]. One simple option is the bi-linear (for 2D) or tri-linear (for 3D) interpolation. Most of the IBM applications available in the literature are based on this linear reconstruction and they are focused on simulating inviscid or laminar flows.

To this date, most of the listed work on IBM is devoted to incompressible flows [see [76] for a list of methods developed to date]. The same for compressible viscous flows is still rare and immature [33, 83, 12]. Most of the IBM applications available in the literature are also based on the linear reconstruction, focusing on simulating inviscid or laminar flows. Ghias *et al.* [33] developed a finite-difference based ghost cell method, same principle as suggested by Tseng *et al.* [112], for compressible viscous flows using a bi-linear interpolation in order to determine the ghost-cell values. Their method was successfully tested for flows over a circular cylinder and an airfoil at low Reynolds (and Mach) numbers where the flow feature was essentially laminar. De Palma *et al.* [83] also developed an immersed boundary method for compressible viscous flows and demonstrated its efficiency and versatility from incompressible to supersonic flow conditions. De Tullio *et al.* [22] developed another variant of IBM to deal with compressible turbulent flows in conjunction with a local grid refinement such that the first cell from the wall is located in the viscous sublayer. High Reynolds number turbulent flows are still possible provided that a very fine mesh is generated near the wall. The drawback is that it could lead to erroneous predictions with a marginal grid resolution. This is because the method is not designed to satisfy the underlying conservation laws in the vicinity of the interface, hence it fails to capture the non-linearities of turbulent flows in the near-wall regions when the grid resolution is not sufficiently fine.

4.1.3 Overview of Cartesian cut-cell method

Immersed boundary method requires a sufficiently fine mesh such that the error in mass conservation stays insignificant. The Cartesian cut-cell method, on the other hand, resorts to a finite-volume approach thereby guaranteeing strict global and local conservation of mass and momentum. This method uses a regular Cartesian grid for all cells, except those which intersect the solid surface. Only the intersecting cells are then truncated or merged to conform to the shape of the solid geometry such that the advantage of using a Cartesian grid method is still retained. This method was first introduced for inviscid flow computations by Clarke *et al.* [16] and was later applied to simulations of viscous flows [116, 114, 113, 123]. The three dimensional implementations of this method for both Euler [52] and compressible Navier-Stokes equations [47] are then reported. Although a second-order accuracy in the discretization was typically used for the interior cells, the order of accuracy in the vicinity of the interface was typically decreased to one [47] or near one (≈ 1.5) [52] and, it was for that reason that the applications were often combined with a local mesh refinement in order to improve the accuracy. In view of foregoing, Meyer *et al.* [74] then developed a second-order accurate Cartesian cut-cell method, called conservative immersed-interface method (CIIM), which was used to solve the incompressible Navier-Stokes equations on three-dimensional non-uniform staggered grids in the LES framework. This method has been gaining popularity because it has shown to be efficient, conservative, second-order accurate, and suitable for LES of wall-bounded flows. Most recently, the method has been extended for the computation of compressible turbulent flows in large-eddy simulations [73] and incompressible turbulent flows in large-eddy simulation in combination with a wall model [13].

4.1.4 Wall modelling

From the LES point of view, the challenge is to achieve a substantial reduction in the resource requirements for high Reynolds number near-wall flows, yet maintaining a realistic description of the effects of near-wall processes. This is because accurate LES of wall bounded flows requires a near-wall resolution comparable to that for DNS, thus limiting the

use of LES to moderate Reynolds numbers. One popular way to overcome this difficulty is to replace the near-wall region with a wall model to skip the direct resolution of the viscous sublayer and buffer layer through a proper parametrization. In this way the grid size can be related just to the large eddies developing in the fluid core, resulting in allowing relatively coarser coarse grids near the wall. Most of reported simulations of highly turbulent flows in LES with a wall model are almost exclusively used on body fitted structured grids. There are only few published papers focusing on the wall modelling of LES on non-body conformal grids [108, 94, 13]. The challenge with the non-body conformal methods is the lack of control of the grid resolution in the vicinity of the solid boundary. The non-dimensional distance (y^+) of the first grid point off the boundary can vary dramatically depending on how the boundary cuts across the grid. Roman *et al.* [94] used the immersed boundary method where the velocity and the wall shear stress, which are the two main components required for a wall model, are locally reconstructed based on the y^+ value of the first node off the boundary. Their method was tested in the framework of finite difference implementation which generally does not satisfy the conservation law in the vicinity of the boundary. Chen *et al.* [13] used the conservative cut-cell method of [74] with a wall model which allowed for simpler and more conventional implementation of a wall model than that by Roman *et al.* [94] for high Reynolds number flow computations.

4.2 Non-body conformal grid methods

4.2.1 Ghost-cell based immersed boundary method (GC-IBM)

This section describes the ghost-cell based immersed boundary method (GC-IBM) that is utilized in this research. The ghost cell method achieves a higher-order representation of the boundary in a way that is simple and flexible with the local spatial reconstruction. Fig. 4.1 depicts an example of a Cartesian grid in two dimensions with an immersed solid boundary. Each cell is classified as one of the following three types: *fluid*, *solid* and *ghost cells*. *Fluid cells* $\boldsymbol{F}$ are cells whose cell centres lie outside the solid boundary, *solid cells* $\boldsymbol{S}$ are cells whose cell centres lie inside but not adjacent to the solid boundary, and *ghost*

cells ***G*** are cells whose cell centres lie inside and adjacent to the solid boundary. Two layers of ghost cells inside the solid boundary are assigned in order to be consistent with the second-order piecewise linear spatial reconstruction when computing the left and right solution states, recall Eq. (3.10). The evaluations of cell interface fluxes then become straightforward everywhere including in the vicinity of the boundary. The ghost cells are identified as any cell in the solid region that has at least one immediate neighbour in the fluid (*i.e.* the first layer of the ghost cells) and/or is neigh boring with a cell that has an immediate neighbour in the fluid (*i.e.* the second layer of the ghost cells). For each node of a ghost cell, a respective mirror image point I is determined by reflecting the node across the boundary into the interior fluid domain, as shown in Fig. 4.2. Using surrounding fluid cells, the flow variables at this image point can be obtained through an interpolation scheme. Ensuring that the surface boundary is always exactly midway between the ghost and image points guarantees that the interpolation scheme remains well behaved. There are a number of options available for constructing the interpolation scheme [70] and the choice depends on one's interest in accuracy and cost. One simple option is a linear interpolation where flow variables are expressed in terms of a linear (bi-linear in 2D or tri-linear in 3D) interpolant. In the case of bi-linear interpolation, the generic flow variable at the image point ϕ_I can be expressed as

$$\phi(x, y) = C_1 xy + C_2 x + C_3 y + C_4 \tag{4.1}$$

The four unknown coefficients C_i can be expressed in terms of the variables at the four nodes surrounding the image point. Three different situations, illustrated in Figs. 4.2(a) to 4.2(c), exist for a given image point and these have to be handled in a well-posed and consistent manner. In the case of Fig. 4.2(a), where all four surrounding cells are fluid cells, Eq. (4.1) can be used directly without any special treatment. The four weighting coefficients are evaluated from the values of ϕ at the four fluid cells by inverting a 4×4 Vandermonde matrix:

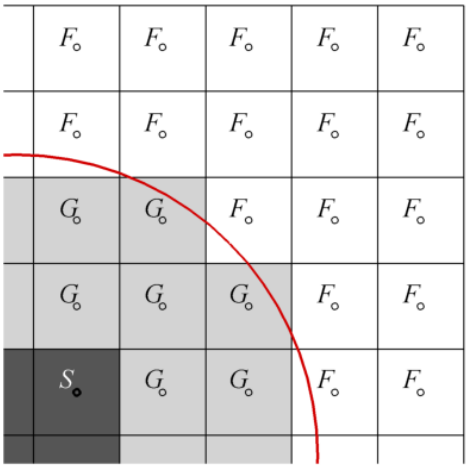

Figure 4.1: Schematic showing solid $\boldsymbol{S}$, fluid $\boldsymbol{F}$, and ghost $\boldsymbol{G}$ cells in the ghost-cell based immersed boundary method.

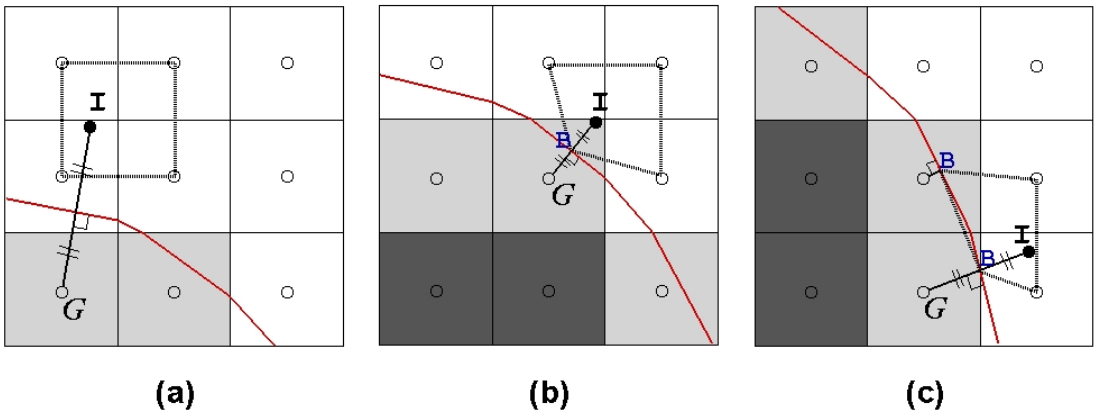

Figure 4.2: Schematic of bi-linear interpolation points when (a) all surrounding cells are fluid cells, (b) one surrounding cell lies inside the surface boundary, and (c) two surrounding cells lie inside the surface boundary.

$$\begin{bmatrix} C_1 \\ C_2 \\ C_3 \\ C_4 \end{bmatrix} = \begin{bmatrix} x_1y_1 & x_1 & y_1 & 1 \\ x_2y_2 & x_2 & y_2 & 1 \\ x_3y_3 & x_3 & y_3 & 1 \\ x_4y_4 & x_4 & y_4 & 1 \end{bmatrix}^{-1} \begin{bmatrix} \phi_1 \\ \phi_2 \\ \phi_3 \\ \phi_4 \end{bmatrix} \tag{4.2}$$

If one surrounding cell lies inside the surface boundary as illustrated in Fig. 4.2(b), using the ghost cell point in the interpolation scheme will cause an ill-posedness problem. The interpolation point is modified to replace the ghost point by its normal boundary intercept (B in Fig. 4.2(b)). In this case, the last row in the Vandermonde matrix Eq. (4.2) is replaced by

$$\phi_B(x, y) = C_1x_By_B + C_2x_B + C_3y_B + C_4. \tag{4.3}$$

Dirichlet boundary conditions are employed to determine the velocity components. For example, no-slip boundary condition ($u_n = 0, u_t = 0$) is imposed at the wall and hence the corresponding matrix to Eq. (4.2) for the case of $\phi = u_n$ or $\phi = u_t$ becomes

$$\begin{bmatrix} C_1 \\ C_2 \\ C_3 \\ C_4 \end{bmatrix} = \begin{bmatrix} x_1y_1 & x_1 & y_1 & 1 \\ x_2y_2 & x_2 & y_2 & 1 \\ x_3y_3 & x_3 & y_3 & 1 \\ x_By_B & x_B & y_B & 1 \end{bmatrix}^{-1} \begin{bmatrix} \phi_1 \\ \phi_2 \\ \phi_3 \\ 0 \end{bmatrix} \tag{4.4}$$

Assuming an adiabatic wall, homogeneous Neumann boundary conditions, $\frac{\partial \phi}{\partial n} = 0$, are applied for quantities such as pressure and density. With some algebra, the gradient of ϕ is then expressed as

$$\frac{\partial \phi}{\partial n} = C_1(y_Bn_x + x_Bn_y) + C_2n_x + C_3n_y = 0 \tag{4.5}$$

Consequently, the corresponding Vandermonde matrix becomes

$$\begin{bmatrix} C_1 \\ C_2 \\ C_3 \\ C_4 \end{bmatrix} = \begin{bmatrix} x_1y_1 & x_1 & y_1 & 1 \\ x_2y_2 & x_2 & y_2 & 1 \\ x_3y_3 & x_3 & y_3 & 1 \\ (y_Bn_x + x_Bn_y) & n_x & n_y & 0 \end{bmatrix}^{-1} \begin{bmatrix} \phi_1 \\ \phi_2 \\ \phi_3 \\ 0 \end{bmatrix} \tag{4.6}$$

If two surrounding cells lie inside the surface boundary (Fig. 4.2c), the above step repeats for the second point, resulting in Vandermonde matrix where the third row is also replaced by Eq. (4.3) or Eq. (4.5), depending on the boundary condition. With the flow variables at the image point expressed in terms of the surrounding nodes and boundary values, the flow variables at the ghost node can now be evaluated. For this, linear interpolation along the wall-normal direction is employed, and the value at the ghost cell node is obtained as

$$\phi_G = \zeta\phi_I + \Gamma \tag{4.7}$$

For a Dirichlet boundary condition, $\Gamma = 2\phi_B$ and $\zeta = -1$. A no-slip boundary condition reduces Eq. (4.7) for the velocities to $\phi_G = -\phi_I$. For Neumann boundary condition, $\Gamma = \frac{\partial\phi}{\partial n} \cdot \Delta l$ and $\zeta = 1$ where Δl is the length of the normal segment between the image and ghost points. An adiabatic wall then reduces Eq. (4.7) for pressure and density to $\phi_G = \phi_I$. The values at the ghost cell are obtained from the corresponding image point and these values are used in the computations of any cell interface flux that involves a ghost cell at the left or right solution state. These ghost cells implicitly satisfy the boundary conditions on the immersed interface. For three-dimensional flows, one needs to extend the above method in a straightforward manner using a tri-linear interpolation method with six interpolation stencils. The finite volume formulation of Eq. (3.26) can be now used consistently, even in the vicinity of the boundary (Fig. 4.3 for a two-dimensional depiction), to perform a wall-resolved LES.

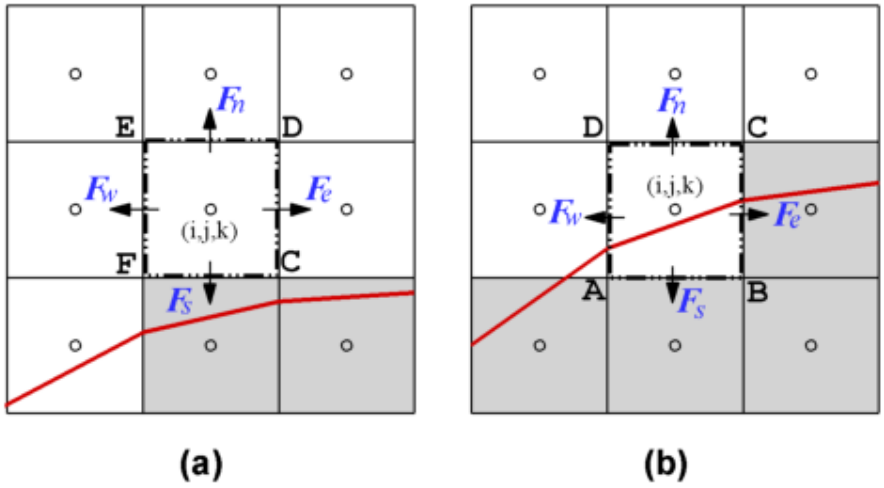

Figure 4.3: Treatment of a fluid cell in the vicinity of the immersed boundary when the immersed boundary cuts across (a) the ghost cell, and (b) the fluid cell. (F_e, F_w, F_n and F_s denote $F_{i+1/2,j}$, $F_{i-1/2,j}$, $F_{i,j+1/2}$, and $F_{i,j-1/2}$, respectively.)

4.2.2 Ghost-cell based cut-cell method (GC-CCM)

In the immersed boundary method described in Section 4.2.1, the exact shape of the fluid cells in the vicinity of the solid boundary is not detailed and this results in the loss or gain of mass and momentum. In the ghost-cell based cut-cell method (GC-CCM) introduced in this research, additional work is required to the finite-volume approach outlined in Section 4.2.1 such that the underlying conservation laws are guaranteed. This method extends conservative cut-cell method of Meyer *et al.* [74] and ghost cell approach of Tseng and Ferziger [112]. First, an additional type called *cut cell* ***C*** is identified (Fig. 4.4(a)). The solid boundary is represented by a series of piecewise linear segments. Based on this representation of the boundary, *cut cells* are defined as the fluid cells that are intersected by the solid boundary. A fluid subset of a ghost cell with a volume fraction less than 0.5 of a full-sized cell is called a small-cell. The presence of small cells restricts the maximum time step that can be used for the integration when an explicit time marching method is applied. This results in the numerical instability and stiffness of the system of equations, known as the *"small-cell problem"*. There are a number of approaches reported in the

literature to address this problem, such as cell merging [123, 88, 87, 52], cell linking [56], and combined merging/linking [46]. In the present work, the simple and straightforward merging algorithm of Ye *et al.* [123] is extended. Here, cut cells are reshaped by merging the small cells (merged cut-cell, Fig. 4.5(a)), or by discarding the portion that lies in the ghost cells (non-merged cut-cell, Fig. 4.5(b)). The shape of a cut-cell depends on the location and local orientation of the solid boundary. Each small cell is paired with a neighbouring fluid cell which is not yet assigned to another small cell. Details of the reshaping procedure can be found in Udaykumar *et al.* [114]. Fig. 4.4(b) provides an illustration of two-dimensional Cartesian grid showing non-merged and merged cut-cells. In contrast to the other cut-cell methods [87, 88], flow variables are not stored in the small cells (although the ghost cells store flow variables). In contrast to Ji *et al.* [52], the flow variables are not required to be at the true cut-cell centroid either. The storage locations of the flow variables are unchanged from the Cartesian cell centre. Since the computation of true cut-cell centroid is avoided, this approach results in a simpler algorithm than those that require the centroid computations (*e.g.* [52, 47]).

The numerical scheme described in Chapter 3 should be modified in the vicinity of the boundary such that it is consistent with the finite volume formulation and preserves the actual volume ratio as well. This section reports an extended version of the conservative immersed-interface method of Meyer *et al.* [74]. Consider a merged cell $ABCDEF$ shown in Fig. 4.5(a). The cell face EA is composed of two segments, EF and FA. The integral on this face can be decomposed and approximated as

$$\int_{EA} F dy = \int_{EF} F dy + \int_{FA} F dy \approx F_w(y_E - y_F)\Delta z + F_{sw}(y_F - y_A)\Delta z \tag{4.8}$$

where Δz denotes the grid step along the direction normal to the representation plane in Fig. 4.5. The flux through each decomposed segment of the face is computed separately at the centre of the corresponding Cartesian cell interface. To accurately estimate the fluxes for the cut-cells, ghost cells are still defined as in the previous section. For instance, the velocities at the two ghost cells ($\bar{u}_{i,j-1,k}$, $\bar{u}_{i+1,j-1,k}$) in Fig. 4.5(a) are used to compute the right solution state for the flux F_{sw}. Having the flow variables at these ghost nodes, the

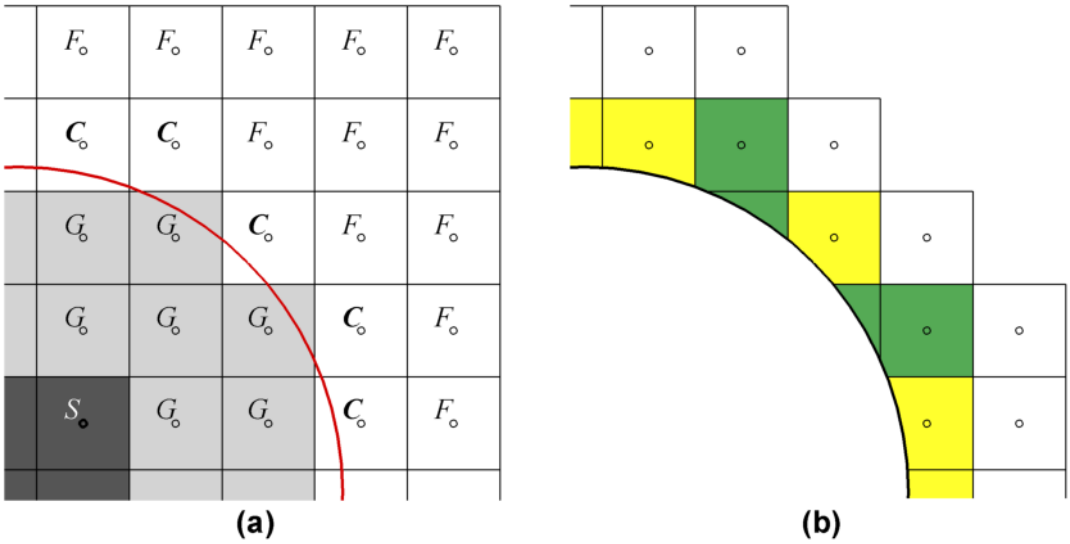

Figure 4.4: (a) Schematic showing solid $\boldsymbol{S}$, fluid $\boldsymbol{F}$, ghost $\boldsymbol{G}$ and cut $\boldsymbol{C}$ cells in the ghost-cell based cut-cell method. (b) An illustration of non-merged (in yellow) and merged (in green) cells.

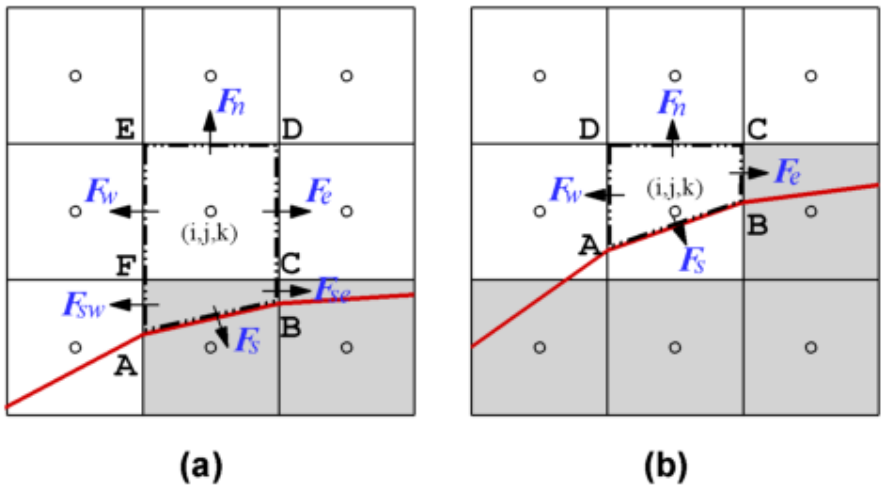

Figure 4.5: Schematic of a cut-cell showing various fluxes required. (a) Merged cell (b) Non-merged cell

piecewise linear reconstruction remains unchanged even in the vicinity of the boundary. Ghost cells are similarly used in [87] and [88] in their calculations but it was arbitrarily assumed that the variables in the ghost cells are equal to the values in the neighbouring fluid cells, leading to a scheme that is relatively less accurate in the vicinity of the boundary. Ghost cells are also similarly employed in [73] but on a single face structure rather than being used locally for a decomposed face as suggested here.

The cell face DB is decomposed similarly; however, it is important to note that the decomposed cell face of CB cannot be treated in the same manner as the cell face FA because both left and right sides of CB are the ghost cells. The velocities at the ghost nodes are previously obtained by mirroring the velocities at the image point ($\phi_G = -\phi_I$), which is necessary when computing the flux across fluid/ghost cells to implicitly satisfy the no-slip boundary conditions. When computing the flux, such as F_{se} across ghost/ghost cells, it does not involve with any physical boundaries. Mirroring velocities of the image point is then not necessary; hence, the ghost cells are set as $\phi_G = \phi_I$ for the velocity components in this case, over-riding the Eq. (4.7). Other variables that involve Neumann boundary conditions (such as density and pressure) do not need any changes. The computations of fluxes F_w, F_e and F_n to second-order accuracy are straightforward and are treated in the same manner as any face of a fluid cell.

For a non-merged cell $ABCD$ as shown in Fig. 4.5(b), the cell face, DA is composed of one segment and the integral can be approximated as

$$\int_{DA} F dy \approx F_w(y_D - y_A)\Delta z \tag{4.9}$$

All the flux computations are treated similarly as those for the merged cell. Now the calculation of the flux F_s on cell face AB, which lies on the solid interface, is considered. Both inviscid and diffusive fluxes are needed on this face and they are evaluated at centre of the face. The primitive variables on the face are imposed from the Dirichlet and Neumann boundary conditions, and the inviscid fluxes are formed directly from these variables. Conditions of Dirichlet type are prescribed for the velocity in order to capture no-slip walls, while conditions of Neumann type are prescribed for pressure and density to model

the adiabatic wall. The diffusive flux is computed from the wall-shear stress and this will be explained later.

The overall methodology described above is extendable to three-dimensions. The finite volume formulation is maintained by taking into account face apertures ($A_{i,j,k}$ with $0 \leq A_{i,j,k} \leq 1$), volume fraction ($\alpha_{i,j,k}$ with $0 \leq \alpha_{i,j,k} \leq 1.5$) and immersed interface $\Gamma_{i,j,k}$ (Fig. 4.6). Now that all the directional fluxes are determined for each cut cell, the fluid volume fraction $\alpha_{i,j,k}$ is computed to estimate its fluid cell volume $V_{i,j,k} = \alpha_{i,j,k}\Delta x\Delta y\Delta z$. The cell faces, $A_{i\pm1/2,j,k}\Delta y\Delta z$, $A_{i,j\pm1/2,k}\Delta x\Delta z$, and $A_{i,j,k\pm1/2}\Delta x\Delta y$, are determined to integrate the fluxes over the real wetted surfaces of the control volume $V_{i,j,k} = \alpha_{i,j,k}\Delta x\Delta y\Delta z$. With reference to Fig. 4.5(a), the cell face $A_{i-1/2,j,k}\Delta y\Delta z$ consists of $(A_{i-1/2,j,k}\Delta y\Delta z)_w$ and $(A_{i-1/2,j,k}\Delta y\Delta z)_{sw}$, where $(A_{i-1/2,j,k})_w = 1$, to account for the fluxes f_w and f_{sw} separately. Other faces can be referenced similarly. The Eq. (3.26) for a cut cell is then modified as

$$
\begin{aligned}
f^n &= f(U^n_{i,j,k}, t^n) \\
&= \frac{\sum_{l=1}^{2}(A_{i+1/2,j,k}\bar{\mathbf{F}}_{i+1/2,j,k})_l - \sum_{m=1}^{2}(A_{i-1/2,j,k}\bar{\mathbf{F}}_{i-1/2,j,k})_m}{\alpha_{i,j,k}\Delta x} \\
&+ \frac{\sum_{n=1}^{2}(A_{i,j+1/2,k}\bar{\mathbf{F}}_{i,j+1/2,k})_n - \sum_{p=1}^{2}(A_{i,j-1/2,k}\bar{\mathbf{F}}_{i,j-1/2,k})_p}{\alpha_{i,j,k}\Delta y} \\
&+ \frac{\sum_{q=1}^{2}(A_{i,j,k+1/2}\bar{\mathbf{F}}_{i,j,k+1/2})_q - \sum_{r=1}^{2}(A_{i,j,k-1/2}\bar{\mathbf{F}}_{i,j,k-1/2})_r}{\alpha_{i,j,k}\Delta z} \\
&+ \frac{\mathbf{C}+\mathbf{D}}{\alpha_{i,j,k}\Delta x\Delta y\Delta z}
\end{aligned}
\tag{4.10}
$$

where $\mathbf{C}$ and $\mathbf{D}$ represent the inviscid and diffusive forces across the immersed interface $\Gamma_{i,j,k}$, equivalent to those on cell face AB in Fig. 4.5 as explained above. The diffusive flux $\mathbf{D}$ in Eq. (4.10) can be calculated from the wall-shear stress as

$$\mathbf{D} = -\int_{\Gamma_{i,j,k}} \tau_w dS \tag{4.11}$$

The wall-shear stress τ_w can be solved (*e.g.* [74, 73]) or modelled (*e.g.* [13, 12, 94]), depending on one's demand for accuracy and computational cost. When the wall-shear stress is to be solved, the above finite volume formulation can be used to perform a wall-resolved LES. The mesh refinements are typically needed in this case and it is needed in all three directions as the reduction in the turbulent scale near the wall occurs in all three directions.

For normal cells away from the solid interface, the face aperture $A_{i,j,k}$ and the volume fraction $\alpha_{i,j,k}$ become unity (and no decomposition of cell face takes place) thereby automatically reducing the Eq.(4.10) to the normal finite volume formulation, Eq. (3.26).

4.2.3 Wall modelling for non-body conforming grids

LES cannot resolve the eddies accurately unless a very fine mesh is employed. In a non-body conformal method, the mesh refinements are needed in all three directions although the requirements of grid resolution are much more demanding along the wall-normal direction. This is because no grid direction is, in general, normal to the body. It is therefore necessary to refine the grid along any direction in order to increase the grid resolution along the normal direction. In the immersed boundary method, the wall gradients are substantially under-predicted on coarse grids. The error from the mass conservation also increases on coarse grids. In an effort to achieve a substantial reduction in the resolution requirements for high Reynolds number near-wall flows while maintaining a realistic description of the effects, the wall-shear stress, τ_w, is estimated using a simple wall model in this work such that coarse grids are used. The simple wall model used in this work is analogous to the wall functions commonly used in RANS approach, except that it is applied in the instantaneous sense in time-accurate calculations. Other types of wall models can be easily added in this scheme if necessary. Various wall modelling approaches are extensively investigated in [107] with different sub-grid scale models in the context of LES on coarse body fitted grids.

The aim of wall functions is to skip the direct resolution of the viscous sub-layer near the wall so that the near-wall grids can be coarser to be related to the larger eddies developing in the fluid core. To correctly approximate the near-wall behaviour, law of the wall approximation is required to return the correct instantaneous wall-shear stress corresponding to the known instantaneous velocity at the first node closest to the wall. The wall-shear stress is then used to satisfy the wall boundary condition. When using the wall function, the first node closest to the wall needs to be ideally located in the log-law region; however, with the immersed interface which cuts the Cartesian cell in a random manner, some nodes closest to the wall will be inevitably located in the viscous sublayer or in the buffer layer. To account for the smooth transition between the linear and the logarithmic region in the buffer layer, a three-layer wall model is used based on the assumption that the near-wall layer consists of a fully viscous sublayer ($y^+ \leq 5$), fully turbulent superlayer ($y^+ > 30$) and a buffer layer in between ($5 < y^+ \leq 30$). The formulation is as follow [8]

$$u^+ = \begin{cases} y^+ & if\ y^+ \leq 5 \\ A\ ln(y^+) + B & if\ 5 < y^+ \leq 30 \\ K^{-1}\ ln(Ey^+) & if\ y^+ > 30 \end{cases} \tag{4.12}$$

where K is the von Karman constant ($K \approx 0.42$), u^+ is the dimensionless resolved velocity tangential to the wall ($u^+ = u_t/u_\tau$), y^+ is the non-dimensional wall distance ($y^+ = \Delta h u_\tau/\nu$), and u_τ is the friction velocity ($u_\tau = \sqrt{\tau_w/\rho}$). u_t is the velocity component at the node P in the wall tangential direction and Δh is the distance of the near-wall node P to the solid surface (Fig. 4.6(b)). The constants, E, A and B are set as $E = 9.8$, $A = (K^{-1}ln(30E) - 5)/ln(6)$ and $B = 5 - A\ ln(5)$, which are simply taken from [8]. An iterative procedure is implemented to solve y^+ since the friction velocity u_τ is required to determine y^+ which, in turn, depends on the wall-shear stress. It is important to note that, since u_τ is computed using the wall-shear stress, the near-wall velocity and the wall-shear stress are rigidly linked in this wall model. This can cause an inaccurate approximation of the wall-shear stress if the near-wall flow separates significantly. This model also implies the logarithmic law of the wall for the mean velocity, which is not valid in many complex

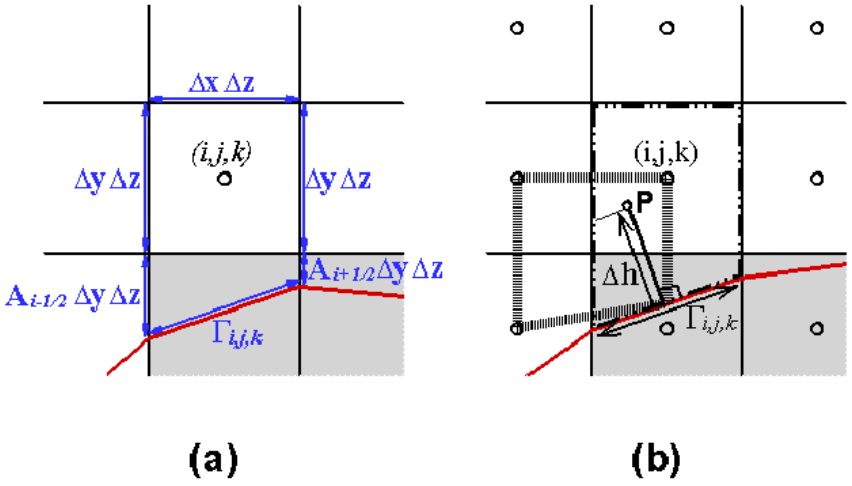

Figure 4.6: (a) Schematic of wetted surface and immersed interface for a cut-cell (i, j, k). (b) Schematic of bi-linear interpolation points for the tangential velocity at P in a cut-cell.

flows especially if separation is present. It is however the simplest model available and it is still widely used especially in studies where the computational efficiency is of most interest. In the future, better wall modelling strategies should be investigated.

In the case of body fitted methods, the near-wall node P is a computational node, hence, the tangential velocity u_t and the distance to the wall Δh can be obtained in a straightforward manner. In the non-body conformal methods, the wall-normal direction does not necessarily coincide with computational nodes, hence, an interpolation procedure is needed for the calculation of the tangential velocity at the near-wall node P. The distance Δh is somewhat arbitrary and needs to be related to the cell volume. The definition of Δh used in Meyer *et al.* [74] is followed:

$$\Delta h = 0.5\sqrt{(\Delta x \cdot n_{\perp,x})^2 + (\Delta y \cdot n_{\perp,y})^2 + (\Delta z \cdot n_{\perp,z})^2} \tag{4.13}$$

where Δx, Δy and Δz are the dimensions of the control volume (i, j, k), and, $n_{\perp,x}$,$n_{\perp,y}$ and $n_{\perp,z}$ are components of the normal vector on $\Gamma_{i,j,k}$. To compute the tangential velocity

at P, the tangential velocities of the surrounding nodes are first computed. Using these values, u_t at P is interpolated using bi-linear (2D) or tri-linear (3D) interpolation. The interpolation method here is similar to that described in Section 4.2.1, which is used to express the flow variables at the image point in terms of its surrounding nodes.

Chapter 5

LES of Compressible Flows using Non-Body Conformal Methods

5.1 Introduction

In order to validate the methodology described in the previous chapters, various test cases involving three-dimensional flow are performed for a wide range of Reynolds numbers as well as Mach numbers. The test-cases are divided into two parts: 1. low to moderate Reynolds number flow cases where wall-resolved LES is performed, and, 2. high Reynolds number flow cases where a simple wall model is employed and the LES is performed on a relatively coarse mesh.

All the numerical techniques described in the previous chapters are implemented in the compressible flow solver developed in-house. The solver is written in FORTRAN-90 which has been parallelized using the OpenMP standard directives. The three-dimensional computations in the present study involve up to 20.4×10^6 grid points and they have been performed locally on a single CPU or in parallel on 16 CPUs (Intel Xeon at 2.6 GHz on SHARCNET, www.sharcnet.ca). The converged results from the largest computations (the fine grid resolution case for the supersonic flow over a cylinder) was obtained in approximately 28 days.

5.2 Wall-resolved LES of moderate Reynolds number flows

For simulations involving low to moderate Reynolds number where sufficiently fine near-wall grids are feasible, a wall-resolved LES is performed. For those cases, the error on mass conservation stays moderate such that the use of GC-IBM (Sec. 4.2.1) is sufficient without the need for additional work to guarantee the underlying conservation laws (*i.e.* GC-CCM of Sec. 4.2.2). Three test cases are prepared here using GC-IBM with the near-wall resolved grids. First, a three-dimensional subsonic flow ($Re = 300$) past a circular cylinder has been simulated at a low Reynolds number. Second, the method is then applied to LES of turbulent flows ($Re = 6700$) over a wavy surface. Lastly, the method is applied to LES of a supersonic turbulent flow ($M_\infty = 2.0$ and $Re = 7000$) over a circular cylinder. The results of these three test cases have been published by the author in [78].

5.2.1 Subsonic flow over a cylinder

A three-dimensional flow past a circular cylinder, immersed in an unbounded uniform flow, has been simulated at a low Reynolds number of $Re = 300$. The Reynolds number is defined as $Re = U_\infty D/\nu$ where D is the cylinder diameter, U_∞ is the free stream velocity and ν is the kinematic viscosity. It should be noted that the cylinder wake is intrinsically three-dimensional at this Reynolds number, therefore two-dimensional simulations are not expected to produce flow fields that would match corresponding experiments [76]. The simulations have been performed in a relatively large rectangular domain of $30D \times 20D$ in the x and y direction respectively in order to minimize the effect of the outer boundary on the development of the wake and to ensure that the results presented here are independent of the domain size. The flow is compressible with constant viscosity and specific heat ratio. At the inflow, subsonic non-reflecting inflow boundary conditions are implemented. At the three other sides of the domain (excluding the spanwise boundaries), subsonic non-reflecting outflow conditions are used. These boundary treatments are explained in the Sec. 3.4.2. The free stream Mach number is kept at a low value of 0.2 in order to minimize the

compressibility effect. This is because the reference experimental data and the numerical solutions that the current results are comparing with are in the incompressible flow regime. In order to demonstrate that the current method is also capable of providing accurate results at a sufficiently high Mach number, a separate simulation of a supersonic flow over a circular cylinder is also performed and this will be discussed later. In this current three-dimensional case, the spanwise domain size was chosen to be $3D$ and periodic boundary conditions are employed in this spanwise ($z-$) direction. This size was used and verified by Ghias *et al.* [33]. The no-slip condition is imposed at the surface of circular cylinder via the IBM methodology described in Sec. 4.2.1.

Three simulations with a different grid resolution are carried out: the coarse grid case on a $202 \times 164 \times 49$ Cartesian grid, the medium grid case on a $300 \times 200 \times 49$ Cartesian grid, and the fine grid case on a $400 \times 320 \times 49$ Cartesian grid. In the streamwise and cross-stream directions the grid is stretched to have a higher resolution in the vicinity of the cylinder. Here, Δx and Δy in the vicinity of the circular cylinder are $0.04D$ for the coarse grid (see Fig. 5.1), $0.025D$ for the medium grid and $0.02D$ for the fine grid. Their average values of y^+ corresponding to the first grid point away from the cylinder surface are approximately 1.08, 0.50 and 0.41, respectively. In the spanwise direction Δz is uniform. In Fig. 5.2 the flow is visualized by isosurfaces of instantaneous z-component of vorticity in the wake at one time instant. This highlights the large coherent flow structure in the wake region which is similar to those observed in Ghias *et al.* [33].

The time-averaged surface pressure and skin friction coefficient are provided in Fig. 5.3 with the available body-conforming numerical [89] and measurement data [109, 23]. It is important to note that, the computations of these quantities are based on the evaluation of surface pressure and wall shear stress, and they are not trivial to compute in the non-body conforming method. This is because different interpolations to estimate the surface pressure or wall shear stress yields a slightly different coefficients. The discrepancies are less significant for a grid with a higher resolution near the wall. In the current solver, for simplicity at the expense of minor accuracy sacrifice, the pressure is taken from the cell centre of the nearest fluid cell whose distance to the immersed boundary varies between the size of the fluid cell. Shear stress at the surface is also computed in a straightforward

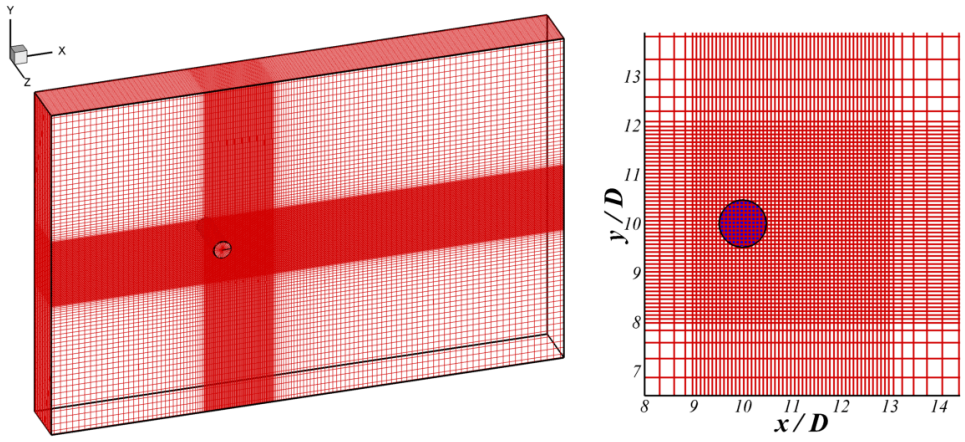

Figure 5.1: The rectangular Cartesian grid domain of a coarse case and a close up view of the grid around the cylinder in the x-y plane. Every third grid point is shown.

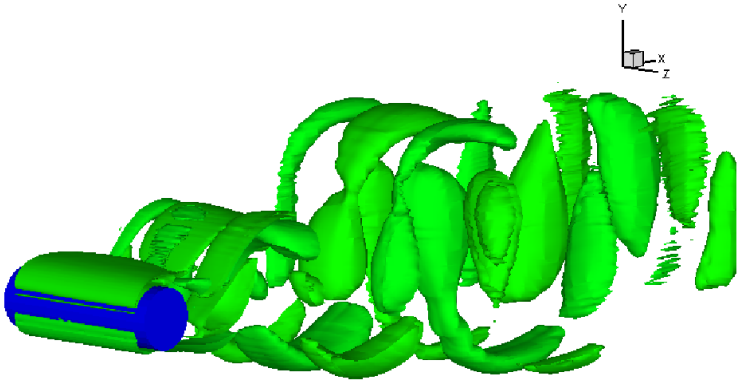

Figure 5.2: Isosurfaces of transverse vorticity magnitude at an instant of time in the vicinity of the circular cylinder ($Re = 300$)

manner by using the tangential (to the immersed boundary) component of the velocity (u_t) at this cell centre and its local distance to the boundary (Δn) via $\tau_w = \mu \frac{\Delta u_t}{\Delta n}$. Comparing the results in Fig. 5.3, it shows that, while the coarse grid solution may not be in a good agreement with the other two, medium and fine grid solutions do show an excellent agreement with the measurement and hence confirms the validity of the current approach. For a quantitative study, drag and lift coefficients are computed and compared to the established data. Integrating the computed surface pressure and shear stress fields over the cylinder surface at each time step, the total force on the surface is evaluated. Then, the drag and lift coefficients are computed according to the expressions: $C_D = F_D/(\frac{1}{2}\rho_\infty {U_\infty}^2 A)$ and $C_L = F_L/(\frac{1}{2}\rho_\infty {U_\infty}^2 A)$, where F_D and F_L are the drag and lift forces, respectively, and $A = D \cdot l_{spanwise}$

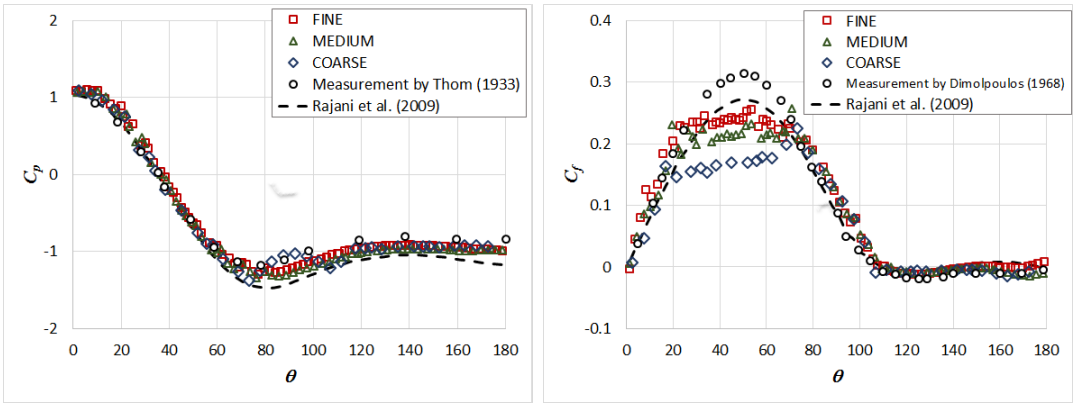

(a) Pressure distribution

(b) Friction distribution

Figure 5.3: Distribution of pressure and skin-friction coefficient along the surface of the cylinder at $Re = 300$.

The variation of C_D and C_L as a function of non-dimensional time are plotted in Fig. 5.4 for the medium grid case. Their time averaged drag coefficient, the root mean square of the lift coefficient, and the Strouhal number are summarized in Table 5.1 along with other corresponding numerical and experimental results for a comparison. The lift variation is used to compute the vortex shedding Strouhal number defined as $S_t = fD/U_\infty$, where f is the vortex shedding frequency. This simulation serves to demonstrate that the current

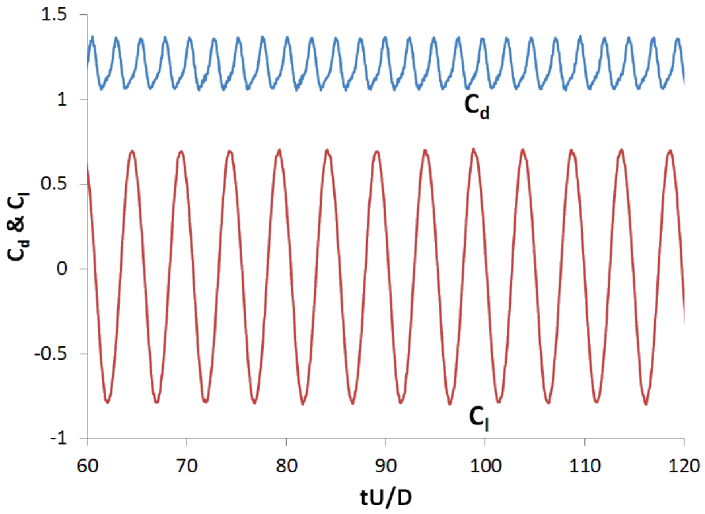

Figure 5.4: Temporal variation of drag and lift coefficient for the medium mesh case.

methodology is capable of resolving thin boundary layers around the immersed boundary.

5.2.2 Flow over a wavy surface

Next, LES is employed to simulate the turbulent flows over a wavy boundary. This is an interesting test case because the geometrical configuration is fairly simple, and yet the flow pattern is complicated. The flow is subject to the effects of alternating convex and concave curvatures. Important dynamical features of a turbulent flow over wavy topography can be revealed by studying the instantaneous flow fields. When the flow speeds up to its maximum magnitude at just downstream of the crest, it separates and starts to form a small recirculation zone which grows as the flow slows down. Here, the flow can be categorized into regions that have unique characteristics. These include the outer region, recirculation region, boundary layer region, shear layer region, separation region, and reattachment region ([10]). Studies of this test case are still rare to date. Using an incompressible flow solver, several efforts have been made on a body-fitted mesh employing a DNS (see [106] and literature cited therein) or LES [127]. On a non-body conformal mesh, [112] and [2]

Table 5.1: Comparison of time averaged drag coefficient C_{D_p} and C_{D_f}, root-mean-square of lift coefficient $C_L(rms)$, mean back pressure coefficient C_{Pb}, and Strouhal number S_t with other simulations and experiments.

Case	C_{D_p}	C_{D_f}	C_D	$C_L(rms)$	C_{Pb}	S_t
present case (coarse)	1.07	0.14	1.21	0.47	-0.94	0.20
present case (medium)	1.15	0.18	1.33	0.53	-0.99	0.21
present case (fine)	1.14	0.19	1.33	0.55	-0.99	0.21
[89] (radial polar grid)	-	-	1.28	0.50	-1.01	0.195
[2] (incompressible IBM)	-	-	1.27	0.42	-	0.21
[123] (incompressible IBM)	-	-	1.38	0.65	-1.22	0.21
[33] (compressible IBM)	-	-	1.23		-1.00	0.21
[122] (measurement)	-	-	1.22	-	-0.96	0.203

successfully performed LES of turbulent flow over a wavy surface using an IBM approach. For compressible flows, there is one publication [106] which reported the DNS results for turbulent flows over wavy wall geometries on a body-fitted mesh. They employed high order convection (6th-order WENO) and diffusion (4th-order central difference) schemes. To the best of author's knowledge, it has not been tested on a non-body conformal mesh using compressible flow formulations. Obtaining an accurate representation of the detailed flow dynamics in the case of non-body conforming method is extremely challenging because the dynamics of the flow is strongly influenced by the physics of the small scale eddies that are developing close to the wall primarily due to the wall shear stress. A proper evaluation of sub-grid scale terms in the vicinity of immersed boundaries has a substantial effect on the accuracy and efficiency of the overall method. In the case of simulating a plane channel flow using a compressible LES solver, a higher order spatial scheme is generally favoured over a low order scheme as the latter (when using the Smagorinsky model) is overly dissipative near the wall [41]. The latter issue can be avoided with a finer resolution of grid as a coarse resolution grid tests the employed discretization scheme more severely. In this work, a second-order scheme is used with the standard Smagorinsky model as a subgrid-scale model. It is well known that this model, as well as most of subgrid viscosity models, does not exhibit the correct behaviour in the vicinity of solid walls. To alleviate the problem, the van Driest damping function is added here in order to artificially reduce

the eddy viscosity near the wall. Three different grid resolutions (coarse, medium, fine) are employed here in order to study the grid sensitivity to solutions. The basic configurations are similar to that of a channel flow except that the bottom boundary wall mimics the transverse ripples given by $y_w = a\cos(\frac{2\pi x}{\lambda})$ where $a = 0.1$ is the amplitude of the wave and λ is the wavelength. The non-dimensional size of the computational domain is $4 \times 2 \times 2$ in the $x-$, $y-$ and $z-$ directions respectively. The wavelength has the size of $\lambda = 2$ and the average height of the channel h is such that $h = \lambda$. The lower wall has two full sinusoidal shapes. The coarse grid employs $160 \times 165 \times 80$ cells (Fig. 5.5). This grid resolution is finer than the resolution with which the grid independent solutions were achieved in a similar work in the corresponding incompressible LES framework [2]. The medium and fine grids here employ $200 \times 305 \times 80$ and $250 \times 385 \times 80$ cells, respectively. In all cases, grid stretching is utilized in the wall normal ($y-$) direction (on both the upper and lower walls) to resolve the near wall layer as in the plane channel flow. To ensure proper resolution of the thin boundary layers at the bottom wall, a very fine and uniform wall-normal grid spacings are used in the vicinity of the wavy boundary such that $\Delta y/h$ is 0.004, 0.002 and 0.0015 for the coarse, medium and fine grid cases, respectively. After the solutions are obtained their corresponding average y^+ values on the first grid cell adjacent to walls are found to be 0.47, 0.17 and 0.13. In the streamwise and spanwise directions the grid spacings (Δx and Δz) are uniform. The upper and lower boundary walls are solid no-slip walls. The Reynolds number based on the mean velocity and the average height of the channel is set to be approximately 7000. A similar configuration was used in the LES study in [10, 2].

The initial flow at a Mach number of 0.2 is given in the channel. Then the periodic boundary conditions are employed in the streamwise and spanwise directions. To ensure that global mass conservation based on bulk velocity is satisfied, the total mass flow rates going out of and coming into the domain are first computed. To make the mass flow rate out equal to the mass flow rate coming in, all the outlet velocity components at the downstream outlet plane are corrected by the ratio of these two mass flow rates. Fig. 5.6 shows the isolines of mean streamwise velocity normalized by bulk velocity, U_b. A qualitative observation reveals that the dominant flow structures are well captured in

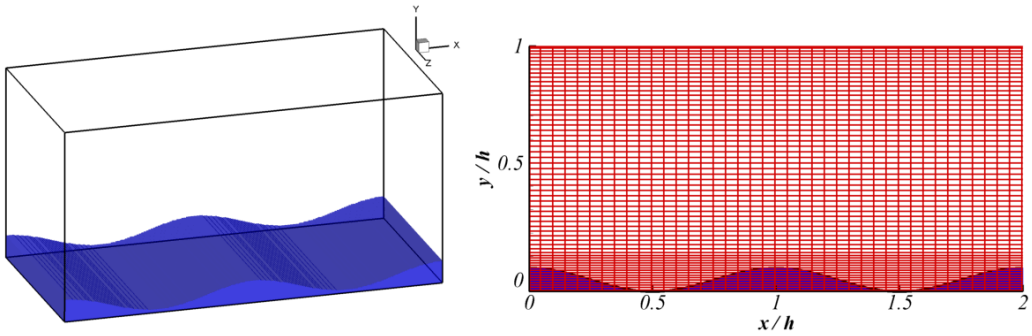

Figure 5.5: The computational domain and the underline grids (coarse case) for flow over a wavy boundary in the X-Y plane. Every fifth grid point is shown.

the present simulation. The recirculation zone, characterized by large oscillations in the mean velocity, appears behind the crest followed by a strong velocity gradient on the hill as anticipated. This recirculating area, however, appears to be excessively large for the coarse mesh case when compared to the medium/fine mesh case as well as the work by others [14, 2, 10]. The locations of predicted mean (time- and spanwise-averaged) separation and reattachment point, defined as locations where wall shear stress vanishes, are given in Table 5.2 for both cases in comparison with other reference work. In the case of coarse mesh, it is believed that the dynamics of the reattaching flow is altered by the persistence of small-scale structures in the simulations obtained with the Smagorinsky's model. This was verified by Suksangpanomrung *et al.* [105], who found in their comparisons of different subgrid scale models in the LES framework, that small scale structures were much more prominent in the reattachment region for the Smagorinsky model. This is remedied by the high resolution mesh which reduces the effect of turbulence model by resolving smaller scale eddies.

For the purpose of conducting quantitative comparison with the DNS data [14], mean streamwise velocity profiles, at nine locations in one wavelength of the topography, are shown in Fig. 5.7. These probing stations are located in the second half of the domain in the streamwise direction (x/λ=1.1 to 1.9), after the flow passes the first crest. The overall agreement with the DNS data is reasonably good. In particular, the differences between

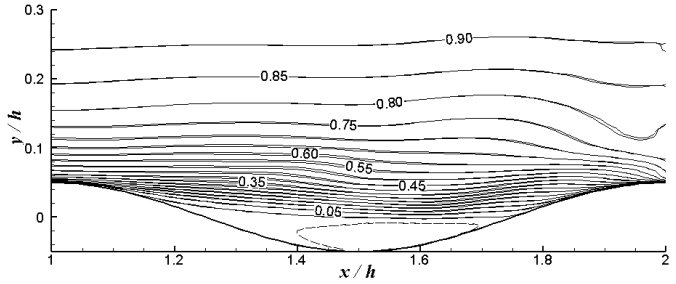

(a) coarse grid LES

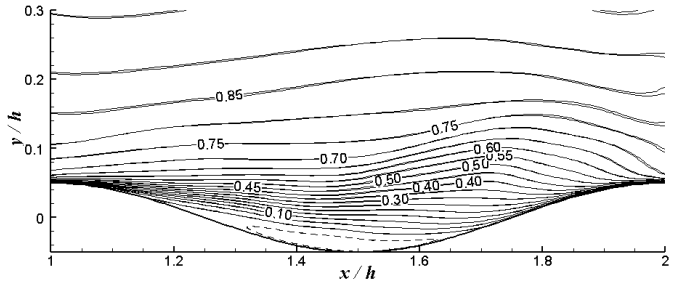

(b) medium grid LES

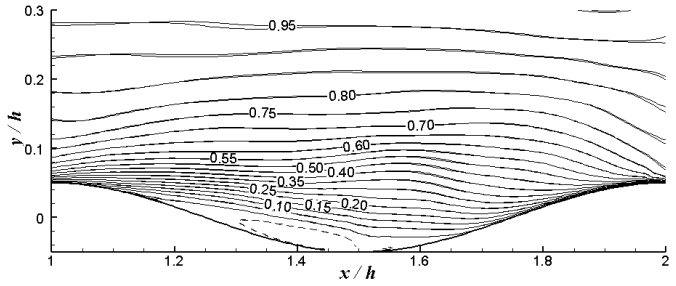

(c) fine grid LES

Figure 5.6: Contours of mean streamwise velocities normalized by bulk velocity U_b. (*dotted line*: zero mean velocity.)

Table 5.2: Locations of separation and reattachment point (x/λ) from the preceding wave crest

Case	Separation point	Reattachment point
present case (coarse)	0.14	0.73
present case (medium)	0.14	0.63
present case (fine)	0.14	0.58
Cherukat [14]	0.14	0.59
Balaras [2]	0.145	0.61
Calhoun [10]	0.14	0.61

the medium/fine grid and the DNS data are very small near the bottom wall. The coarse grid solutions show to have the back-flow which persists further away from the bottom wall due to its larger recirculation zone. From the outer region to the top wall, all three results show virtually no difference. A detailed comparisons of the mean velocities (streamwise and wall-normal) in the vicinity of the crest and trough are shown in Fig. 5.8. At the trough, the maximum mean back-flow velocities for both coarse and medium grids are over-predicted when compared to the DNS data due to the largely/slightly (for coarse/medium grid) over-predicted size of the recirculation zone. The fine grid results showed nearly no back-flow as the flow is nearly reattached. Despite the usage of the standard Smagorinsky model the turbulent intensity profiles shown in Fig. 5.9 agree reasonably fine with the DNS data near the wall. Away from the wall the turbulence is dissipated rapidly and as the grid is coarsened. An accurate turbulent spectrum can be obtained via more sophisticated turbulence models. Overall, a higher resolution grid provides a better prediction of the recirculation zone, and hence improves the overall quality of the mean flow-field.

5.2.3 Supersonic flow over a cylinder

Here, a supersonic flow past a circular cylinder at $Re = 7000$ and $M_\infty = 2.0$ is presented. The objective here is to demonstrate the robustness of the proposed immersed boundary method for higher Mach number flows. A preliminary work on the equivalent test case is reported by de Tullio and Iaccarino [21] where the authors briefly discussed the results

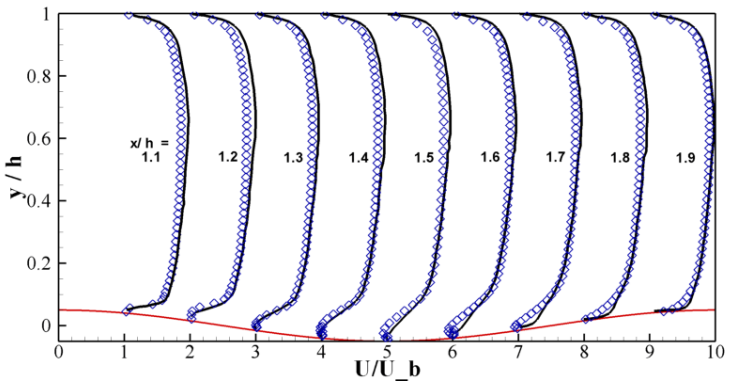

(a) coarse grid LES

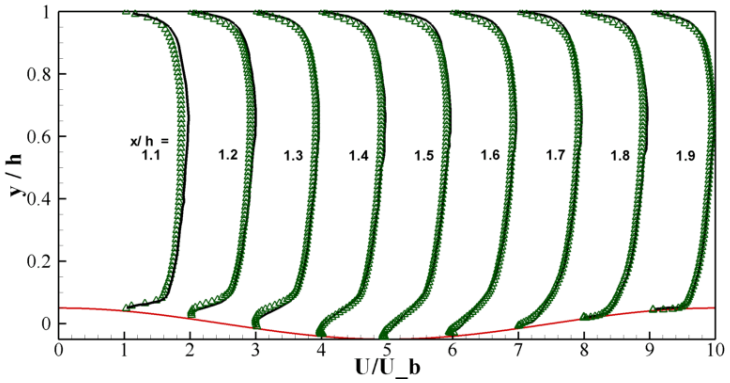

(b) medium grid LES

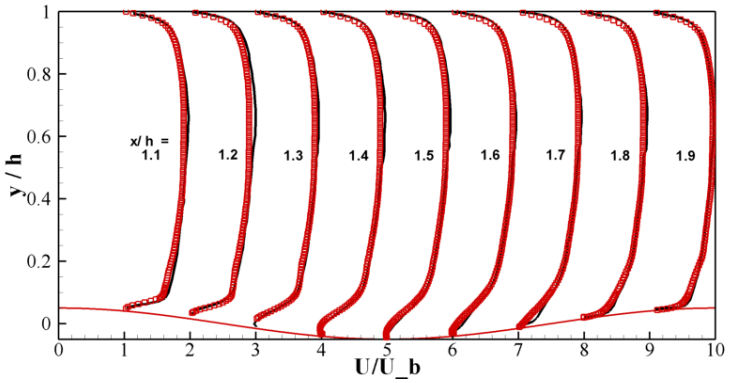

(c) fine grid LES

Figure 5.7: Profiles of mean streamwise velocities at locations for x/λ=1.1, 1.2, 1.3, 1.4, 1.5, 1.6, 1,7, 1.8, and 1.9 (−: DNS [14]). Every third grid point is shown.

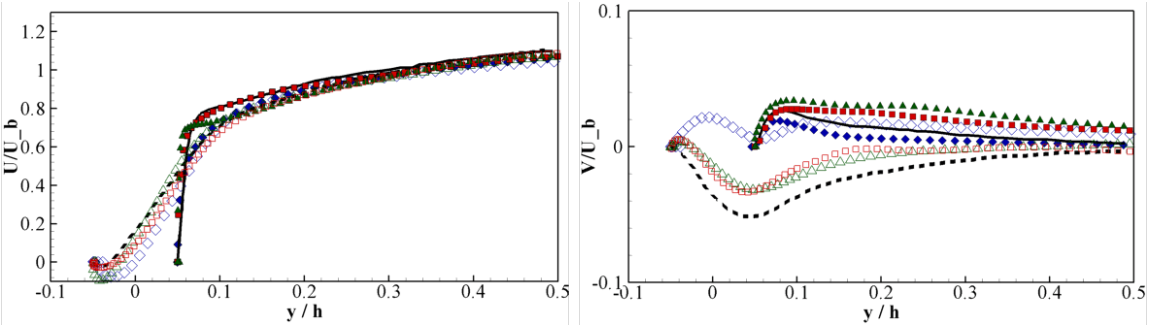

(a) streamwise (b) wall-normal

Figure 5.8: Mean streamwise and wall-normal velocities at crest and trough; (−: DNS [14]; ◊/△/□: coarse/medium/fine grid LES at trough; ♦/▲/■: coarse/medium/fine grid LES at crest).

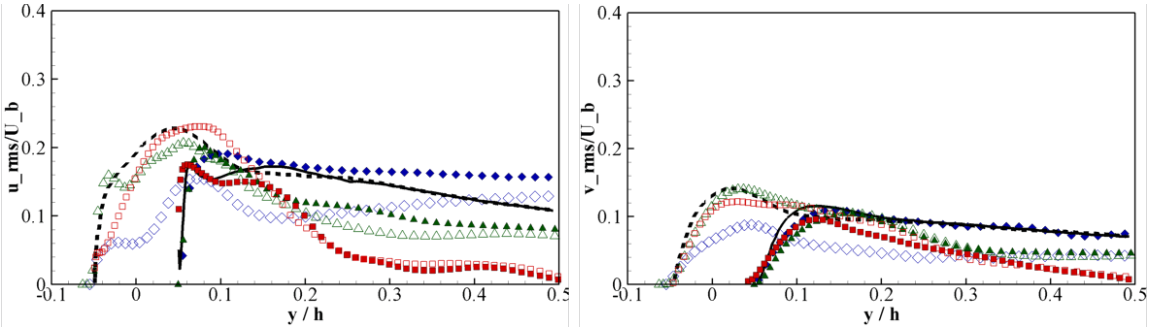

(a) streamwise (b) wall-normal

Figure 5.9: Streamwise and wall-normal RMS values; (−: DNS [14]; ◊/△/□: coarse/medium/fine grid LES at trough; ♦/▲/■: coarse/medium/fine grid LES at crest).

qualitatively with their pressure contours. There are a few other previously reported experimental and numerical work on supersonic and turbulent flow over a cylinder which were focused on high Reynolds numbers above 1.6×10^5 [30, 83, 9] using a two-dimensional IBM-RANS approach (in the case of numerical work). With the current (conventional) LES approach, in the absence of treatments such as a wall model and/or local grid refinement, work on such a highly turbulent flow is not competitive due to an extremely large number of grid cells required.

The simulations have been performed in the domain of $14D \times 14D \times 3D$ in the x, y and z direction respectively. The rest of the geometrical configurations are basically the same from the subsonic case presented earlier. Three non-uniform Cartesian grids have been employed for the computations: the coarse case on a $400 \times 200 \times 40$ grid, the medium case on a $600 \times 300 \times 40$ grid, and the fine case on a $850 \times 600 \times 40$ grid. The Δx and Δy in the vicinity of the circular cylinder are $0.02D$ for the coarse grid, $0.01D$ for the medium grid and $0.005D$ for the fine grid. Their average values of y^+ corresponding to the first grid point away from the cylinder are 4.36, 2.63 and 1.63, respectively. At the inlet, supersonic inflow boundary conditions are applied. For all other boundaries (excluding the spanwise boundaries) non-reflecting outflow conditions are applied. To include the effect of the turbulence, the standard Smagorinsky turbulence model is used again in conjunction with the van Driest damping function. All the simulations are performed in a three-dimensional domain but the results showed no three-dimensional cylinder wake. Fig. 5.10 provides a Mach number contours from the fine grid solution. Upstream of the cylinder, a bow shock is formed behind which the flow becomes subsonic. From right ahead of the cylinder, this subsonic flow travels along the cylinder surface and accelerates to form a supersonic region. This supersonic region is separated from the subsonic recirculation region that is directly behind the cylinder as shown by a long symmetric tail shock. The time-averaged surface pressure coefficient distributions along the surface of the cylinder are provided in Fig. 5.11. The drag coefficients based on the pressure coefficient for coarse, medium and fine grids are 0.929, 0.930, and 0.927, respectively. In spite of the inadequate resolution in the boundary layer region indicated by its near-wall y^+ values, the coarse grid solution converges well to the two other finer grid solutions. In all cases, the solutions clearly show all the flow

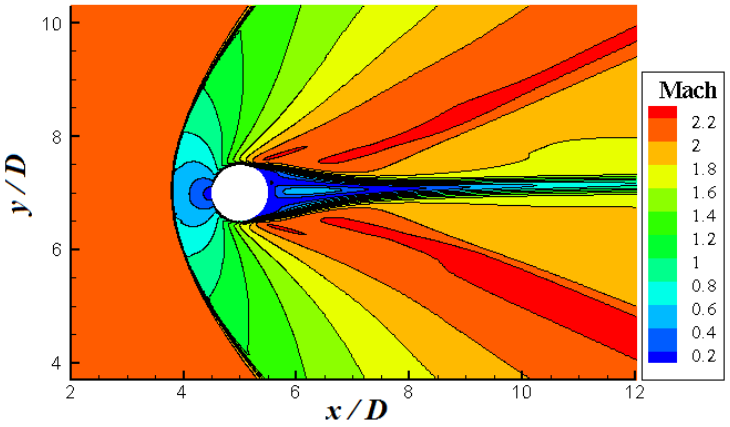

Figure 5.10: Mach number contours for a supersonic flow past a cylinder for $M_\infty = 2.0$ and $Re = 7000$ (fine case).

features associated with a supersonic flow past a cylinder.

5.3 LES of high Reynolds number flows using a wall model

For simulations involving high Reynolds number the wall-shear stress, τ_w, is estimated using a simple wall model such that a coarse mesh can be used. LES is then performed on non-body conformal grids. In the LES with wall models, explicit sub-grid scale models are strongly affected by the discretization errors in the large near-wall cells, and therefore cannot account properly for the turbulence in this region. Since the numerical diffusion in the shock-capturing scheme (such as the MUSCL scheme) is larger than the diffusion of the sub-grid scale models [32], the addition of an explicit sub-grid scale model is often unnecessary. An alternative approach of turbulence modelling technique is the implicit LES (or, MILES [6], Sec. 2.3.2) where the truncation error of the numerical discretization itself functions as a sub-grid scale model with no explicit modelling. The use of the MILES approach also further simplifies the numerical implementation. The accuracy and the

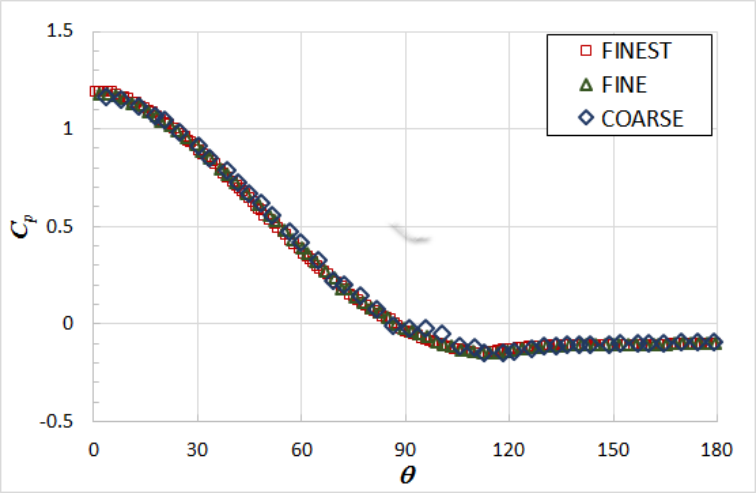

Figure 5.11: Distribution of pressure coefficient along the surface of the cylinder for $M_\infty = 2.0$ and $Re = 7000$.

performance of this implicit LES with the second order cut-cell method for turbulent flows has been well proven by Meyer *et al.* [75].

In the following LES simulations, the near-wall grid cells are relatively coarse due to the constraint imposed by the wall function. The usage of the wall functions dictates the near-wall grid resolution, and hence, a conventional grid convergence study is difficult to be applied when wall functions are employed. With variations of grid resolution, however, consistent results can be obtained as long as the constraint of the wall model with respect to the coupling position is satisfied [13]. For this reason, the order of accuracy is not investigated here. The order of accuracy in the vicinity of the boundary for GC-IBM and S-CCM is well discussed by others [112, 33, 52].

The selected test cases are: turbulent flow through an inclined channel, highly turbulent flow ($Re = 11200$) over a wavy surface, and a supersonic turbulent flow ($Re_D = 2 \times 10^5$ and $M_\infty = 1.7$) over a circular cylinder. The simulations are performed on three different types of non-body conformal grids: GC-IBM (Sec. 4.2.1), GC-CCM (Sec. 4.2.2) and a standard cut-cell method (namely S-CCM), and their performances are compared. S-CCM is a conventional cut-cell method similar to the cut-cell reconstruction procedure as described

in Ji *et al.* [52]. All small cells are assigned to their largest neighbour fluid cells and those cells are combined into a single cell as in the proposed method, but the difference here is that there is no face decomposition on merged cells. Instead, the flow variables are stored at the true cut-cell centroid, which always lies inside the fluid region, and the fluxes of these variables are estimated at the midpoints of the faces bounding the cut-cell. The centroid of a cut-cell is computed as follows:

$$\mathbf{c}_m = \frac{\sum_{i=1}^{n_g} V_i \mathbf{c}_i}{\sum_{i=1}^{n_g} V_i} \tag{5.1}$$

where $\mathbf{c}_m$ are the coordinates of the centroid of the cut-cell; $\mathbf{c}_i$ and V_i are the coordinates of the centroid and the volume, respectively, of the i-th component cells comprising the cut-cell; and, n_g is the number of the component cells in the cut-cell. The results of these three test cases have been reported by the author in [79].

5.3.1 Inclined channel flow at high Reynolds number

The first test case is the turbulent flow through a plane channel that is inclined at β=0°, 10° and 30° with respect to the grid (Fig. 5.12(a)). A plane channel case with β=0°, where the wall boundary aligns exactly with the cell interface, is undertaken as a precursor to the 10° and 30° inclined channel flow cases in order to examine the performance of the current solver as well as the wall model on the coarse near-wall grids. As the immersed boundary aligns with the cell interface, the three methods that are evaluated here (GC-CCM, GC-IBM and S-CCM) collapse into a single wall-conforming case. The numerical parameters are chosen with reference to the work of Hoyas *et al.* [50] who investigated channel flow at the Reynolds number of $Re_\tau = 2000$[1] based on the channel half width h and the friction velocity u_τ. These values are adopted for the present study. The LES results using wall models at the equivalent Reynolds number are recently reported by a

[1]The respective values of the alternative Reynolds number based on the bulk velocity is found to be $Re_b = 46618$.

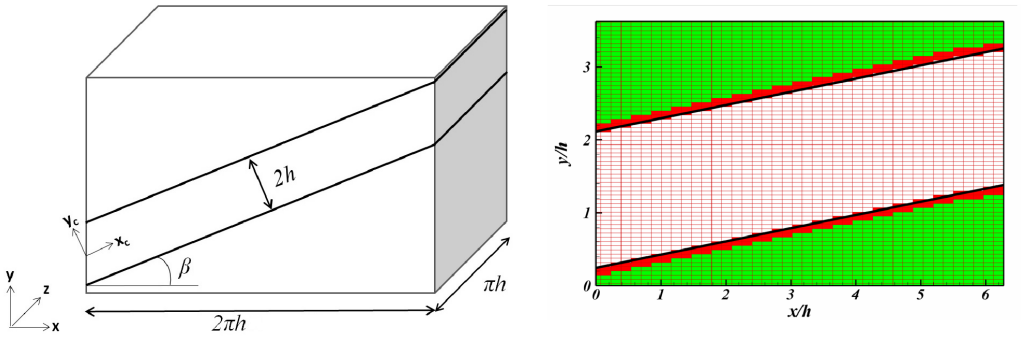

Figure 5.12: Computational set-up and the underline grids (*red cells*: ghost; *green cells*: solid; *line*: immersed interface) for the inclined turbulent channel flow. Every grid point is shown.

few others for the incompressible flows (*e.g.* [13, 94]). The periodic boundary conditions are employed in the streamwise and spanwise directions. To ensure that the global mass conservation is satisfied in the streamwise direction, the total mass flow rates going out (M_{out}) of, and coming in (M_{in}) to the domain are matched. To enforce the matching, all the outlet velocity components at the downstream interface are multiplied by the ratio M_{in}/M_{out} at every timestep. In the wall-normal direction, a simple wall model is used at both top and bottom interfaces. Having the plane channel with β=0° as a base reference case, the channel is then inclined at 10° and 30°, respectively, in order to test the reliability under a dramatic variation of wall distance y^+.

First, a channel size of $2\pi h \times 2h \times \pi h$ is immersed in a domain of $2\pi h \times 2.5h \times \pi h$ for β=0°. The mesh employs 40×40 cells in the streamwise ($x-$) and spanwise ($z-$) directions, respectively. In the $y-$ direction, wall-normal in this case, 40 cells (32 cells inside the fluid phase) are chosen such that the y^+ value corresponding to the first grid point away from the wall lies in the logarithmic layer ($y^+ > 30$). In all directions, the grid spacings (Δx, Δy and Δz) are uniform. Results for the mean velocity are compared with the DNS results of Hoyas *et al.* [50] in Fig. 5.13(a). Wall distances are non-dimensionalized based on the wall units ν/u_τ and the friction velocity u_τ from DNS of [50]. The first grid cell adjacent to the wall lies in the log-layer ($y^+ = 61$) as expected. The behaviour of the

mean velocity is slightly under-predicted near the wall, but beyond $y^+ > 400$ the solution from the current solver agrees well with the DNS profile for this wall-conforming case. The velocity fluctuation intensities are shown in Fig. 5.13(b). The peak values for u'^+ and w'^+ are surprisingly well captured while the same peak value for v'^+ is under-predicted near the wall. From the results presented here, it can be concluded that the current MILES solver in conjunction with a simple wall function yields reasonably good results for a turbulent channel flow.

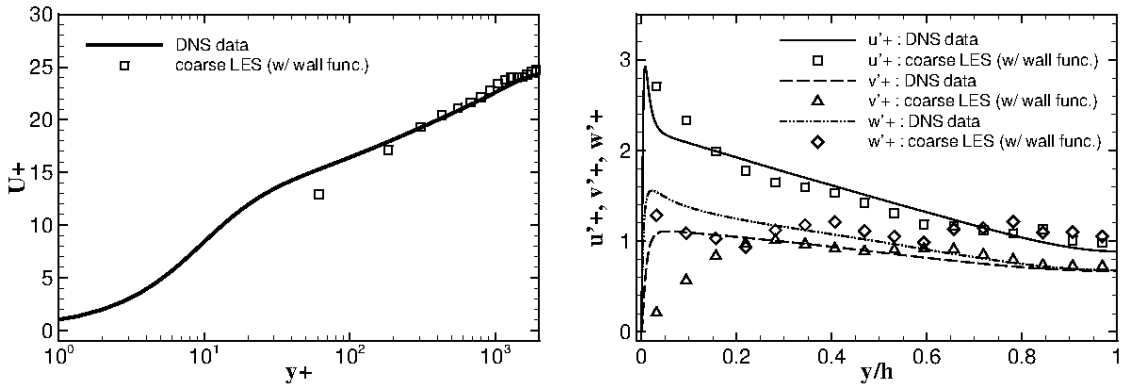

(a) Mean velocity profiles

(b) Velocity fluctuation intensities

Figure 5.13: Plane channel flow for $\beta = 0°$.

For the channel case where β=10°, the rectangular domain is changed to $2\pi h \times 3.625h \times \pi h$ in order to contain the inclined channel. The mesh employs 40 and 40 cells in the $x-$ and $z-$ directions, and 58 cells in the $y-$ direction such that the grid spacing remains unchanged from the plane channel case where β=0°. For β=30°, the rectangular domain is changed to $2\pi h \times 6.125h \times \pi h$ and the mesh employs 65 and 40 cells in the $x-$ and $z-$ directions, and 98 cells in the $y-$ direction. In both cases, the current methodology is tested severely due to the variation of the near-wall y^+ value along the streamwise direction. The streamwise distributions of the near-wall y^+ value are shown in Fig. 5.14(a). In the case of β=10°, the near-wall y^+ value fluctuates between local maximum and minimum values, whereas in the case of β=30°, the near-wall y^+ value gradually increases until its local maximum value (*i.e.* volume fraction of a merged-cell $\approx$ 1.5) is reached. The

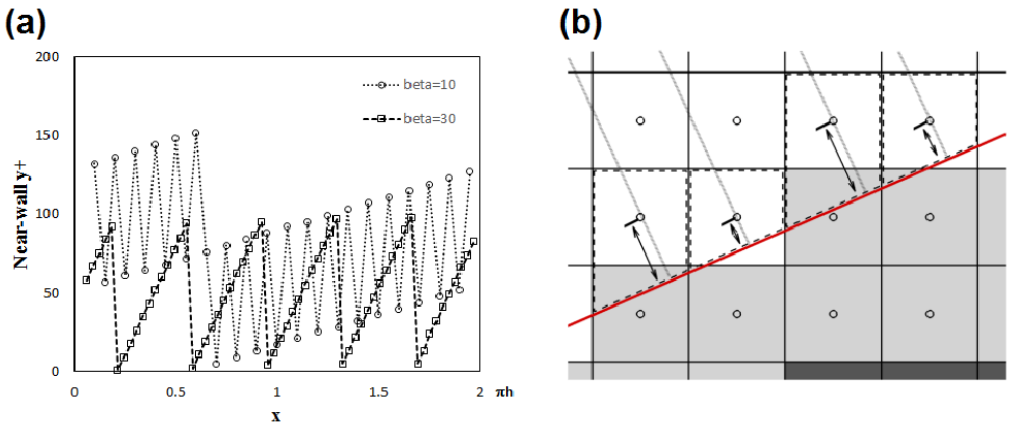

Figure 5.14: (a) Streamwise distribution of near-wall y^+ value for $\beta = 10°$ and $30°$, and (b) illustration of near-wall y^+ variation and wall-normal line.

resulting profiles for the mean velocity and velocity fluctuation intensities in the wall-normal direction from all three methods are shown in Figs. 5.15 and 5.16. The profiles at two different streamwise locations - one where a small near-wall y^+ value (in the viscous sub-layer region) is detected, and the other where a large near-wall y^+ value (in the log-law region) is detected - are presented. Since the wall-normal line does not always coincide with the computational nodes (Fig. 5.14(b)), the points in the profiles are computed from linear interpolation of the nearby nodes. At both inclination angles, the overall results confirm that the predicted mean velocity and velocity fluctuation intensity profiles from GC-CCM agree well with the DNS results with a similar accuracy as that for the β=0° case. The GC-IBM and the S-CCM, however, perform poorly to match with the DNS data. The wall functions in these methods under-predict the wall-shear stress, thereby severely under-predicting the mean velocity near the wall. This under-prediction is related to the over-predicted streamwise velocity fluctuation intensity (u'^+).

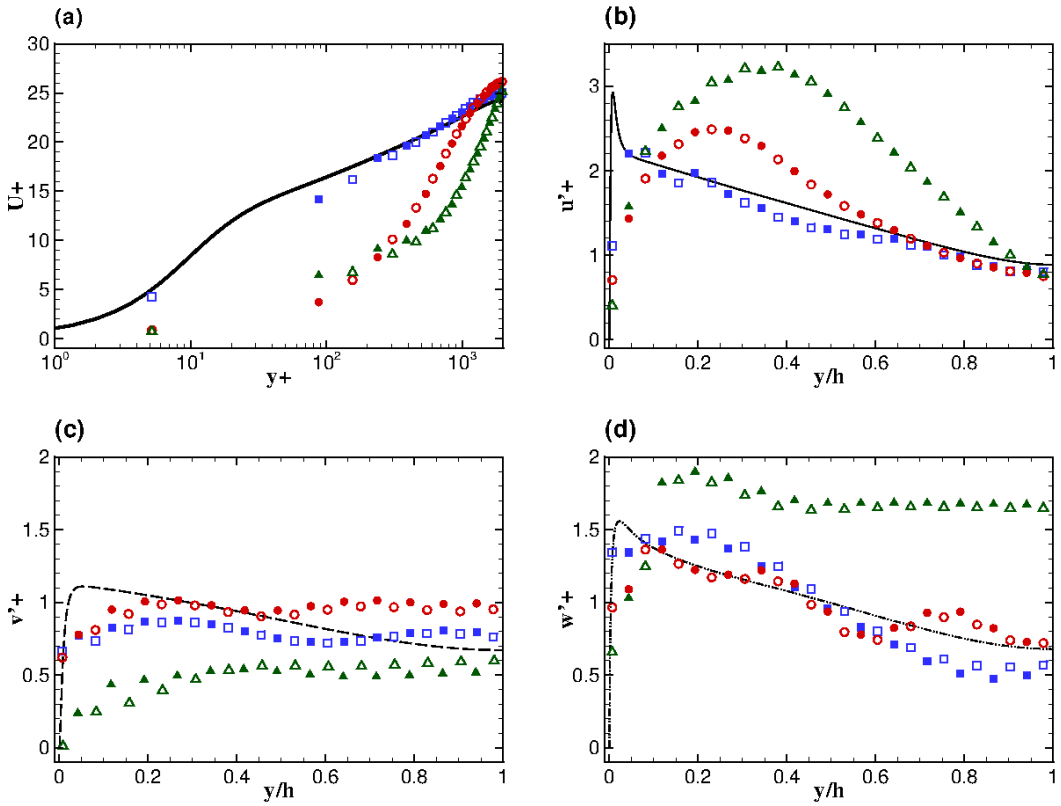

Figure 5.15: Plane channel flow for $\beta = 10°$; (a) Mean velocity profiles $U+$, (b) velocity fluctuation intensity u'^{+}, (c) velocity fluctuation intensity v'^{+}, and (d) velocity fluctuation intensity w'^{+}. *line* DNS; □ GC-CCM (small near-wall y^{+}); ■ GC-CCM (large near-wall y^{+}); ∘ GC-IBM (small near-wall y^{+}); • GC-IBM (large near-wall y^{+}); △ C-CCM (small near-wall y^{+}); ▲ C-CCM (large near-wall y^{+}).

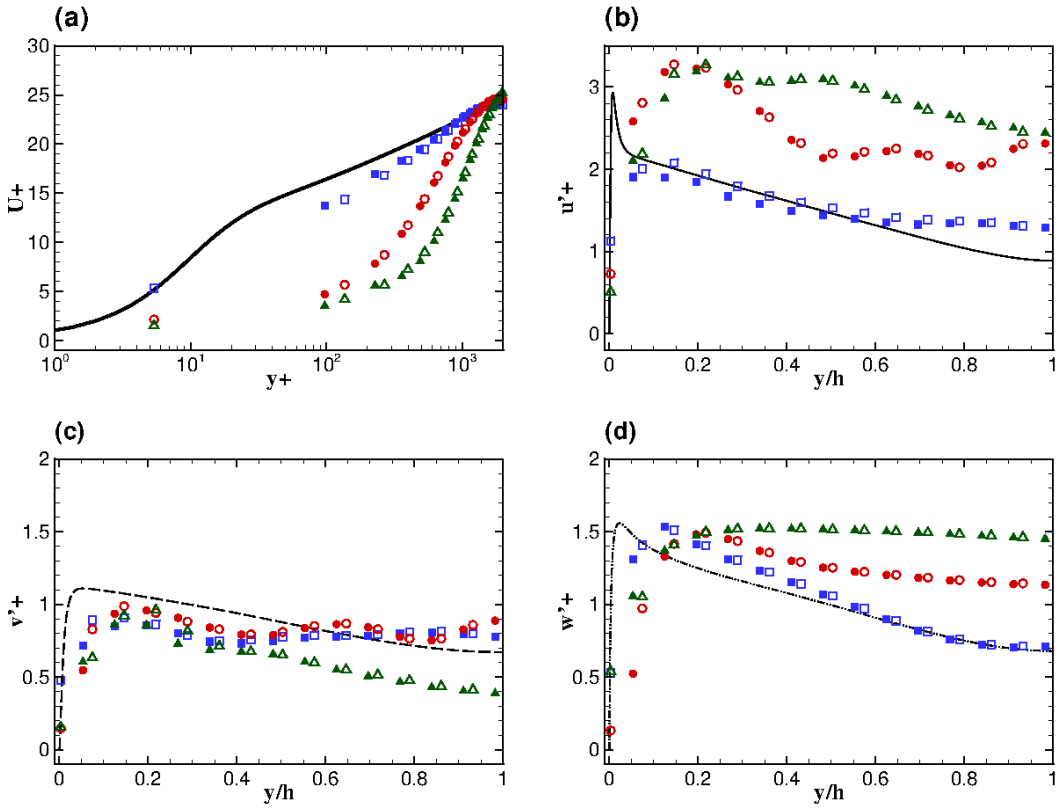

Figure 5.16: Plane channel flow for $\beta = 30°$; (a) Mean velocity profiles $U+$, (b) velocity fluctuation intensity u'^{+}, (c) velocity fluctuation intensity v'^{+}, and (d) velocity fluctuation intensity w'^{+}. *line* DNS; □ GC-CCM (small near-wall y^{+}); ■ GC-CCM (large near-wall y^{+}); ∘ GC-IBM (small near-wall y^{+}); • GC-IBM (large near-wall y^{+}); △ C-CCM (small near-wall y^{+}); ▲ C-CCM (large near-wall y^{+}).

5.3.2 Turbulent flow over a wavy Surface

The turbulent flow over a wavy boundary is an appropriate validation test case as the geometrical configuration is fairly simple, and yet, the flow pattern is complicated that it exhibits various flow structures at the convex and concave curvatures. Shortly after the wave crest, the flow speeds up to its maximum magnitude and then separates to form a recirculation zone at the downstream side of the wave. It then develops a turbulent shear layer over the recirculation zone. The flow-field can be categorized into several regions with unique characteristics and they are: the outer region, recirculation region, boundary layer region, shear layer region, separation region and reattachment region [10]. It is important to properly resolve the separated shear layer as this region plays an important role in the turbulent production. Typically, a flow structure in this test case requires careful grid resolutions with a grid clustering in the vertical direction to effectively resolve the boundary layer and the shear layer. An adequate streamwise resolution of the flow is also important particularly in the separation region due to the fact that the reattachment position (and so is the entire flow) is highly sensitive to the location of separation. The main difficulty in using DNS or LES for a complex wall-bounded flow at a high Reynolds number is the demand for a tremendous grid resolution. In general, it is crucial to have a fine mesh resolution in order to accurately predict these flow features. Most statistical turbulence models have difficulties in predicting these flow features or even the reattachment length. Using a body fitted mesh, several efforts have been directed to DNS (see [106] and literature cited therein) and to wall-resolved LES [127] for incompressible flows. For compressible flows, Sun *et al.* [106] reported their DNS results for turbulent flows over wavy wall geometries on a body fitted mesh using high-order convection and diffusion schemes. Obtaining an accurate representation of the detailed flow dynamics on a non-body conformal mesh is extremely challenging because the cells are cut at different angles in the regions where the most interesting phenomena such as separation and reattachment take place. Using the non-body conformal method, some have successfully performed LES of incompressible turbulent flow over a wavy surface using an IBM approach [112, 2]. The DNS study of higher Reynolds number ($Re = 11200$) flow over the wavy surfaces is also reported in Niceno and Kuhn [80]. For compressible flows, wall resolved LES results of turbulent flow over a wavy

surface at $Re = 6700$ using a GC-IBM approach are reported by the author in [78]. To the best of the author's knowledge, there has not been a reported work which incorporated a wall model in this type of simulations.

In this type of flow, the flow dynamics is strongly influenced by the small-scale eddies that are developing close to the wall. When the wall-shear stress is approximated by the wall model using the information from the outer flow, it can compensate the lack of resolution in near-wall region even with a relatively coarse near-wall mesh in the context of LES. The basic configurations in the test case are similar to that of a plane channel flow except that the bottom boundary wall mimics the transverse ripples given by $y_w = a\cos(\frac{2\pi x}{\lambda})$ where $a = 0.1$ is the amplitude of the wave and λ is the wavelength (Fig. 5.17). The average height of the channel h is such that $h = \lambda$ and the lower wall has two full sinusoidal waves. The size of the computational domain is $2h \times 1h \times 1h$ in the streamwise (x), vertical (y) and spanwise (z) directions, respectively. The Reynolds number based on the bulk velocity U_b and half channel height is 11200. Since the wall-function approach is used, coarse grids are employed where the flow domain is discretized by $180 \times 50 \times 40$ cells in the streamwise, vertical and spanwise direction, respectively. In all directions, the grid spacings (Δx, Δy and Δz) are maintained uniform. The comparison of the grid spacings from the current work and the grid spacings from the equivalent work by [80] in DNS is given in Table 5.3. The initial flow at a Mach number of 0.2 is given in the channel. The periodic boundary conditions are employed in the streamwise and spanwise directions, and wall models are used at the immersed interface and the top wall. To enforce the mass flow rate out of the computational domain equal to the mass flow rate into the computational domain, all the streamwise outlet velocity component at the downstream outlet plane is corrected by the ratio of inflow and outflow mass flow rates, similar to the technique used in the turbulent channel flow test case.

The large-eddy simulations are performed using three different non-body conformal formulations as before: the proposed cut-cell method (GC-CCM), ghost cell based immersed boundary method (GC-IBM), and standard cut-cell method (S-CCM). Fig. 5.18 shows the isolines of the mean streamwise velocity obtained from each method. All quantities are normalized with the bulk velocity U_b and averaging of flow variables is carried out over

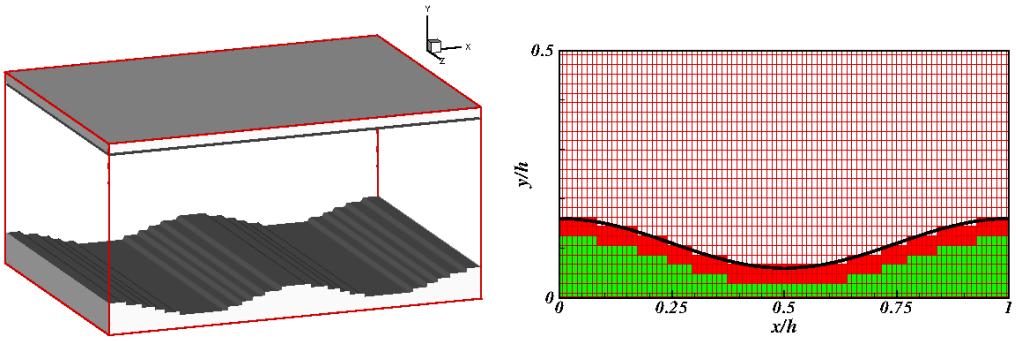

Figure 5.17: The computational domain and the underline grids (*red cells*: ghost; *green cells*: solid; *line*: immersed interface) for the flow over a wavy boundary. Every grid point is shown.

Table 5.3: The best approximations of locations of separation and reattachment points (x/λ) from the preceding wave crest.

Case	Δx	Δy	Δz	Separation point	Reattachment point
Current cut-cell method	$h/45$	$h/25$	$h/20$	0.23	0.60
Standard GC-IBM	$h/45$	$h/25$	$h/20$	0.17	0.77
Standard cut-cell	$h/45$	$h/25$	$h/20$	0.23	0.77
DNS [80]	$h/128$	$h/256$	$h/128$	n/a	n/a

the spanwise direction and in time. A qualitative observation reveals that the dominant flow structures are reasonably well captured with GC-CCM. The strong velocity gradients on the hill (between $0.6 < x/h < 1.0$) and the recirculation area reported in Niceno and Kuhn [80] can be seen in Fig. 5.18(a). This recirculation area, characterized by large oscillations in the mean velocity, appears to be excessively large when GC-IBM and S-CCM are adopted. The strong velocity gradients on the hill before and after the recirculating zone are also not visible with these two methods. The locations of the predicted mean separation and reattachment points are best approximated and given in Table 5.3. Although it is not possible to measure these locations precisely from this non-body conformal coarse mesh, it is evident that GC-IBM predicts an early flow separation and also a much delayed flow reattachment point compared to the current method. The numerical results of mean streamwise profiles are plotted against the DNS results [80] in Fig. 5.19(a). The profiles at the five probing stations in a wavelength of the topography ($x/h = 0.00, 0.25, 0.50, 0.75$ and 1.00) are selected and plotted for evaluations. $x/h = 0.00$ and $x/h = 1.00$ are at the wave crests, $x/h = 0.50$ is at the wave trough, and $x/h = 0.25$ and $x/h = 0.75$ are at the inflection points of the wall profile. Streamwise vortices are a dominant turbulent structure near the wavy wall. The results confirm that the mean streamwise velocity profile obtained from GC-CCM agrees well with that from DNS despite the coarse grid employed. It can be deduced from the good agreement of the mean streamwise velocity profiles that the predicted separation and reattachment points also agree reasonably well with the DNS results (which are not quantified in Niceno and Kuhn [80]). Using GC-IBM and S-CCM in conjunction with wall functions, the resulting coarse grid LES solutions under-predict the mean velocity near the wall, similar to what has been observed in the inclined turbulent channel flow. The vertical velocity profiles (Fig. 5.19(b)) obtained with GC-CCM also show a reasonably good agreement with the DNS results except at the location $x/h = 0.50$ where large discrepancies are observed. With the employment of wall functions, obtaining a precise match of the velocity profiles at $x/h = 0.50$ with LES is nearly impossible since the law-of-the-wall does not hold anymore in this recirculation region. The coarse grid LES with a wall model from GC-IBM and S-CCM heavily under-predicted the vertical velocity at all probing stations, demonstrating the poor performance caused not only by the wall

functions but also by their immersed boundary and cut-cell techniques. Fig. 5.19(c) and 5.19(d) show the comparisons of the streamwise and vertical normal stresses from all three methods. All three methods predict marginally when compared against DNS results with GC-IBM showing particularly poor results for the streamwise normal stresses. Generally, all the predictions at $x/h = 0.50$ exhibit the largest discrepancy from the DNS.

5.3.3 Supersonic flow over a circular cylinder

Lastly, a supersonic flow past a circular cylinder at $Re_D = 2 \times 10^5$ and $M_\infty = 1.7$ is presented in order to demonstrate the robustness of the proposed formulation for higher Mach number flows. With D being the diameter of the circular cylinder, the simulations have been performed in the domain of $[-10D, 10D] \times [-8D, 8D] \times [0, 3D]$ in the x (streamwise), y (cross-streamwise) and z (spanwise) direction respectively. The cylinder is centred at the origin. At the inflow, all velocity components and density are imposed, and pressure is calculated from the equation of state. At the outflow and the lateral boundaries, non-reflecting outflow conditions based on wave decomposition are used. In the spanwise direction a periodic boundary condition is employed. These boundary treatments are explained in the Sec. 3.4.2. The flow domain is discretized by $400 \times 200 \times 40$ cells in the streamwise, cross-streamwise and spanwise directions respectively. In the streamwise and cross-streamwise directions the grid is stretched to cluster points near the surface of the cylinder in order to provide a higher resolution in the vicinity of the cylinder (Fig. 5.20). Δx and Δy in the vicinity of the circular cylinder are $0.02D$.

The LES is conducted using the three different non-body conformal formulations again. Fig. 5.21 provides a Mach number contours from GC-CCM. A bow shock is formed ahead of the cylinder across which the on-coming supersonic becomes subsonic. This subsonic flow travels along the cylinder surface and accelerates to form a supersonic region. The supersonic region is separated from the subsonic recirculation region that is contained inside the long symmetric tail shock starting from directly behind the cylinder. Fig. 5.22 provides a local view of the Mach number contours around the cylinder from each of the three methods. A qualitative observation of these contours reveals that the three methods

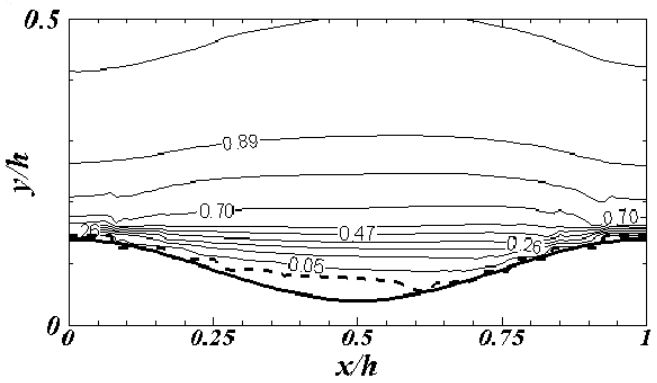

(a) GC-CCM

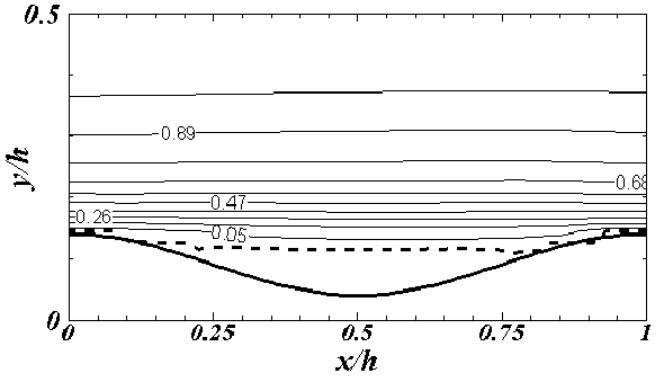

(b) GC-IBM

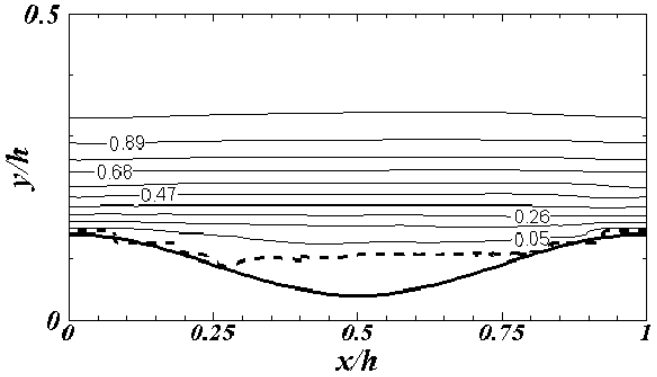

(c) S-CCM

Figure 5.18: Contours of mean streamwise velocity normalized by bulk velocity U_b. (*dotted line*: zero mean velocity)

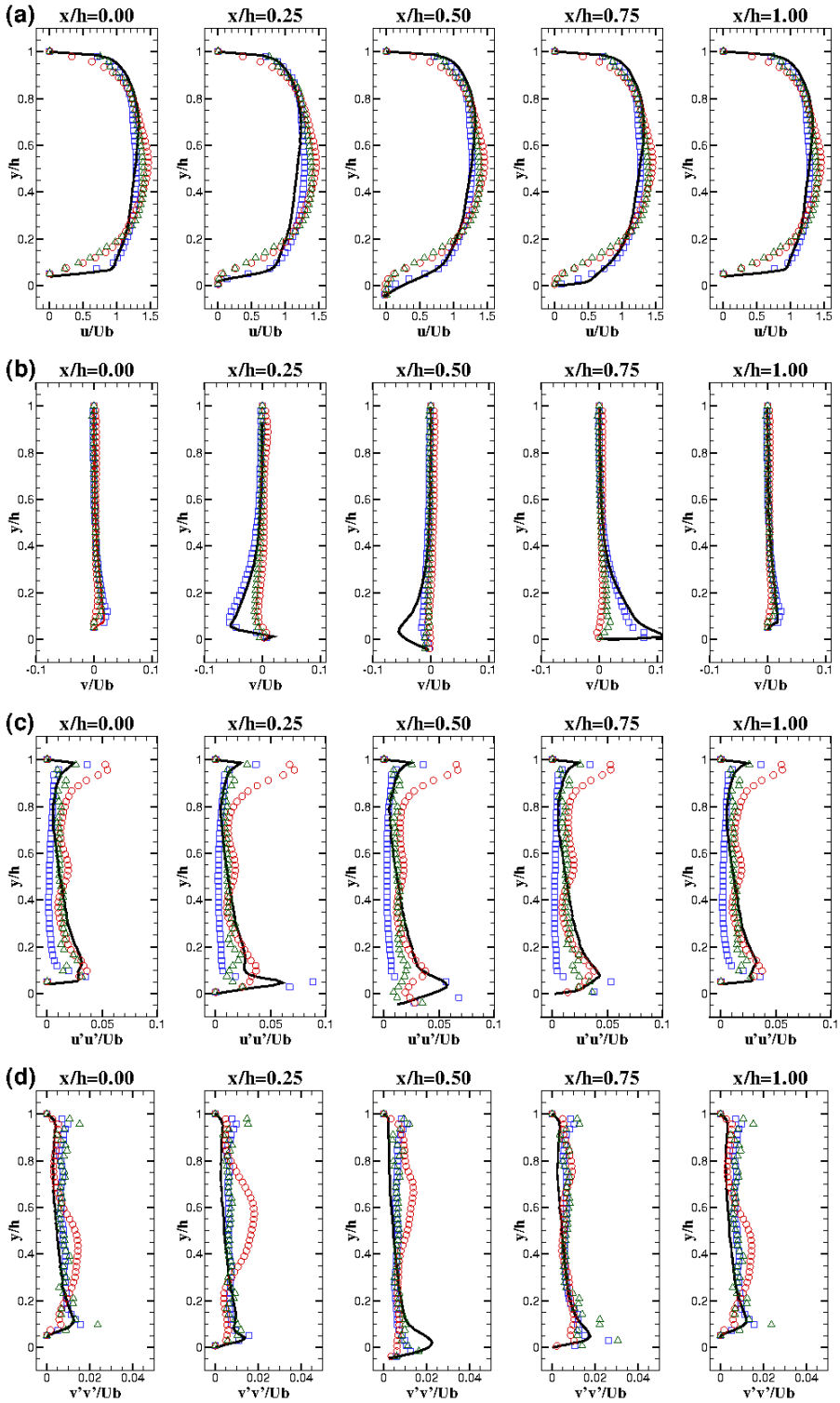

Figure 5.19: Profiles of (a) mean streamwise velocity, (b) mean vertical velocity, (c) streamwise normal stress, and (d) vertical normal stress at different streamwise locations (□: GC-CCM, ∘: GC-IBM, △: C-CCM, −: DNS [80]).

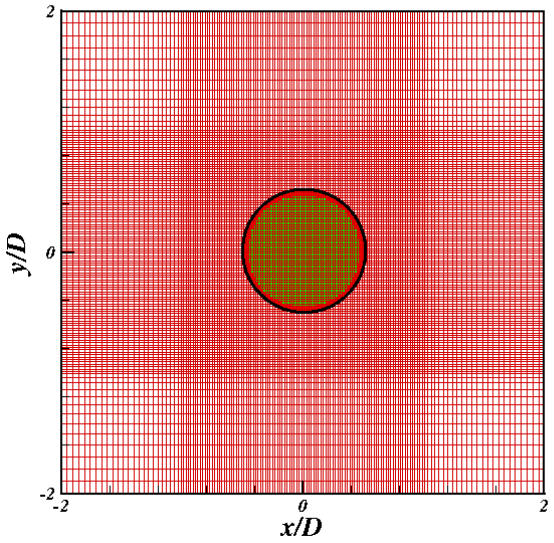

Figure 5.20: Local view of the grid (*red cells*: ghost; *green cells*: solid; *line*: immersed interface) for the supersonic turbulent flow past a cylinder. Every grid point is shown.

provide virtually indistinguishable results. The results of computations are summarized and compared with the corresponding experimental data [4] and the RANS results [83] in Table 6.1. The separation point is given in θ which denotes the clockwise angle measured from the leading edge of the cylinder. The y^+ value corresponds to the first grid point away from the cylinder surface and it varies across the cylinder surface in the given range. Behind the cylinder where flow has separated, y^+ values are extremely small because the friction velocity is extremely small. The drag coefficient is computed according to the expression: $C_D = F_D/(\frac{1}{2}\rho_\infty {U_\infty}^2 A)$ where F_D is the drag forces and $A = D \cdot l_{spanwise}$. The time-averaged surface pressure coefficient distributions along the surface of the cylinder are provided in Fig. 5.23 along with the experimental data of [4]. All three methods show a good agreement with the experimental data despite the coarse grids used in the simulations.

Overall, the differences in the results between the three methods are minimum in this high Mach number and turbulent test case. The main reason is, the previous test-cases showed evident differences in the velocity profiles and the turbulence quantities, but such

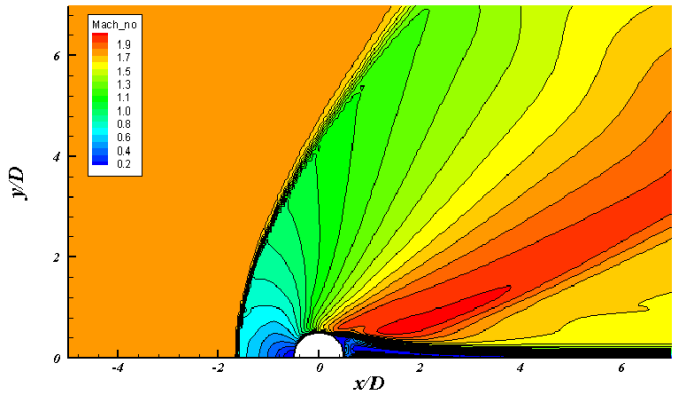

Figure 5.21: Close up view of the Mach contour maps for the supersonic turbulent flow past a cylinder for $Re_D = 2 \times 10^5$, $M_\infty = 1.7$ (GC-CCM only).

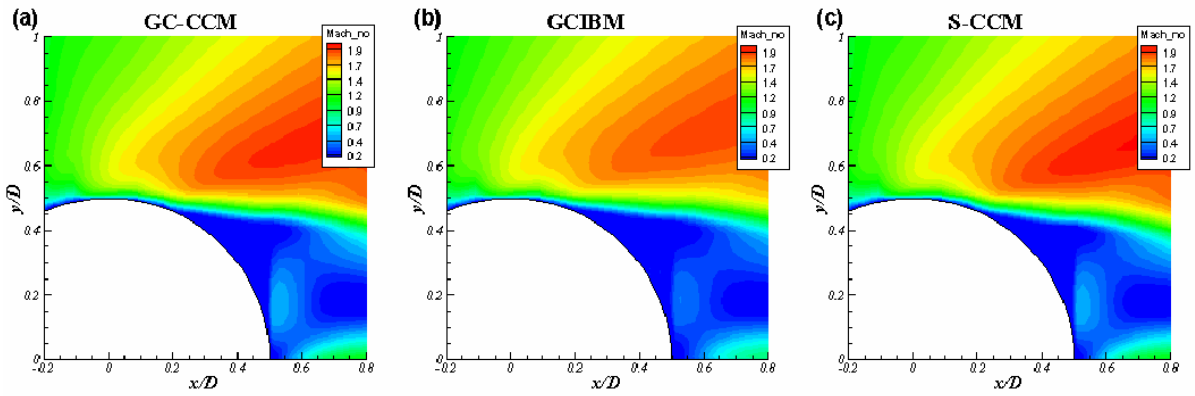

Figure 5.22: Local view of the Mach number contour for the supersonic turbulent flow past a cylinder for $Re_D = 2 \times 10^5$, $M_\infty = 1.7$.

Table 5.4: Simulation of supersonic turbulent flow over a circular cylinder. The separation point θ_s, the drag coefficient C_D, and the average y^+ are compared against the experimental data of [4].

Case	y^+ range	Separation point θ_s	C_D
GC-CCM	0.4 to 98	116°	1.39
GC-IBM	0.5 to 95	116°	1.26
S-CCM	0.3 to 98	117°	1.40
Experimental [4]	n/a	112°	1.43
RANS-IBM (fine) [83]	n/a	111°	1.39

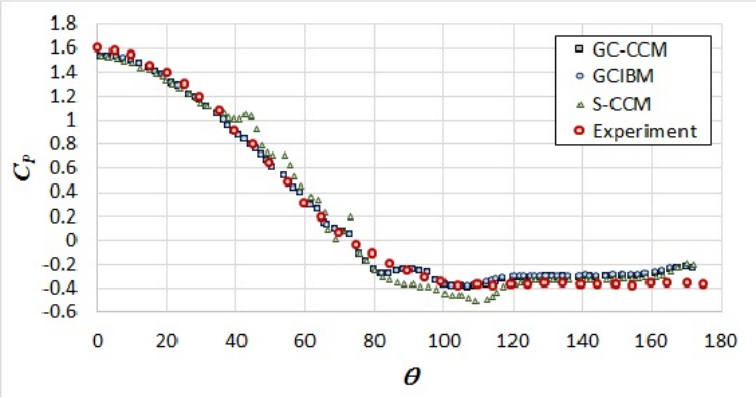

Figure 5.23: Distribution of pressure coefficient along the surface of the cylinder for $Re_D = 2 \times 10^5$, $M_\infty = 1.7$.

sensitive quantities are typically not available in this test-case at a high Mach number. An accurate prediction of the friction drag requires an accurate prediction of wall shear-stress, and it was seen in the previous test-cases that the prediction of wall shear-stress varies with the non-body conformal method used. This, however, is not important for the cylinder at this high Mach number, as the main contribution to the aerodynamic drag is the pressure drag with the frictional drag contributing less than 0.5% [4].

5.4 Conclusions

For flows involving low to moderate Reynolds numbers, the ghost-cell immersed boundary method (GC-IBM) of Tseng and Ferziger [112] is extended in order to perform LES of compressible flows. Despite the use of the standard Smagorinsky turbulence model (in conjunction with the van Driest damping function), the results agree reasonably well with the DNS data. The finer mesh results are consistent with the results reported in the literature while the coarse mesh results fail to correctly predict the recirculation zone. The GC-IBM is successfully applied to perform LES of compressible turbulent flow associated with wavy wall geometries. To demonstrate the robustness of the current method for higher Mach number flows, it is tested with a supersonic flow over a cylinder at a moderate Reynolds number. The GC-IBM nicely captures the qualitative behaviour of the supersonic flow in the vicinity of the cylinder. This result demonstrates the validity and flexibility of the GC-IBM algorithm in the compressible LES framework.

For the flows involving high Reynolds numbers, this work develops the ghost-cell based cut-cell method (GC-CCM), which is built upon the conservative Cartesian cut-cell method of Meyer *et al.* [74] and the GC-IBM of Tseng and Ferziger [112]. For merged cells, cell faces are decomposed, and additional fluxes based on adjacent cells are calculated in order to accurately capture the near-wall flow behaviour. The proposed method is assessed on grids with coarse near-wall resolution and applied to perform LES of high Reynolds number flows in conjunction with a wall model. A simple wall function approach is used to approximate the wall-shear stress, and the discretization error is used to model the sub-grid scale turbulence (MILES), although both of these models can be replaced by others

if desired. The results confirm that the proposed method agrees well with the reference data despite the coarse near-wall resolution. The method represents the flow physics in the vicinity of the solid boundary more accurately than the other non-body conformal methods compared in this work. It can be concluded that the proposed GC-CCM, with the combination of a wall model, is a viable approach that renders relatively accurate results for compressible flows at high Reynolds numbers.

Chapter 6

Computational Aeroacoustics

6.1 Introduction

6.1.1 Motivation and objectives

The sound generated by fluid flow (aeroacoustic noise) originates from many sources, including jet flow, spinning blades, wind, and flow around bodies of various geometrical shape. A good understanding of sound generating mechanism and the ability to predict that sound accurately and reliably is a necessary step in reducing or controlling the noise. In this chapter, far-field radiated noise prediction from flow over a circular cylinder is studied as a benchmark case. A promising strategy is to develop a hybrid approach which combines a flow solver for computing the sound source field with an acoustic solver for the acoustic far-field. For the flow solver, the large-eddy simulation (LES) methodology, with the non-body conformal method developed in the earlier chapter, is employed to accurately represent the flow generating mechanism. The flexibility of the non-body conformal method in handling the complex geometries can easily extend the geometry of cylinder into wings, high-lift systems or landing gears. The acoustic solver can be any of the extended Kirchhoff method, acoustic analogies or the linearized Euler equations (LEE). In this chapter, the methodologies considered in this work for the acoustic calculation is described and

a numerical result from a benchmark case is reported.

6.1.2 Hybrid approach in computational aeroacoustics

The full, time-dependent and compressible Navier-Stokes equations, which describe the motion of fluids, also describe the propagation of acoustic waves, as these waves propagate by means of adiabatic compression and decompression of fluid. The numerical computation of these sound sources and sound propagation constitutes the main focus in the field of *Computational Aeroacoustics* (CAA).

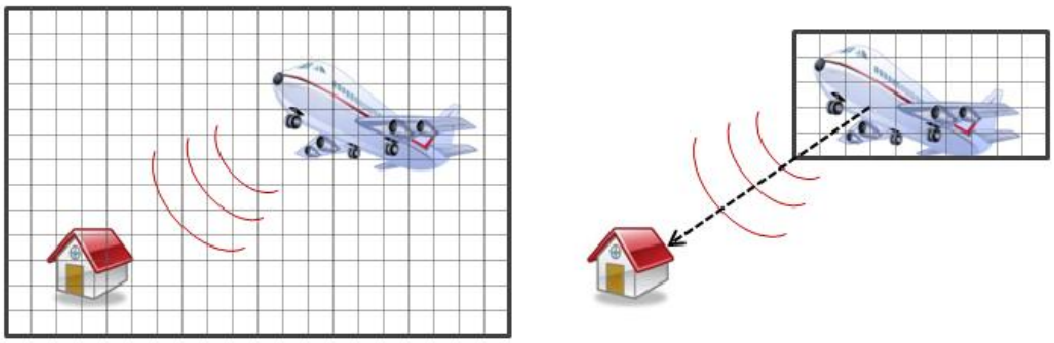

(a) Direct Approach (b) Hybrid Approach

Figure 6.1: Numerical approaches for far-field aeroacoustics problems. The grids illustrate the computational domain.

For a far-field noise prediction, the intuitive numerical approach is to extend the computational domain from the noise source to the receiver region, and solve the full Navier-Stokes equations using modern turbulence simulation techniques such as DNS or LES. This approach is called a *direct approach* (Fig. 6.1(a)). Unfortunately, this approach poses limitations and challenges when the goal is to perform a far-field noise prediction. For instance, a CFD calculation, where the domain extends from an airplane (noise source) in the air to a house on the ground (receiver), requires a prohibitive computer storage that it is bordering on the absurd. The difficulties arise from the fact that the nature of the

aeroacoustics problem is substantially different from those of traditional fluid dynamics problems. Some of the difficulties are:

1. Amplitude Disparity - Acoustic wave involves extremely small pressure fluctuations, but the noise source region involves pressure changes that are several orders of magnitude higher. While dealing with such high pressure changes, the propagation of acoustic waves must be handled simultaneously. This requires a numerical scheme to have an extremely high order of accuracy to minimize the numerical dispersion and dissipation. With a conventional level of accuracy, it is almost certain that the numerical error will overtake the magnitudes of acoustic waves.

2. Spatial Disparity - Acoustic far-field is typically several orders of magnitude larger in length than the noise generating flow field of interest. The allowable grid size for calculating the acoustic waves can be much coarser (than the grid size required for the CFD flow field), however, to compute the solution accurately over such long propagation distances, a uniform grid should be taken in the entire domain in order to reduce the truncation error. This enforces the grid size to match that for the CFD flow field throughout the entire domain. This can be extremely costly.

As an alternative, *hybrid approaches* (Fig. 6.1(b)) became popular for far-field aeroacoustic predictions. In this approach, the computation of flow decouples from the propagation of sound. The computation of noise source is first obtained using a conventional CFD technique. The propagation of sound is then computed in a separate acoustic solver with the source field data as an input. Of many acoustic solvers in the hybrid approaches, the most common ones are the extended Kirchhoff approach, the Ffowcs-Williams and Hawkings (FW-H) approach, and the Linearized Euler Equations (LEE) approach. LEE is the most rigorous but also the most computationally expensive method, as it has to solve a group of linearized equations on a continuous computational mesh that covers the whole acoustic field of interest. The biggest advantage is that it accounts for non-uniform mean flow and treats the convection and rarefaction effects that have an important influence on the propagation of acoustic waves. When the flow conditions outside the source zone are

assumed such that it is quiescent and homogeneous, a simple integral approach such as the Kirchhoff approach or the Ffowcs-Williams and Hawkings approach would suffice. These approaches solve only scalar equations at discrete locations in directions corresponding to the observer positions, therefore, they are very efficient computationally. Of the two integral approaches, the more popular method is the Ffowcs-Williams and Hawkings (FW-H) method which is based on the Lighthill's Acoustic Analogy. Several papers [7, 101] have reported the superiority of the FW-H approach over the Kirchhoff approach. In the following section, the derivation of Lighthill's acoustic analogy, FW-H equations, and their integral formulations are briefly explored from the fundamental equations. The assumptions along the derivation process will be emphasized, and the limitations in their usage will be discussed.

6.2 Acoustic analogy

6.2.1 Lighthill's acoustic analogy

Aeroacoustics became an important issue in the 1950s with the development of commercial jet powered aircrafts. The need to reduce the noise from jet engines puts a focus on the lack of understanding of the underling mechanisms. This stimulated James Lighthill [65] to develop his theory for aeroacoustic sound generation where he proposed how to obtain this source term from within the Navier-Stokes equations. This is the foundation for a field of research, Aeroacoustics. In classical acoustics, the mass and momentum equations are first reduced to the Euler equations after assuming that there is no dissipation and no heat conduction (adiabatic process). This can lead to the assumption of constant entropy (isentropic flow) throughout the entire flow field. Also, sound perturbations are so small that their contribution to the convection velocity of the flow is negligible in many cases. This means that sound can, in essence, be described by the linearized Euler equations. Further assuming that the fluid is homogeneous and quiescent, a homogeneous wave equation can be derived. The derivations are readily available in textbooks on fundamental acoustics. With the classical acoustic wave equations, the limitation is the lack of models for sound

generation, *i.e.* there is no source term present in the wave equation. The acoustic field is generated in a quiescent fluid by an imposed external force $f(t)$, and assumes this external force induces linear perturbations of the quiescent fluid state. Evidently, sound generation from within the fluid itself - by turbulent and/or unsteady vortical flow processes that are described in the Navier-Stokes equations - cannot be treated unless it is somehow obtained by other means which is incorporated as an external force.

The idea of Lighthill's acoustic analogy is to reformulate the mass and momentum equations in a form of wave equation, but without introducing the above assumptions or simplifications. The result is an inhomogeneous wave equation whose source term contains all the nonlinearities, viscous stress and entropy gradients (that are neglected in the derivation of the classical wave equations). In his theory, sound is generated by unsteady flows through the nonlinear interaction of velocity fluctuations, entropy fluctuations, as well as viscous stress. In the free space, in the case of jet noise in particular, this is true. The theory is based on the underlying assumption that the space is split into two parts: the source field and the sound field (see Fig. 6.2). In the source field, the nonlinearities, viscous stress and entropy gradients take place to generate the noise. In the sound field, the generated noise propagates into the homogeneous and quiescent fluid. This is the part where the fluctuating pressure (or density) field satisfies the homogeneous wave equation.

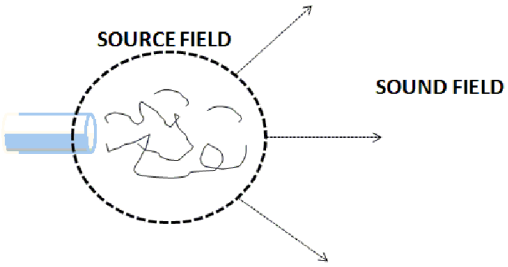

Figure 6.2: Two fields in Lighthill's acoustic analogy: Source Field and Sound Field.

A brief derivation of Lighthill's acoustic analogy is explained below. Similar to the derivation of the classical wave equation, the starting point is the exact form of mass and momentum equations (*i.e.* Eq. 2.1 and Eq. 2.2):

$$\frac{\partial \rho}{\partial t} + \frac{\partial \rho u_i}{\partial x_i} = 0 \tag{6.1}$$

$$\frac{\partial \rho u_i}{\partial t} + \frac{\partial \rho u_i u_j}{\partial x_j} + \frac{\partial p}{\partial x_i} - \frac{\partial \tau_{ij}}{\partial x_j} = 0 \tag{6.2}$$

Subtract $\frac{\partial}{\partial x_i}$ of momentum equation from $\frac{\partial}{\partial t}$ of continuity equation:

$$\frac{\partial^2 \rho}{\partial t^2} = \frac{\partial^2}{\partial x_i \partial x_j}(\rho u_i u_j + p\delta_{ij} - \tau_{ij}) \tag{6.3}$$

Assuming that the source region is embedded in a surrounding homogeneous fluid with no mean flow (characterized by the mean pressure p_0, mean density ρ_0 and mean sound speed c_0), it then follows a similar procedure as in the derivation of the classical wave equation. Substituting $\rho = \rho_0 + \rho'$ and $p = p_0 + p'$, and subtracting $c_0^2 \nabla^2 \rho'$ to obtain an inhomogeneous wave equation:

$$\begin{aligned} \frac{\partial^2 \rho'}{\partial t^2} - c_0^2 \frac{\partial^2 \rho'}{\partial x_i \partial x_i} &= \frac{\partial^2}{\partial x_i \partial x_j}(\rho u_i u_j + (p' - c_0^2 \rho')\delta_{ij} - \tau_{ij}) \\ &= \frac{\partial^2 T_{ij}}{\partial x_i \partial x_j} \end{aligned} \tag{6.4}$$

The left-hand side of the equation represents the acoustic-field while the right-hand side represents the source-field. T_{ij} is called the Lighthill stress tensor, which takes care of the sound generating fluid motion. It is a departure of a linear wave motion through a quiescent fluid. Lighthill stated that this acoustic source is a quadrupole source. The Lighthill stress tensor $T_{ij} = \rho u_i u_j + (p' - c_0^2 \rho')\delta_{ij} - \tau_{ij}$ contains three identifiable terms:

- $\rho u_i u_j$ is the Reynolds stress. In isentropic turbulent flows, this is the only significant term.
- $(p' - c_0^2 \rho')\delta_{ij}$ represents the deviations from adiabatic changes of state that occur

when, for instance, there is heat release from chemical reactions (combustions). For isentropic flow, this term is zero.

- τ_{ij} is the viscous stress. This term is associated with viscous dissipation of motion and is usually negligible.

This is an analogy because it represents the full complex fluid motion as a linear wave equation for a quiescent fluid, plus a source term which is from the unsteady turbulent flow. In other words, it assumes that the source field and the acoustic field are independent (uncoupled). This is the main limitation of this theory, which is further discussed in the next section.

6.2.2 Limitations in Lighthill's theory

In Lighthill's theory, it is assumed that the source term is known and unaffected by the acoustic field. This is called a one-way coupling of the flow and sound (Fig. 6.3(a)). This is a good approximation when the splitting of space in two parts, the sound field and the source field, is valid. For this to be valid, sound must be produced in a free space with no acoustic reflections which can influence the sound generation. Sound perturbations also must be so small that their contribution (while propagating) to the convection velocity of the flow is negligible. The latter is the same underlying assumption that is applied in the classical acoustics, however, in the application of aeroacoustics this sometimes fails. In some situations where acoustic waves are reflected back to the source region, a modulation of the source process is possible which can lead to a positive (unstable) feedback loop. This phenomenon, referred to as a self-sustained oscillator, results in the creation of distinct tones, "whistling". This is not accounted for in the Lighthill's theory. In some engineering practice, knowledge about whistles is important as they can produce high sound levels. Cavity noise belongs to this case where the practical example includes such as sunroof buffeting. Another limitation is the assumption that the fluid motion and mean flow gradients do not affect the sound generation and propagation (which is also assumed in the classical acoustics) (Fig. 6.3(b)). The theory is derived for the case where sources are

embedded in a quiescent flow (zero mean flow velocity U_0 and constant fluid state p_0, ρ_0 and c_0). In reality, this may not be true. A strong mean flow can lead to curved propagation paths and to a frequency change, called Doppler shift, in the emitted sound. In this case, an acoustic solver based on Linearized Euler Equation (LEE) is useful.

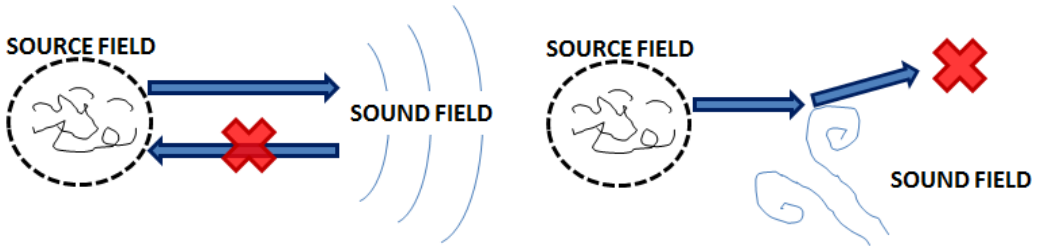

(a) One-way coupling (b) No mean flow gradients

Figure 6.3: Limitations in Lighthill's theory.

6.3 Curle's equation

In the derivation of Lighthill's acoustic analogy, a turbulent flow is assumed to be the quadrupole source only, which is driven by the unsteady flow in free space. The contribution to the sound field from this quadrupole source is generally small and negligible at low Mach numbers [65]. In most practical applications turbulence is generated by the presence of solid body in the flow. It is not hard to find examples of noisy flows that involve aerodynamic forces interacting with solid objects. Airframe noise is an important component of overall noise during an aircraft landing. In the automotive industry, wind noise is also an important area since flow past components, such as side-view mirrors, A-pillars or windshield wipers, can be noisy. Other examples include the noise from wind turbines, fans in rotating machines, and helicopter rotors. The presence of a solid object in the flow enhances noise radiation in two ways: 1) by creating noisy flow features such as unsteady separation and vortex shedding, and 2) by imposing a boundary inhomogeneity that promotes efficient conversion of flow energy to acoustic energy.

It is possible to include the effect of a solid object within the acoustic analogy through the use of mathematical control surfaces. Curle [20] extended the Lighthill's analogy to include the effects of solid boundaries. Consider a volume of fluid V outside a closed control surface S (see Fig. 6.4). The function f is defined such that $f < 0$ is the volume interior to the solid surface, and $f > 0$ is the volume exterior to the surface. Bypassing the mathematical rigours, the integral solution can be written as [39]:

$$\rho(x,t) = \frac{1}{c_0^2}\int\int_V T_{ij}\frac{\partial^2 G}{\partial y_i \partial y_i}\,\mathrm{d}^3 y\,\mathrm{d}\tau - \frac{1}{c_0^2}\int\int_S n_j p_{ij}\frac{\partial G}{\partial y_i}\,\mathrm{d}^2 y\,\mathrm{d}\tau \tag{6.5}$$

where G is the Green's function and n_j are components of the outward pointing (into the fluid) unit normal of the surface S. The derivation is well documented in Curle's original paper [20]. If the solid body is small relative to the acoustic wavelength, the effect of the body on sound propagation is negligible, and Curle's surface integral predicts a compact dipole which, at low Mach numbers, dominates the quadrupole radiation. For this acoustically compact case, the free-space Green's function can be used and the above equation becomes Curle's solution to the Lighthill equation. The integral solution takes the following form in the acoustic far field:

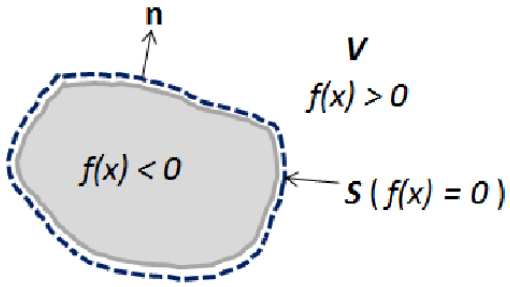

Figure 6.4: The definition of the solid surface as $f(x) = 0$. The surface integral is taken over the surface S of the body and the volume integral over the part of space V where Lighthill's quadrupole term gives a contribution.

$$\rho(x,t) \approx \frac{1}{4\pi c_0^3}\int_S \frac{r_i}{r^2}\frac{\partial}{\partial t} n_j p_{ij}(y, t-\frac{r}{c_0})\,\mathrm{d}^2 y + \frac{1}{4\pi c_0^3}\int_V \frac{r_i r_j}{r^3}\frac{\partial^2}{\partial t^2} T_{ij}(y, t-\frac{r}{c_0})\,\mathrm{d}^3 y \tag{6.6}$$

where $r = |x - y|$ is the distance between an observer's position x and a source position y, and $r_i = x_i - y_i$.

If the solid object is not acoustically compact, its presence is felt by the acoustic waves, resulting in a more complex scattering field. To account for the surface reflection of acoustic waves, the correct hard-wall boundary condition must be satisfied by the acoustic components of the flow. This can be achieved in two ways. If the source field is obtained from a compressible flow calculation (with a high-order accurate scheme), the appropriate acoustic boundary condition is naturally satisfied. Curle's solution is then valid even though it utilizes the free-space Green's function. If, on the other hand, the source field is from a less expensive incompressible flow calculation (or compressible flow calculation with a low-order scheme), acoustic boundary conditions need to be imposed when solving Eq. 6.5 which necessitates the use of Green's function tailored to the specific geometry in consideration. Analytical Green's functions for hard-wall boundaries are unavailable except for the simplest geometries. For complex geometries, the exact Green's functions can be computed using a *boundary element method* - a numerical method that is actively used in many engineering applications for acoustics.

6.4 Ffowcs-Williams and Hawkings equation for moving bodies

Curle showed that the effect of a rigid body can be incorporated in Lighthill's acoustic analogy as an additional source term. This approach has been generalized by Ffowcs-Williams and Hawkings who derived a very general formulation valid for any moving body

enclosed by a surface $S(t)$. This is achieved by an elegant and efficient utilization of generalized functions (see Section C.2.8 Surface Distributions in [91]). Although originally meant to include the noise generation by moving bodies (such as propeller noise) into the Lighthill's theory, it is now the most widely used starting point for theories of flow induced noise.

The original paper [31] that presents the FW-H equation was difficult to understand, as considerable mathematical maturity was required to follow the author's reasoning in the derivation. Taking advantage of their hard work, the final equation in a differential form is considered and presented here. Consider again a closed, non-deformable surface defined by $f(x,t) = 0$, moving along a velocity vector v (see Fig. 6.5). FW-H equation can be written as follows:

$$(\frac{1}{c^2})\frac{\partial^2 p'}{\partial t^2} - \nabla^2 p' = \underbrace{\frac{\partial}{\partial t}[\rho_0 v_n \delta(f)]}_{(monopole)} - \underbrace{\frac{\partial}{\partial x_i}[p n_i \delta f]}_{(dipole)} + \underbrace{\frac{\partial^2}{\partial x_i \partial x_j}[H(f) T_{ij}]}_{(quadrupole)} \tag{6.7}$$

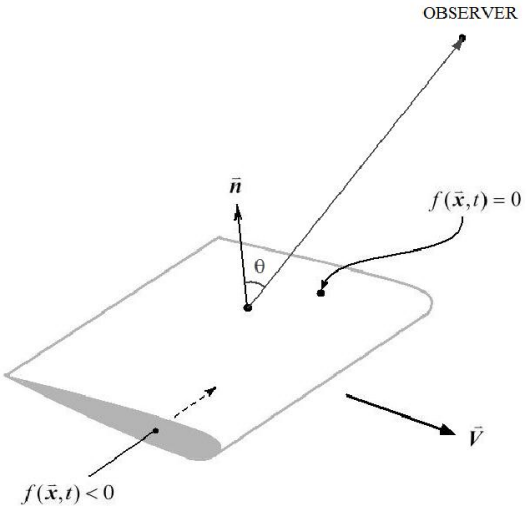

Figure 6.5: The definition of the moving surface as $f(x,t) = 0$.

where p' is the perturbation (acoustic) pressure, c is the ambient speed of sound, ρ_0 is the ambient density and p is the local pressure on the surface. $p' = c^2$, $\rho' = c^2(\rho - \rho_0)$ and p' can only be interpreted as the acoustic pressure if $\rho'/\rho_0 \ll 1$. The Heaviside and the Dirac delta functions are denoted as $H(f)$ and $\delta(f)$. Again, T_{ij} is the Lighthill stress tensor where all the nonlinearities from the equations of conservation of mass and momentum are lumped in. The above formulation is called the *impermeable surface* FW-H formulation.

It is important to mention that there are two variations of the FW-H formulations - the *impermeable surface* FW-H and the *permeable surface* FW-H. The latter is not to be discussed in this work, although it is worth mentioning briefly. The great advantage of the *permeable* FW-H formulation comes when one wants to account for the quadrupole source term. In that formulation, the control surface is a fictitious surface (not a solid body as shown in Fig. 6.4) which encloses some volume surrounding the solid body. This allows one to avoid the expensive volume integration for quadrupole source because the surface integration of this fictitious control surface includes the quadrupole noise source. The details about the *permeable* FW-H can be found in the original paper by FW-H [31] as well.

The three source terms in the FW-H equation, as indicated in the Eq. 6.7, have physical meanings. This is helpful in understanding the noise generation. The first source term is purely of geometrical nature and it describes the noise generation by the fluid displaced by the moving body. The associated field is called thickness noise and it has a monopole-type contribution. In the case of helicopter (propeller) noise, this is the dominant noise source. The second term depends on the normal surface stresses due to the pressure distribution. This is generated by the force that acts on the fluid as a result of the presence of the solid body. The associated field is called loading noise and it has a dipole-type contribution. In the case of airframe noise (in the absence of thickness noise), this is the dominant noise source. The third term is the contribution of the Lighthill stress tensor which accounts for that such as nonlinear effects, as explained previously in Sec. 6.2.1. This quadrupole term is a volume source and requires computationally expensive volume integration outside of the surface integration. This distinct separation of the three terms is useful in numerical computations because not all terms must be computed at all times if a particular source

does not contribute to the sound field. For instance, the contribution to the sound field from the Lighthill's stress tensor, the quadrupole source, is generally small and negligible at low Mach numbers. It only becomes non-negligible at high Mach numbers. For subsonic flows, quadrupole type radiation is also relatively inefficient in the presence of a monopole or dipole noise source as well. This can be shown by the scaling argument that relates the acoustic intensity $\mathbf{I}$ of the noise source to the convection velocity. Lighthill [65] showed that $\mathbf{I} \sim M^8$ for the quadrupole sources, where M indicates the Mach number. Later, Curle [20] had also shown that $\mathbf{I} \sim M^6$ for dipole sources and $\mathbf{I} \sim M^4$ for monopole sources. This implies:

$$\frac{\mathbf{I}_{quad.}}{\mathbf{I}_{di.}} \sim \frac{\mathbf{I}_{di.}}{\mathbf{I}_{mono.}} \sim M^2 \tag{6.8}$$

Neglecting the insignificant quadrupole term, the Eq. 6.7 can, in principle, be solved if the pressure distribution along the surface is known. By using a free field Green's function, Farassat [29] developed various versions of integral forms of the FW-H equation. Farassat's final formulation is presented below after bypassing the mathematical details:

$$p'(x,t) = p'_{Thickness}(x,t) + p'_{Loading}(x,t) \tag{6.9}$$

where

$$\begin{aligned} 4\pi p'_{Thickness}(x,t) &= \int_{f=0} \left[\frac{\rho_0 \dot{v}_n}{r(1-M_r)^2} + \frac{\rho_0 v_n \hat{r}_i \dot{M}_i}{r(1-M_r)^3} \right]_{ret} dS \\ &+ \int_{f=0} \left[\frac{\rho_0 c v_n (M_r - M^2)}{r^2 (1-M_r)^3} \right]_{ret} dS, \end{aligned} \tag{6.10}$$

$$4\pi p'_{Loading}(x,t) = \int_{f=0}\left[\frac{\dot{p}cos\theta}{cr(1-M_r)^2}+\frac{\hat{r}_i\dot{M}_i p cos\theta}{cr(1-M_r)^3}\right]_{ret} dS + \int_{f=0}\left[\frac{p(cos\theta-M_i n_i)}{r^2(1-M_r)^2}+\frac{(M_r-M^2)pcos\theta}{r^2(1-M_r)^3}\right]_{ret} dS \quad (6.11)$$

The subscript ret denotes evaluation at retarded time, $\tau = t - r/c_0$. $\hat{r}$ is the unit radiation vector and n is the surface normal vector. $\hat{r}_i$ is the component of unit radiation vector in each direction. Note that $cos\theta = n \cdot \hat{r}$ and $M_r = M \cdot \hat{r}$. The dot $\cdot$ refers to a time derivative of the variable.

This formulation is called the Formulation 1A of Farassat [27]. Other formulations of the solutions are also available which might be easier to handle in certain applications, see [27, 28]. It is important to be reminded that this formulation utilizes the free-space Green's function. The hard-wall boundary condition must be satisfied in order to use this formulation. Once its applicability is well justified, the Ffowcs-Williams and Hawkings equation is then ready to be used in conjunction with the CFD solutions.

6.5 Sound generated by flow over a circular cylinder

6.5.1 Benchmark case (Re=90,000)

The objective of this work is to calculate the far-field sound generated from low Mach number flow around a three-dimensional circular cylinder in the sub-critical regime using the Lighthill's acoustic analogy. As a benchmark based on the experimental work of Revell *et al.* [90], a flow with a Reynolds number of $Re = 90,000$ and a free-stream Mach number of $M = 0.2$ is simulated. The simulation is conducted in three-dimensional computational domains to account for the effects of the inherently three-dimensional flow at this Reynolds number. For low Mach number flows such as this case, the coupling between sound and flow fluctuations can usually be neglected. Thus, the source of noise can be computed separately from the acoustic field. Under this assumption, the far-field sound is computed using the FW-H approach. The collected flow-field data is input to the acoustic solver

to solve the Formulation 1A of Farassat (Eq. 6.10 and Eq. 6.11), provided that the noise source is verified to be acoustically compact, *i.e.,* the cylinder body is small relative to the acoustic wavelength associated with the vortex shedding.

For this benchmark case, the Formulation 1A of Farassat can be further simplified. Since the cylinder is stationary, the monopole sound source term (Eq. 6.10) yields zero. In this case, most of the noise is generated by the unsteady pressure fluctuations on the cylinder wall, contributing mostly to the dipole noise source term. At the current Mach number, the contribution from the quadrupole source in the turbulent wake region is also insignificant in the presence of the dipole source according to Eq. 6.8; hence it is also neglected. Starting from Eq. 6.11 and further simplifying for the case of a non-moving surface and neglecting the insignificant terms, the acoustic pressure in the far-field can be written as

$$4\pi p'_{Loading}(x,t) = \frac{1}{c_0}\int_{f=0}\left[\frac{\frac{\partial p}{\partial \tau}cos\theta}{r}\right]_{ret} dS \tag{6.12}$$

In the current acoustic solver, Eq. 6.12 is used for the far-field noise prediction. The subscript *"ret"* denotes evaluation at retarded time $\tau = t - r/c_0$, and θ is the angle between the radiation vector and the surface normal n (see Fig. 6.5). The retarded term in Eq. 6.12 must be interpolated in time at the observer position to find the values at the retarded time for the integration. This operation is necessary because the sampling at emission time from the source does not coincide with the sampling at receiving time. An accurate estimate of the derivative can be obtained using the Stirling formula, which is based on simple numerical differentiation theory. The formulation, given in [120], is as follows:

$$\begin{aligned}\frac{\partial p'}{\partial \tau} &= \frac{p_{\tau+1} - p_{\tau-1}}{2\tau} + \frac{\Delta\tau}{\tau}\left[p_{\tau+1} - 2p_\tau + p_{\tau-1}\right] \\ &\quad + \frac{[3\Delta\tau^2 - 1][p_{\tau+1} - 3p_\tau + 3p_{\tau-1} - p_{\tau-2}]}{12\tau}\end{aligned} \tag{6.13}$$

The computed noise predictions are compared with the experiment of Revell *et al.* [90] and other available numerical work [19, 82].

6.5.2 Flow-field prediction

MILES (Sec. 2.3.2) is employed to compute the unsteady flow-field using the ghost-cell based cut-cell method (Sec. 4.2.2) in conjunction with the wall function (Sec. 4.2.3). The computational domain size is $30D \times 20D \times 2.5D$ in the x (streamwise), y (cross-streamwise) and z (spanwise) directions, respectively, and the cylinder is immersed in the domain with centre at $(x, y) = (10D, 10D)$ (Fig. 6.6). The grid employs $300 \times 200 \times 25$ cells. In the x and y directions, the grid is stretched to cluster points in the vicinity of the cylinder to provide higher resolution. Δx and Δy in the vicinity of the cylinder is $0.02D$ while uniform grid spacing is applied in the z direction. This spatial mesh resolution near the wall yields y^+ values in the range of 0.3 to 164. At the inflow, subsonic non-reflecting inflow boundary conditions are implemented. At the three other sides of the domain (excluding the spanwise boundaries), subsonic non-reflecting outflow conditions are used.

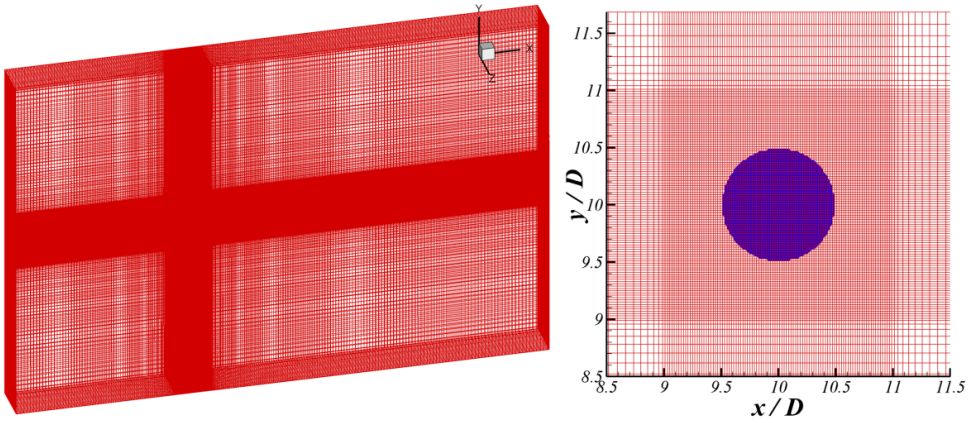

Figure 6.6: The rectangular Cartesian grid domain and a close up view of the grid around the cylinder in the x-y plane ($Re = 90,000$). Every grid point is shown.

Fig. 6.7 shows portions of the time histories of C_L and C_D. It illustrates difficulties experienced by the computations near this critical Reynolds number. Relative to the earlier

test case of flow over a cylinder at $Re = 300$ (Sec. 5.2.1), an amplitude modulation of the lift forces is observed, mainly due to the strong occurrence of the irregular vortex break-up along the cylinder span, leading to a three-dimensional vortex shedding. Comparing the mean quantities against the experimental analysis [11], the current CFD predicts well with $S_t = 0.207$ and $C_D = 1.33$ (Table 6.1). It can be noted that the unsteady RANS results by Cox *et al.* [19] generally over-predicts S_t and under-predicts C_D with some variations depending on the turbulence model used. The current results are comparable to the wall-resolved 3D-LES results by Orselli *et al.*[1] [82]. In order to show the three-dimensional flow structures in the cylinder wake, the isosurfaces of transverse vorticity magnitude in the wake at one time instant is illustrated in Fig. 6.8.

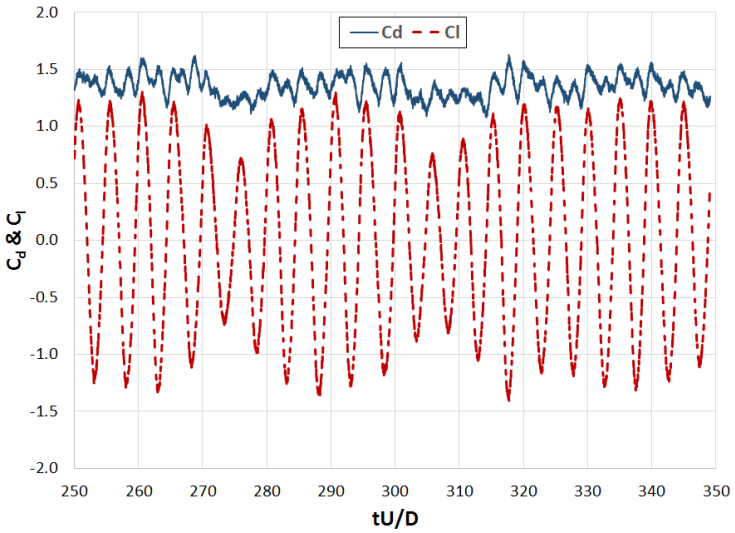

Figure 6.7: Temporal variation of drag and lift coefficient ($Re = 90,000$).

6.5.3 Acoustic prediction

For sound calculation, the experimental data by Revell *et al.* [90] is used as a benchmark case. Their work used a free jet flow over a circular cylinder placed inside an anechoic

[1]incompressible, wall-resolved LES on 5.4 million hexahedral-type volume cells. The present work employs 1.5 million Cartesian volume cells.

Table 6.1: Comparison of obtained S_t and C_D with experimental data and other numerical data. For RANS predictions, Cox *et al.* [19] used a compressible flow solver (CFL3D) and an incompressible flow solver (CITY3D).

Case	S_t	C_D
Experimental data [11]	0.18-0.20	0.98-1.35
RANS SST (comp. solver) [19]	0.227	0.804
RANS k-ϵ (comp. solver) [19]	0.233	0.625
RANS k-ϵ (incomp. solver) [19]	0.296	0.582
3D-LES [82]	0.191	1.08
present 3D-LES w/ wall function	0.207	1.33

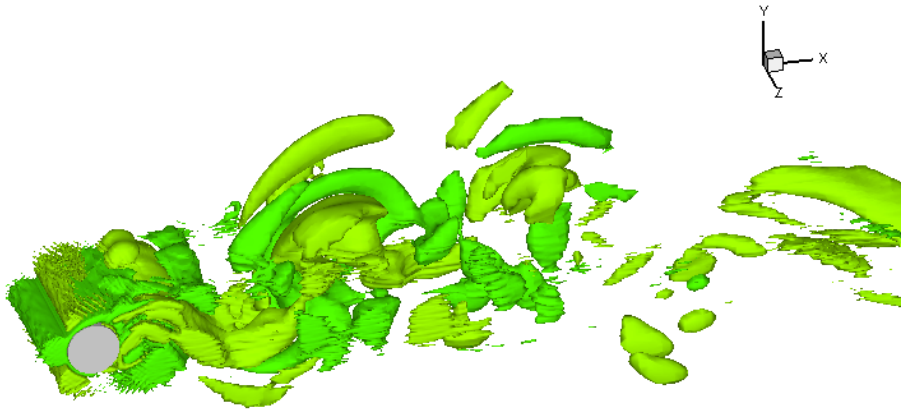

Figure 6.8: Isosurfaces of transverse vorticity magnitude at an instant of time in the vicinity of the circular cylinder ($Re = 90,000$).

wind tunnel to obtain aerodynamic quantities and far-field acoustic spectra. Their smooth circular cylinder with a diameter of $D = 0.019m$, measured under $Re = 89,000$ and $M = 0.2$ is considered here. The span length of the cylinder is $L = 26.3D$ $(0.5m)$. The location of the microphone is 90° from the free-stream direction and is $128D$ away from the mid-span of the cylinder. The unsteady surface pressures are recorded at every $2 \times 10^{-6}s$ which is equivalent to a sampling rate of 500 kHz. On the order of 500 timesteps per acoustic period is generally sufficient to ensure an adequate temporal resolution [19]. The appropriate time step should be related to resolving the highest frequency from the range of interest, and this poses an extremely stringent resolution requirement on lower frequencies. In this particular benchmark case, high-frequency noises (quadrupole source) are neglected. The sound source is due to the pressure fluctuation on the cylinder surface, which sheds a vortex at a Strouhal number of 0.2 ($\approx$ 722 Hz). The dipole directivity pattern is assumed (such that there is no complex scattering field) because the cylinder cross section is acoustically compact. As the wavelength corresponding to the shedding frequency ($\approx 0.47m$) is indeed large compared with the diameter of the cylinder ($0.019m$), this approximation is actually very good in this flow condition. The applicability of Formulation 1A of Farassat for this benchmark case is also justified.

The chosen sampling rate (500 kHz) yields approximately 690 timesteps per shedding cycle for the noise at this frequency. The CFD simulation is run to obtain approximately 60 shedding cycles (*i.e.* $690 \times 60 = 41400$ total timesteps). Due to computational cost limitations, a shorter cylinder span of $L_s = 2.5D$ is used in the CFD simulation as opposed to $L = 26.3D$ used in the experiment. The time history of surface pressures is processed through the Fast Fourier Transform (FFT) for a spectral analysis. In order to account for the additional sound pressure level (SPL) generated due to the longer span of the cylinder, SPL for the simulated span (L_s) must be corrected. In this work, the acoustic correction method proposed by Kato *et al.* [54] is used. The basic idea is to estimate a SPL correction (SPL_c) for the short cylinder span (L_s), which can be added to account for the longer span. Sound pressure level correction for the long span can be made by adding $10log(L/L_s)$ if a coherence length of the surface pressure fluctuations along the cylinder span, L_c, is determined to be less than the simulated span, *i.e.* $L_c \leq L_s$. If $L_c > L$, then

$20log(L/L_s)$ must be added. The SPL to be corrected for the long span, L is given by

$$SPL_c = \begin{cases} 10\ \log(\frac{L}{L_s}) & (L_c \leq L_s), \\ 20\ \log(\frac{L_c}{L_s}) + 10\ \log(\frac{L}{L_c}) & L_s < L_c < L, \\ 20\ \log(\frac{L}{L_s}) & L \leq L_c. \end{cases} \tag{6.14}$$

L_c is the spanwise coherence length, which is also a function of frequency ($L_c = L_c(\omega)$). The first expression assumes that the fluctuating pressure for spanwise distance beyond L_s is not correlated, whereas the third expression assumes a perfect correlation of the fluctuating pressure along the cylinder span L. According to Kato *et al.* [54], the degree of coherence of the fluctuating surface pressure along the cylinder span can be represented by an equivalent coherence length, $L_c(\omega)$, which is the only unknown value of the corrected method. This study simply follows the work of Orselli *et al.* [82] where the $L_c(\omega)$ for $St = 0.20$, 0.38 and 0.76 are found to be $7.86D$, $0.56D$ and $0.074D$ respectively. Near the von Karman vortex shedding frequency ($St \approx 0.207$), $L_c = 7.86D$ falls within the range $L_s < L_c(\omega) < L$ of Kato's formulation (Eq. 6.14). For the other two frequencies ($St = 0.38$ and 0.76), L_c is lower than L_s, indicating that other frequencies (higher than $St = 0.20$) falls in the range, $L_c \leq L_s$. Thus, at the vortex shedding frequency, the sound spectrum is corrected by adding a value of $SPL_c(St = 0.20) = 15.0dB$ after using the second expression in Eq. 6.14. At higher frequencies, the sound is corrected by adding $SPL_c(St = 0.20) = 10.1dB$ due to the first expression. The uncorrected and corrected sound spectra are presented and compared with the experimental results in Fig. 6.9. Comparison of the experimental and the numerical spectra at the vortex shedding frequency ($St = 0.20$) shows that the predicted peak of SPL after the acoustic correction ($\approx 101.3dB$) matches well with corresponding value of Revell *et al.* [90] ($\approx 98.4dB$). Overall, the present acoustic computations agree well with the experimental data.

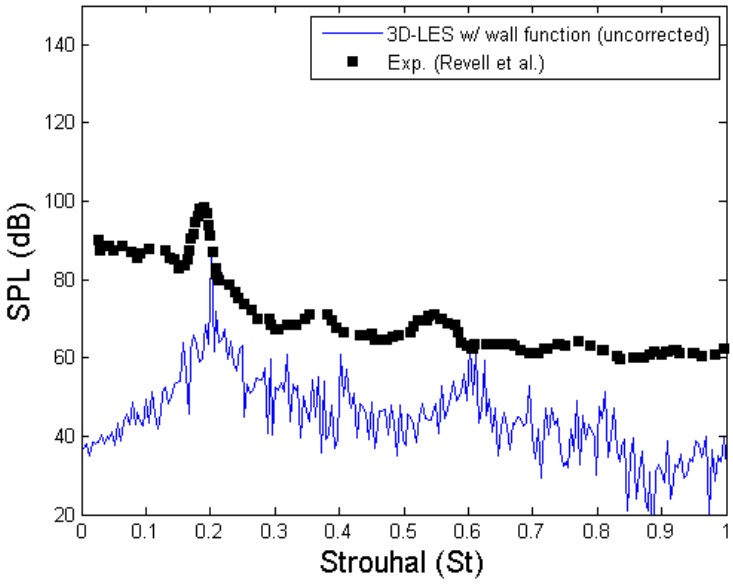

(a) Uncorrected

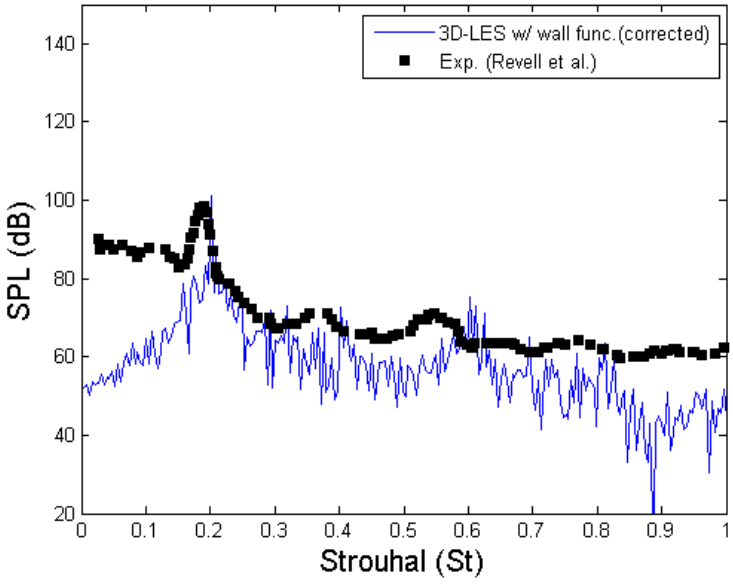

(b) Corrected

Figure 6.9: Comparison of predicted and measured sound pressure level for a microphone located $128D$ away from the cylinder and at 90° from the stagnation point.

6.6 Conclusions

Of many hybrid approaches available in computational aeroacoustics, the Ffowcs-Williams and Hawkings (FW-H) approach is selected for the far-field acoustic calculation. Once the applicability is justified, this integral approach becomes a powerful tool for an acoustical prediction in terms of efficiency and accuracy. Because the fundamental equations are reduced to an inhomogeneous wave equation where the integral formulation is known, prediction of wave propagation is simple.

As a benchmark, prediction of far-field noise generated from low Mach number flow around a circular cylinder in the sub-critical regime is performed using the FW-H approach. The flow-field is obtained by LES using the GC-CCM and a wall-function, as similarly demonstrated in the previous chapter. Due to limitations on computational resources, a shorter cylinder span is used in the CFD computations. To account for the additional sound level generated by the longer span, the acoustic correction method proposed by Kato *et al.* [54] is applied. The computed sound spectrum agrees well with the corresponding experimental data of Revell *et al.* [90]. The results demonstrate that the developed hybrid LES-acoustic analogy method, where the flow-field is computed using the GC-CCM and a simple wall-function, can predict the sound spectrum quite accurately for the case of a three-dimensional flow around a cylinder in the sub-critical regime. For future studies, similar LES simulations with more complex geometries, such as wings, high-lift system or landing gear, should be carried out for the airframe noise predictions.

Chapter 7

Conclusions and Recommendations

7.1 Summary

In the present study, a hybrid LES-acoustic analogy method for computational aeroacoustics has been developed. The intention here is to develop CFD and acoustic methodologies for an accurate prediction of far-field noise that results from flow over complex geometries. Generating high quality body fitted grids around complex geometries is challenging and time-consuming. As an alternative, numerical methods based on non-body conformal grids are developed and assessed; these methods can deal with bodies of almost arbitrary shape. Two non-body conformal grid methods are proposed and assessed in this work: the ghost-cell based immersed boundary method (GC-IBM) and the ghost-cell based cut-cell method (GC-CCM). The applicability of these methods is investigated extensively in the compressible LES framework. The developed methods are tested for a wide range of Reynolds numbers as well as Mach numbers. The test cases include flows over a cylinder, a wavy surface, and through an inclined turbulent channel. For high Reynolds number flows, a wall model is employed to approximate the wall-shear stress and avoid a requirement for severe grid resolution near the wall. The successfully developed CFD methodology for a sound source is then used in an aeroacoustic application to predict the far-field radiated noise. The test case used here is the prediction of sound generated by flow over a circular

cylinder. Several approaches can be used in the acoustic solver for the sound propagation. Of many hybrid approaches available in the computational aeroacoustics, the Ffowcs Williams-Hawkings (FW-H) acoustic analogy is selected to explore the far-field acoustic calculation due to its versatility and efficiency. The numerical results are compared to the experimental data and predict the sound spectral quite accurately.

7.2 Contributions

Although the research is driven to achieve an accurate far-field acoustic prediction, the majority of the work contributing to this research is focused on solving the turbulent flow-field, that is, the noise source. In particular, the focus is to accurately perform LES of turbulent compressible flows in a complex geometric setting using non-body conformal methods. As such, the research is mainly dedicated to develop efficient, easy-to-implement and relatively accurate non-body conformal methods that can be used for flow over complex geometries.

First, the original ghost-cell based immersed boundary method (GC-IBM) of Tseng and Ferziger [112] is extended for compressible turbulent flows. The treatment of the ghost cells comes from the proper boundary conditions enforced on the immersed boundary through image points in the fluid region. This method is successfully applied to LES of compressible turbulent flow associated with wavy wall geometries. The results agree reasonably well with the DNS data. In order to demonstrate the robustness of the current method for higher Mach number flows, a supersonic flow over a cylinder at a moderately high Reynolds number is simulated. The results nicely capture the qualitative behaviour of the supersonic flow in the vicinity of the cylinder and demonstrate the validity and flexibility of the GC-IBM algorithm in the compressible LES framework.

Second, a new method called ghost-cell based cut-cell method (GC-CCM) is developed. This method utilizes both ghost cells and cut cell methodologies. For improved accuracy near the wall, cell faces are decomposed and the fluxes are evaluated through each face component. The presented methodology does not require storing information at the centre

of small cut cells and at the centroid of merged cells, as in previous cut cell approaches. A simple wall-function approach is used to approximate the wall-shear stress and the discretization error is used to model the sub-grid scale turbulence (implicit LES), although both of these models can be replaced by others if desired. The results confirm that the proposed method agrees well with the reference data despite the employment of coarse grids. It represents the flow physics in the vicinity of the solid boundary more accurately than the other non-body conformal methods compared in this work.

Last, but certainly not least, prediction of far-field noise generated from flow around a circular cylinder in the sub-critical regime is performed using the Ffowcs Williams and Hawkings (FW-H) approach. The unsteady flow-field, *i.e.*, the sound-generating mechanism, is provided by performing LES using the GC-CCM and a wall-function. To reduce the computational cost, a shorter cylinder span is used in the CFD simulations than that used in the reference experimental work by Revell *et al.* [90]. The sound level is then corrected using an acoustic correction method to account for the longer cylinder span. Both CFD and acoustic results agree well with the corresponding experimental data.

7.3 Recommendations for future work

The present study shows the proposed non-body conformal grid method to be efficient, easy-to-implement and relatively accurate compared to other non-body conformal methods. To conclude whether they are also accurate compared with the body-fitted grid formulations, one needs to analyze the performance of the proposed method against body-fitted grids. One such comparative study has been carried out by Meyer *et al.* [75], who showed that their cut-cell formulation and the equivalent body-fitted formulation result in similar accuracies for turbulent statistics and mean integral quantities. It will be important to conduct a similar study with the current method where a wall model is in place.

The current study uses a simple wall model based on a wall function. The accuracy can be further improved using a more sophisticated wall model. It will be important to assess the effect of a wall model and to compare the numerical results using various wall

models.

In order to achieve the research goal that the author ultimately envisioned, namely, an accurate airframe noise prediction, similar LES simulations with more complex geometries, such as wings, high-lift system or landing gear, should be performed. Using the acoustic solver, their far-field noise should be predicted and compared to the existing data.

APPENDICES

Appendix A

Navier-Stokes Characteristic Boundary Condition

A.1 Characteristic analysis for x-direction

Although the system of governing equations (2.1 - 2.3) are written in terms of conservative variables, they can also be written in terms of primitive variables. Let $\tilde{U}$ be the conservative variable vector (as defined in Eq. 3.3) and U be the primitive vector, $[\rho, u, v, w, p]^T$. The two systems are related by

$$\frac{\partial \tilde{U}}{\partial t} = P \frac{\partial U}{\partial t} \quad \text{where} \quad P = \frac{\partial \tilde{U}}{\partial U}. \tag{A.1}$$

P is the Jacobian matrix. Similarly,

$$\frac{\partial F_k}{\partial x_k} = Q_k \frac{\partial U}{\partial x_k} \quad \text{where} \quad Q_k = \frac{\partial F_k}{\partial U}. \tag{A.2}$$

where k denotes x, y or z directions.

For characteristic analysis for x-direction,

$$\frac{\partial \tilde{U}}{\partial t} + \frac{\partial F_x}{\partial x} + \tilde{C} = 0 \quad \text{where} \quad \tilde{C} = \frac{\partial F_y}{\partial y} + \frac{\partial F_z}{\partial z} + \tilde{D}. \tag{A.3}$$

This can be written in terms of primitive variable as

$$\frac{\partial U}{\partial t} + A_x \frac{\partial U}{\partial x} + C = 0 \quad \text{where} \quad C = A_y \frac{\partial U}{\partial y} + A_z \frac{\partial U}{\partial z} + D. \tag{A.4}$$

$A_k = P^{-1} Q_k$, $C = P^{-1}\tilde{C}$ and $D = P^{-1}\tilde{D}$.

Let l_i and r_i are left and right eigenvectors of A_x such that

$$l_i^T A_x = \lambda_i l_i^T \ , \quad A_x r_i = \lambda_i r_i \ , \quad i = 1, ..., m \tag{A.5}$$

where eigenvalues λ_i are given by $det(A_x - \lambda I) = 0$ and the left and right eigenvectors are mutually orthogonal as $l_i^T \cdot r_j = \delta_{ij}$.

A diagonalizing similarity transformation is generated for A_x by forming the matrix S such that its columns are the right eigenvectors r_j. S^{-1} is the left eigenvectors l_i^T. The similarity transformation is then

$$S^{-1} A_x S = \Lambda \tag{A.6}$$

where Λ is the diagonal matrix of eigenvalues. Applying this transformation to Eq. A.4 gives

$$S^{-1} \frac{\partial U}{\partial t} + \Lambda S^{-1} \frac{\partial U}{\partial x} + S^{-1} C = 0 \tag{A.7}$$

whose m components are

$$l^T \frac{\partial U}{\partial t} + \lambda_i l_i^T \frac{\partial U}{\partial x} + l_i^T C = 0 \quad , \quad i = 1, ..., m \tag{A.8}$$

To make the boundary condition analysis more convenient, the i^{th} component of the vector $\mathcal{L}$ is

$$\mathcal{L}_i \equiv \lambda_i l_i^T \frac{\partial U}{\partial x_i}. \tag{A.9}$$

The Eq. A.7 can then be rewritten as

$$S^{-1}\frac{\partial U}{\partial t} + \mathcal{L} + S^{-1}C = 0 \tag{A.10}$$

or, in the component form of Eq. A.11 as

$$l^T \frac{\partial U}{\partial t} + \mathcal{L}_i + l_i^T C = 0 \quad , \quad i = 1, ..., m \tag{A.11}$$

Eigenvalues of A_x in Eq. A.4 are

$$\lambda_1 = u - c \quad , \quad \lambda_2 = \lambda_3 = \lambda_4 = u \quad , \quad \lambda_5 = u + c \tag{A.12}$$

where c is the speed of sound, $c^2 = \frac{\gamma p}{\rho}$. Eigenvalues of λ_1 and λ_5 are the velocities of the sound waves moving in the negative and positive x directions, λ_2 is the velocity for entropy advection, while λ_3 and λ_4 are the velocities at which v and w are advected in the x direction.

The left eigenvectors are written as

$$\begin{aligned}
l_1^T &= (0, 1, -\rho c, 0, 0), \\
l_2^T &= (c^2, -1, 0, 0, 0), \\
l_3^T &= (0, 0, 0, 1, 0), \\
l_4^T &= (0.0.0.0.1), \\
l_5^T &= (0, 1, \rho c, 0, 0).
\end{aligned} \tag{A.13}$$

The quantities $\mathcal{L}_i$ from Eq. A.9 are formed as

$$\begin{aligned}
\mathcal{L}_1 &= \lambda_1(\frac{\partial p}{\partial x} - \rho c\frac{\partial u_1}{\partial x}),\\
\mathcal{L}_2 &= \lambda_2(c^2\frac{\partial \rho}{\partial x} - \frac{\partial p}{\partial x}),\\
\mathcal{L}_3 &= \lambda_3\frac{\partial v}{\partial x},\\
\mathcal{L}_4 &= \lambda_4\frac{\partial w}{\partial x},\\
\mathcal{L}_5 &= \lambda_5(\frac{\partial p}{\partial x} + \rho c\frac{\partial u}{\partial x}).
\end{aligned} \tag{A.14}$$

These definitions may be inverted to give

$$\begin{aligned}
\frac{\partial \rho}{\partial x} &= \frac{1}{c^2}\left[\frac{\mathcal{L}_2}{u} + \frac{1}{2}(\frac{\mathcal{L}_5}{u+c} + \frac{\mathcal{L}_1}{u-c})\right],\\
\frac{\partial u}{\partial x} &= \frac{1}{2\rho c}\left(\frac{\mathcal{L}_5}{u+c} - \frac{\mathcal{L}_1}{u-c}\right),\\
\frac{\partial v}{\partial x} &= \frac{\mathcal{L}_3}{u},\\
\frac{\partial w}{\partial x} &= \frac{\mathcal{L}_4}{u}.\\
\frac{\partial p}{\partial x} &= \frac{1}{2}\left(\frac{\mathcal{L}_5}{u+c} + \frac{\mathcal{L}_1}{u-c}\right),
\end{aligned} \tag{A.15}$$

Then, $S\mathcal{L}$ can be written as

$$d \equiv S\mathcal{L} = \begin{pmatrix} 1/c^2[\mathcal{L}_2 + 1/2(\mathcal{L}_5 + \mathcal{L}_1)] \\ (1/2)(\mathcal{L}_5 + \mathcal{L}_1) \\ (1/2\rho c)(\mathcal{L}_5 - \mathcal{L}_1) \\ \mathcal{L}_3 \\ \mathcal{L}_4 \end{pmatrix} = \begin{pmatrix} d_1 \\ d_2 \\ d_3 \\ d_4 \\ d_5 \end{pmatrix} \tag{A.16}$$

The Eq. A.10 can be multiplied by the similarity transformation matrix S on both sides, where the above $S\mathcal{L}$ can be substituted to rewrite the primitive equations in the form. Multiplying the governing equations in the primitive form by the Jacobian matrix P to give

$$
\begin{aligned}
\frac{\partial \rho}{\partial t} + d_1 + \frac{\partial(\rho v)}{\partial y} + \frac{\partial(\rho w)}{\partial z} &= 0, \\
\frac{\partial(\rho u)}{\partial t} + u d_1 + \rho d_3 + \frac{\partial(\rho u)v}{\partial y} + \frac{\partial(\rho u)w}{\partial z} &= \frac{\partial \tau_{1j}}{\partial x_j}, \\
\frac{\partial(\rho v)}{\partial t} + v d_1 + \rho d_4 + \frac{\partial(\rho v)v}{\partial y} + \frac{\partial(\rho v)w}{\partial z} + \frac{\partial p}{\partial y} &= \frac{\partial \tau_{2j}}{\partial x_j}, \\
\frac{\partial(\rho w)}{\partial t} + w d_1 + \rho d_5 + \frac{\partial(\rho w)v}{\partial y} + \frac{\partial(\rho w)w}{\partial z} + \frac{\partial p}{\partial z} &= \frac{\partial \tau_{3j}}{\partial x_j}, \\
\frac{\partial \rho E}{\partial t} + \frac{1}{2}(u_k u_k) d_1 + \frac{d_2}{\gamma - 1} + (\rho u) d_3 + (\rho v) d_4 + (\rho w) d_5 & \\
+ \frac{\partial}{\partial y}[(\rho E + p)v] + \frac{\partial}{\partial z}[(\rho E + p)w] &= \\
\frac{\partial(u_j \tau_{ij})}{\partial x_i} - \frac{\partial q_i}{\partial x_i}. &
\end{aligned}
\tag{A.17}
$$

References

[1] AS Almgren, JB Bell, P. Colella, and T. Marthaler. A cartesian grid projection method for the incompressible Euler equations in complex geometries. *SIAM J Sci Comput*, 18:1289, 1997.

[2] E. Balaras. Modeling complex boundaries using an external force field on fixed cartesian grids in large-eddy simulations. *Computers and Fluids*, 33:375–404, 2004.

[3] F. Bashforth and J.C. Adams. *Theories of Capillary Action*. London,Cambridge University Press, 1883.

[4] V.A. Bashkin, A.V. Vaganov, I.V. Egorov, D.V. Ivanov, and G.A. Ignatova. Comparison of calculated and experimental data on supersonic flow past a cylinder. *Fluid Dynanmics*, 37:473–483, 2002.

[5] MJ Berger and R LeVeque. A rotated difference scheme for Cartesian grids in complex geometries. *AIAA 10th computational fluid dynamics conference, Honolulu, Hawaii*, p.1, 1991.

[6] J. Boris, F. Grinstein, E. Oran, and R. Kolbe. New insights into large eddy simulation. *Fluid Dynamics Research*, 10:199–228, 1992.

[7] K.S. Brentner and F. Farassat. An analytical comparison of the acoustic analogy and Kirchhoff formulation for moving surfaces. *AIAA Journal*, 36 (8):1379–1386, 1998.

[8] M. Breuer and W. Rodi. Large eddy simulation of complex turbulent flows of practical interest. *Flow simulation with High Performance Computers II*, 52 of Notes on Numerical Fluid Mechnics:258–274, 1996.

[9] A. Burbeau and P. Sagaut. Simulation of a viscous compressible flow past a circular cylinder with high-order discontinuous Galerkin methods. *Computers and Fluids*, 31:867–889, 2002.

[10] R.J. Calhoun and R.L. Street. Turbulent flow over a wavy surface: Neutral case. *Journal of Geophysical Research*, 106:9277–9293, 2001.

[11] B. Cantwell and D. Coles. An experimental study of entrainment and transport in the turbulent near wake of circular cylinder. *J. Fluid Mech.*, 136:321–374, 1983.

[12] F. Capizzano. A turbulent wall model for immersed boundary methods. *AIAA Journal*, 49(11):2367–2381, 2011.

[13] Z. Chen, S.Hickel, and A.Devesa. Wall modeling for implicit large-eddy simulation and immersed-interface methods. *Theor. Comput. Fluid Dyn.*, 28:1–21, 2014.

[14] P. Cherukat, Y. Na, and T.J. Hanratty. Direct numerical simulation of a fully developed turbulent flow over a wavy wall. *Theoretical and Computational Fluid Dynamics*, 11:109–134, 1997.

[15] F. Chow and P. Moin. A further study of numerical errors in large-eddy simulations. *Journal of Computational Physics*, 184:366–380, 2003.

[16] D. Clarke, M. Salas, and H. Hassan. Euler calculations for multi-element airfoils using Cartesian grids. *AIAA Journal*, 24 (3):353–358, 1986.

[17] P. Colella, D.T. Graves, B.J. Keen, and D. Modiano. A Cartesian grid embbeded boundary method for hyperbolic conservation laws. *Journal of Computational Physics*, 211:347–366, 2006.

[18] P. Colella and P. Woodward. The piecewise parabolic method (PPM) for gasdynamical simulations. *Journal of Computational Physics*, 54:174–210, 1984.

[19] J.S. Cox, C.L. Rumsey, and B.A. Younis. Computation of sound generated by flow over a circular cylinder: An acoustic analogy approach. *NASA Technical Memorandum 110339*, 1997.

[20] N. Curle. The influence of solid boundaries on aerodynamic sound. *proceeding of the Royal Society of London*, A231:505–514, 1955.

[21] M.D. de Tullio and G. Iaccarino. Immersed boundary technique for compressible flow simulations on semi-structured meshes. *Center for Turbulence Research, Annual Research Briefs 2005*, pages 71–83, 2005.

[22] M.D. de Tullio, P. De Palma, G. Iaccarino, G. Pascazio, and M. Napolitano. An immersed boundary method for compressible flows using local grid refinement. *Journal of Computational Physics*, 225:2098–2117, 2007.

[23] H.G. Dimopoulous and T.J. Hanratty. Velocity gradients at the wall for flow around a cylinder for reynolds number between 60 and 360. *J. Fluid Mech.*, 33:303–319, 1968.

[24] P. Dutt. Stable boundary conditions and difference schemes for Navier-Stokes equations. *SIAM J. Numer. Anal.*, 25-2:245–267, 1988.

[25] G. Erlebacher, M.Y. Hussaini, C.G. Speziale, and T.A. Zang. Toward the large-eddy simulation of compressible turbulent flows. *Journals of Fluid Mechanics*, 238:155–185, 1992.

[26] E.A. Fadlun, R. Verzicco, P. Orlandi, and J. Mohd-Yusof. Combined immersed-boundary finite-difference methods for three-dimensional complex flow simulations. *Journal of Computational Physics*, 161:30–60, 2000.

[27] F. Farassat. Discontinuities in aerodynamics and aeroacoustics: the concept and application of generalized derivatives. *Journal of Sound and Vibration*, 55:165–193, 1977.

[28] F. Farassat. Linear acoustic formulas for calculation of rotating blade noise. *AIAA Journal*, 19(9):1122–1130, 1981.

[29] F. Farassat. Derivation of formulation 1 and 1a of farassat. *NASA-TM-2007-214842, available at http://ntrs.nasa.gov*, 2007.

[30] F.E.Gowen and E.W.Perkins. Drag of circular cylinders for a wide range of reynolds numbers and mach numbers. *Technical Note 2960*, 1953.

[31] J.E. Ffowcs-Williams and D.L. Hawkings. Sound generation by turbulence and surfaces in arbitrary motion. *Philosophical Transactions of the Royal Society*, A264:321–342, 1969.

[32] E. Garnier, M. Mossi, P. Sagaut, P. Comte, and M. Deville. On the use of shock-capturing schemes for large-eddy simulation. *Journal of Computational Physics*, 153:273–311, 1999.

[33] R. Ghias, R. Mittal, and H. Dong. A sharp interface immersed boundary method for compressible viscous flows. *Journal of Computational Physics*, 225:528–553, 2007.

[34] S. Ghosal. An analysis of numerical errors in large-eddy simulations of turbulence. *Journal of Computational Physics*, 125:187–206, 1996.

[35] S. Ghosal and P. Moin. The basic equations for the large eddy simulation of turbulent flows in complex geometry. *Journal of Computational Physics*, 118:24–37, 1995.

[36] S.K. Godunov. A difference method for numerical calculation of discontinuous solutions of the equations of hydrodynamics. *Matematischeskii Sbornik*, 47:271–306, 1959.

[37] D. Goldstein, R. Handler, and L. Sirovich. Modeling and no-slip flow boundary with an external force field. *Journal of Computational Physics*, 105:354–366, 1993.

[38] D. Goldstein, R. Handler, and L. Sirovich. Direct numerical simulation of turbulent flow over a modelled riblet covered surface. *Journal of Computational Physics*, 302:333–376, 1995.

[39] M.E. Goldstein. *Aeroacoustics*. McGraw-Hill Book Company Inc., New York, 1976.

[40] J.J. Gottlieb and C.P.T. Groth. Assessment of Riemann solvers for unsteady one-dimensional inviscid flows of perfect gases. *Journal of Computational Physics*, 78:437–458, 1988.

[41] J. Gullbrand and F.K. Chow. The effect of numerical errors and turbulence models in large-eddy simulations of channel flow, with and without explicit filtering. *Journal of Fluid Mechanics*, 495:323–341, 2003.

[42] T. Hagstrom and S.I. Hariharan. Accurate boundary conditions for exterior problems in gas dynamics. *Mathematics of Computation*, 51:581–597, 1988.

[43] R. Hannappel, T. Hauser, and R. Friedrich. A comparison of ENO and TVD schemes for the computation of shock-turbulence interaction. *Journal of Computational Physics*, 121:176–184, 1995.

[44] A. Harten, B. Enquist, S. Osher, and S.R. Chakravarthy. Uniformly high order accurate essentially non-oscillatory schemes, iii. *Journal oc Computational physics*, 25:35–61, 1987.

[45] A. Harten, P. Lax, and B. van Leer. On upstream differencing and Godunov-Type schemes for hyperbolic conservation laws. *SIAM Review*, 25(1):35–62, 1983.

[46] D. Hartmann, M. Meinke, and W. Schroeder. An adaptive multilevel multigrid formulation for cartesian hierarchical grid methods. *Computers and Fluids*, 37:1103–1125, 2008.

[47] D. Hartmann, M. Meinke, and W. Schroeder. A strictly conservative cartesian cut-cell method for compressible viscous flows on adaptive grids. *Comp. Methods Appl. Mech. Engrg.*, 200:1038–1052, 2010.

[48] S. Hickel and N.A. Adams. On implicit subgrid-scale modeling in wall-bounded flows. *Physics of Fluids*, 19:105106–1105106–13, 2007.

[49] C. Hirsch. *Numerical Computation of Internal and External Flows, Volume 2, Computational Methods for Inviscid and Viscous Flows*. Toronto, John Wiley and Son, 1990.

[50] S. Hoyas and J. Jimenez. Scaling of the velocity fluctuations in turbulent channels up to re = 2003. *Physics of Fluids*, 18:011702, 2006.

[51] X.Y. Hu, B.C. Khoo, N.A. Adams, and F.L. Huang. A conservative interface method for compressible flows. *Journal of Computational Physics*, 219:553–578, 2006.

[52] H. Ji, F. Lien, and E. Yee. Numerical simulation of detonation using an adaptive cartesian cut-cell method combined with a cell-merging technique. *Computers and Fluids*, 39:1041–1057, 2010.

[53] G. Kalitzin and G. Iaccarino. Turbulence modeling in an immersed boundary rans method. *CTR Annual Briefs*, 2002.

[54] C. Kato, A. Lida, Y. Takano, H. Fujita, and M. Ikegawa. Numerical prediction of aerodynamic noise radiated from low mach number turbulent wake. *AIAA paper*, pages 93–145, 1993.

[55] J. Kim, D. Kim, and H. Choi. An immersed-boundary finite-volume method for simulations of flow in complex geometries. *Journal of Computational Physics*, 171:132–150, 2001.

[56] M. Kirkpatrick, S. Armfield, and J. Kent. A representation of curved boundaries for the solution of the Navier-Stokes equations on a staggered three-dimensional Cartesian grid. *Journal of Computational Physics*, 184:1–36, 2003.

[57] D. Knight, G. Zhou, N. Okong'o, and V. Shukla. Compressible large-eddy simulation using unstructured grids. *AIAA paper*, pages 98–0535, 1998.

[58] M. Lai and C.S. Peskin. An immersed boundary method with formal second-order accuracy and reduced numerical viscosity. *Journal of Computational Physics*, pages 705–719, 2000.

[59] N. Lamarque, M. Porta, F. Nicoud, and T. Poinsot. On the stability and dissipation of wall boundary conditions for compressible flows. *Int. J. Numer. Meth. Fluids*, 00:1–6, 2000.

[60] J. Lee and S.M. Rufflin. Development of a turbulent wall-function based viscous Cartesian grid methodology. *AIAA Paper*, pages 2007–1326, 2007.

[61] B. Van Leer. Towards the ultimate conservative difference scheme iii. upstream-centered finite-difference schemes for ideal compressible flow. *J.Comp.Phys.*, 23(3):263–275, 1977.

[62] A. Legay, J. Chessa, and T. Belytschko. An Eulerian-Lagrangian method for fluid-structure interaction based on level sets. *Comput. Methods Appl. Mech. Eng.*, 195:2070–2087, 2006.

[63] R.J. LeVeque. *Finite Volume Methods for Hyperbolic Problems*. London,Cambridge University Press, 2002.

[64] F. Lien and M. Leschziner. Upstream monotonic interpolation for scalar transport with application to complex turbulent flows. *Int. J. Num. Meth. Fluids*, 19:527–548, 1994.

[65] M.J. Lighthill. On sound generated aerodynamically, i. general theory. *Proceedings of the Royal Society of London*, A211:564–587, 1952.

[66] M. Liou and C. Steffen. A new flux splitting scheme. *Journal of Computational Physics*, 107:23–39, 1993.

[67] M.S. Liou and C.J. Steffen. A sequal to AUSM: AUSM+. *Journal of Computational Physics*, 129:364–382, 1996.

[68] H. Lomax, T.H. Pulliam, and D.W. Zingg. *Fundamentals of Computational Fluid Dynamics*. Springer, 2003.

[69] T.S. Lund. On dynamic models for large eddy simulation. *Annual Research Briefs, Center for Turbulence Research, Stanford University*, 177, 1991.

[70] S. Majumdar, G. Iaccarino, and P. Durbin. RANS solvers with adaptive structure boundary non-conforming grids. *Center for Turbulence Research Annual Research Briefs*, pages 353–366, 2001.

[71] M.P. Martin, U. Piomelli, and G.V. Candler. Subgrid-scale models for compressible large-eddy simulations. *Theoretical and Computational Fluid Dynamics*, 13:361–376, 2000.

[72] H. Matsui and B. Buffett. Commutation error correction for large eddy simulations of convection driven dynamos. *Geophysical and Astrophysical Fluid Dynamics*, 101:429–449, 2007.

[73] C. Merlin, P. Domingo, and Luc Vervisch. Immersed boundaries in large eddy simulation of compressible flows. *Flow Turbulence Combust*, 90:28–68, 2013.

[74] M. Meyer, A. Devesa, S. Hickel, X.Y. Hu, and N.A. Adams. A conservative immersed interface method for large-eddy simulation of incompressible flows. *Journal of Computational Physics*, 229:6300–6317, 2010.

[75] M. Meyer, S. Hickel, and N.A. Adams. Assessment of implicit large-eddy simulation with a conservative immersed interface method for turbulent cylinder flow. *International Journal of Heat and Fluid Flow*, 31:368–377, 2010.

[76] R. Mittal and G. Iaccarino. Immersed boundary methods. *Ann. Rev. Fluid Mech*, 37:239–261, 2005.

[77] J. Mohd-Yusof. Combined immersed boundary/B-spline methods for simulations of flows in complex geometries. *Center for Turbulence Research Annual Research Briefs*, 160(1):317–327, 1997.

[78] J.W. Nam and F.S. Lien. A ghost-cell immersed boundary method for large-eddy simulations of compressible turbulent flows. *International Journal of Computational Fluid Dynamics*, 28:41–55, 2014.

[79] J.W. Nam and F.S. Lien. Assessment of ghost-cell based cut-cell method for large-eddy simulations of compressible flows at high reynolds number. *International Journal of Heat and Fluid Flow*, 53:1–14, 2015.

[80] B. Niceno and S. Kuhn. Direct numerical simulation (DNS) of turbulent flow over wavy surfaces. *V European Conference on Computational Fluid Dynamics, ECCOMAS CFD 2010, Lisbon, Portugal*, 2010.

[81] J. Oliger and A. Sundstroem. Theoretical and practical aspects of some initial boundary value problems in fluid mechanics. *SIAM J. Appl. Math.*, 35:419–446, 1978.

[82] R.M. Orselli, J.R. Meneghini, and F. Saltara. Two and three-dimensional simulation of sound generated by flow around a circular cylinder. *AIAA paper*, pages 2009–3270, 2009.

[83] P. De Palma, M.D. de Tullio, G. Pascazio, and M. Napolitano. An immersed-boundary method for compressible viscous flows. *Computers and Fluids*, 123:450–465, 2006.

[84] C.S. Peskin. Flow patterns around heart valves: a numerical method. *Journal of Computational Physics*, 10:252–271, 1972.

[85] U. Piomelli, T.A. Zang, C.G. Speziale, and M.Y. Hussaini. On the large-eddy simulation of transitional wall-bounded flows. *Physics of Fluids*, 2:257–265, 1990.

[86] T.J. Poinsot and S.K. Lele. Boundary conditions for direct simulations of compressible viscous flows. *Journal of Computational Physics*, 101:104–129, 1992.

[87] S. Popinet. Gerris: a tree-based adaptive solver for the incompressible Euler equations in complex geometries. *Journal of Computational Physics*, 190:572–600, 2003.

[88] J.J. Quirk. An alternative to unstructured grids for computing gas dynamic flows around arbitrarily complex two-dimensional bodies. *Computers and Fluids*, 23:125, 1994.

[89] B. N. Rajani, A. Kandasamy, and Sekhar Majumdar. Numerical simulation of laminar flow past a circular cylinder. *Applied Mathematical Modelling*, 33:1228–1247, 2009.

[90] J.D. Revell, R.A. Prydz, and A.P. Hays. Experimental study of airframe noise vs. drag relationship for circular cylinders. *Lockheed Report 28074, Feb. 1977. Final Report for NASA Contract NAS1-14403.*

[91] S.W. Rienstra and A. Hirschberg. An introduction to acoustics. *Eindhoven University of Technology*, 2004.

[92] P.L. Roe. Approximate Riemann solvers, parameter vectors and different schemes. *Journal of Computational Physics*, 43:357–372, 1981.

[93] P.L. Roe. Characteristic-based schemes for the Euler equations. *Ann. Rev. Fluid Mech.*, 18:337–365, 1986.

[94] F. Roman, V. Armenio, and J. Froehlich. A simple wall-layer model for large eddy simulation with immersed boundary method. *Physics of Fluids*, 21(101701):1–4, 2009.

[95] D.H. Rudy and J.C. Strikwerda. A non-reflecting outflow boundary condition for subsonic Navier-Stokes calculations. *Journal of Computational Physics*, 36:55–70, 1980.

[96] D.H. Rudy and J.C. Strikwerda. Boundary conditions for subsonic compressible Navier-Stokes calculations. *Computers and Fluids*, 9:327–338, 1981.

[97] E.M. Saiki and S. Biringen. Numerical simulation of a cylinder in uniform flow: application of a virtual boundary method. *Journal of Computational Physics*, 123:450–465, 1996.

[98] J.H. Seo and Y.J. Moon. Aerodynamic noise prediction for long-span bodies. *Journal of Sound and Vibration*, 306:564–579, 2007.

[99] C.W. Shu and S. Osher. Efficient implementation of essentially non-oscillatory schock capturing schemes. *Journal of Computational Physics*, 77:439–471, 1988.

[100] C.W. Shu and S. Osher. Efficient implementation of essentially non-oscillatory schock capturing schemes: Ii. *Journal of Computational Physics*, 83:32–78, 1989.

[101] B.A. Singer, K.S. Brentner, and D.P. Lockard. Simulation of acoustic scattering from a trailing edge. *Journal of Sound and Vibration*, 230:541–560, 2000.

[102] J. Smagorinsky. General circulation experiments with the primitive equations. *Monthly Weather Review*, 91:99–165, 1963.

[103] J.L. Steger and R.F. Warming. Flux vector splitting of the inviscid gasdynamic equations with application to finite-difference methods. *Journal of Computational Physics*, 40:263–293, 1991.

[104] J.M. Stockie and B.R. Wetton. Analysis of stiffness in the immersed boundary method and implications for time-stepping schemes. *Journal of Computational Physics*, 154:41–64, 1999.

[105] A. Suksangpanomrung, N. Djilani, and P. Moinat. Large-eddy simulation of separated flow over a bluff rectangular plate. *International Journal of Heat and Fluid Flow*, 21:655–663, 2000.

[106] Z.S. Sun, Y.X. Ren, S.Y. Zhang, and Y.C. Yang. High-resolution finite difference schemes using curvilinear coordinate grids for DNS of compressible turbulent flow over wavy walls. *Computers and Fluids*, 45:84–91, 2011.

[107] L. Temmerman, M.A. Leschziner, C.P. Mellen, and J. Froehlich. Investigation of wall-function approximations and subgrid-scale models in large eddy simulation of separated flow in a channel with streamwise periodic constrictions. *International Journal of Heat and Fluid Flow*, 24:157–180, 2003.

[108] F. Tessicini, G. Iaccarino, M. Wang, and R. Verzicco. Wall modeling for large-eddy simulation using an immersed-boundary method. *CTR Annu. Res. Briefs*, pages 181–187, 2002.

[109] A. Thom. The flow past circular cylinder at low speeds. *Proc. Royal Soc. A*, 141:651–669, 1933.

[110] K.W. Thompson. Time dependent boundary conditions for hyperbolic systems. *Journal of Computational Physics*, 68:1–24, 1987.

[111] K.W. Thompson. Time dependent boundary conditions for hyperbolic systems, ii. *Journal of Computational Physics*, 89:439–461, 1989.

[112] Y.H. Tseng and J.H. Ferziger. A ghost-cell immersed boundary method for flow in complex geometry. *Journal of Computational Physics*, 192:593–623, 2003.

[113] H.S. Udaykumar, R. Mittal, and P. Rampunggoon. Interface tracking finite volume method for complex solid-fluid interactions on fixed meshes. *Commun. Numer. Methods Eng.*, 18:89–97, 2002.

[114] H.S. Udaykumar, R. Mittal, P. Rampunggoon, and A. Khanna. A sharp interface cartesian grid method for simulating flows with complex moving boundaries. *Journal of Computational Physics*, 174:345–380, 2001.

[115] H.S. Udaykumar, R. Mittal, and W. Shyy. Solid-liquid phase front computations in the sharp interface limit on fixed grids. *Journal of Computational Physics*, 153:535–574, 1999.

[116] H.S. Udaykumar, W. Shyy, and M.M. Rao. A mixed Eulerian-Lagrangian method for fluid flows with complex and moving voundaries. *Int. J. Numer: Methods Fluids*, 22:691–705, 1996.

[117] B. van Leer. Towards the ultimate conservative difference scheme. v. a second order sequel to godunov's method. *Journal oc Computational physics*, 32:101–136, 1979.

[118] R. Verzicco, J. Mohd-Yusof, P. Orlandi, and D. Haworth. Large eddy simulation in complex geometry configurations using boundary body forces. *AIAA Journal*, 38:427–433, 2000.

[119] B. Vreman, B. Geurts, and H. Kuerten. Subgrid-modelling in LES of compressible flow. *Applied Scientific Research*, 54:191–203, 1995.

[120] G. Waller. Prediction of flap-edge noise using STAR-CD. *AIAA paper*, pages 2008–2863, 2002.

[121] D.C. Wilcox. *Turbulence Models for CFD 3rd Ed.* DCW Industries Inc., 2006.

[122] C.H.K. Williamson. Vortex dynamics in the cylinder wake. *Ann. Rev. Fluid Mech.*, 8:477–539, 1996.

[123] T. Ye, R. Mittal, HS. Udaykumar, and W. Shyy. An accurate cartesian grid method for viscous incompressible flow with complex immersed boundaries. *Journal of Computational Physics*, 156:209–240, 1999.

[124] T. Ye, R. Mittal, H.S. Udaykumar, and W. Shyy. A cartesian grid method for viscous incompressible flows with complex immersed boundaries. *AIAA paper*, pages 99–3312, 1999.

[125] A. Yoshizawa. Statistical theory for compressible turbulent shear flows, with the application to subgrid modeling. *Physics of Fluids*, 29:2157–2164, 1986.

[126] Y. Zang, R.L. Street, and J.R. Koseff. A dynamic mixed subgridscale model and its application to turbulent recirculating flows. *Physics of Fluids*, 5:3186–3196, 1993.

[127] E.A. Zedler and R.L. Street. Large-eddy simulation of sediment transport: currents over ripples. *Journal of Hydraulic Engineering*, 127:444–452, 2001.